Improved estimates of air-sea oxygen fluxes and biological carbon export through the use of self-calibrating Argo oxygen floats in the Pacific

Seth Michael Bushinsky

A dissertation
submitted in partial fulfillment of the
requirements for the degree of

Doctor of Philosophy

University of Washington
2015

Reading Committee:
Steven R. Emerson, Chair
Paul D. Quay
Stephen C. Riser

Program Authorized to Offer Degree:
School of Oceanography

University of Washington

Abstract

Improved estimates of air-sea oxygen fluxes and biological carbon export through the use of self-calibrating Argo oxygen floats in the Pacific

Seth Michael Bushinsky

Chair of the Supervisory Committee:
Professor Steven R. Emerson
School of Oceanography

The production and consumption of oxygen during photosynthesis and respiration stoichiometrically links oxygen and organic carbon in the surface ocean. Oxygen sensors are currently being deployed on profiling floats throughout the ocean, which has the potential to greatly expand the extent of in situ oxygen measurements and our understanding of biological processes in the ocean. Inaccuracies in current oxygen sensors due to instrument drift currently limit the utility of these floats for estimating air-sea oxygen fluxes. This thesis describes in situ calibrations of oxygen sensors on profiling floats through atmospheric measurements and the use of this data towards understanding oxygen and organic carbon cycles in the Pacific. We deployed 12 modified Argo floats equipped with Aanderaa oxygen optodes in the Pacific: one at Ocean Station Papa (OSP) in the northeast Pacific, 10 in the Kuroshio Extension (KE), and one in the south subtropical Pacific near Samoa. Air oxygen measurements after each float profile were used to accurately calibrate the optodes and correct for drift observed in approximately ½ of the optodes over >2 years. I interpret these oxygen data using two methods. At OSP, I developed a 1-dimensional abiotic gas model for use with oxygen data to determine the annual net community production (ANCP). I found that summertime production was roughly balanced by wintertime net heterotrophy and that estimates of bubble-induced, air-sea exchange and diapycnal diffusion at the base of the mixed layer were important to interpretation of oxygen fluxes. In the KE I interpreted data from multiple floats to determine mean annual cycles of supersaturation and air-sea oxygen fluxes from biogeochemical regions. While the magnitude of the abiotic oxygen fluxes in winter is too high to quantify ANCP in this area, I calculated summertime production and winter subduction from the regional oxygen data. This work represents an improvement in our ability to remotely measure in situ oxygen and new methods of interpretation so that a global array of oxygen sensors on profiling floats can be used to quantify the marine oxygen and carbon cycles.

TABLE OF CONTENTS

LIST OF FIGURES

LIST OF TABLES

ACKNOWLEDGEMENTS

The National Science Foundation generously supported this work in multiple ways: through grant OCE-1129112, which funded float development and deployment, and through a Graduate Research Fellowship and an Integrative Graduate Education and Research Traineeship, both of which funded the majority of my graduate career.

In addition to being a member of my committee, Stephen Riser and his research group were essential to the development and deployment of the floats discussed throughout this dissertation. In particular, Dana Swift and Rick Rupan helped me understand what we could and could not do with these floats and were the reason we were able to collect so much good data.

Paul Quay and Eric Riser, two other members of my committee, provided valuable feedback and critical consideration of the challenges inherent to this work and how best to approach the problems we faced. I came to the University of Washington hoping to work with both Paul and Eric and am glad I had the chance to do so.

Much of this work, from the initial test float deployment at Ocean Station Papa, to the numerous Line P cruises and mooring turnarounds that we used to support float data, relied on collaboration and cooperation with a number of scientists from the National Oceanic and Atmospheric Administration Pacific Marine Environmental Laboratory. Specifically, Meghan Cronin and her research group were integral to every piece of work we did at Ocean Station Papa. On land, Stacy Maenner in particular was helpful and patient as we integrated our oxygen measurements with their data stream and Keith Ronnholm effectively coordinated much of the work between our group and NOAA. I would like to thank Michael Craig and Jennifer Keene for being great company through many gray days in the Pacific.

Marie Robert both led the Line P program at the Institute of Ocean Sciences of Fisheries and Oceans Canada and was a good friend and accommodating Chief Scientist on all of my Line P cruises. I would also like to thank the many other Institute of Ocean Sciences researchers who helped me in data collection and instrument deployment at Ocean Station Papa. Roberta Hamme and her lab group provided several of the calibration samples from Line P cruises that were so helpful in comparing mooring and float datasets.

I had the pleasure of working at sea on several ships throughout my graduate career. My first and last cruises were on the University of Washington's R/V Thomas G. Thompson, which was a wonderful resource to have close at hand. Both the White and Red crews of the CCGS John P. Tully were among the most professional, helpful, and fun people I have worked with at sea. The crew of the R/V Melville and the UW undergraduate students on our 2013 Kuroshio Extension cruise were key to successful deployment of 17 floats despite challenging conditions and an ambitious experimental design.

I would like to thank the graduate students I was fortunate enough to know and work with at the University of Washington, both in the School of Oceanography and through the Program on Climate Change. It is hard to imagine a better group of peers with whom to navigate the trials and oddities of graduate school. My officemates Andrea Fassbender and Kevin Tempest, who kept me focused and happy, were especially appreciated. Many other students were good friends, colleagues, and outdoor partners and deserve thanks for making this an enjoyable experience, both scientifically and personally. Andrea Fassbender, Hilary Palevsky, and Noel Pelland were welcome compatriots as we sought to understand the workings of carbon and oxygen in the Pacific. I would like to thank Noel Pelland in particular for many afternoons spent discussing the finer points of diffusivity and air-sea exchange over coffee.

The other members of the Emerson lab group have been good colleagues throughout this process. Chuck Stump taught me many things in the realm of oxygen and instrumentation; this work would have been much harder without him. Mariela R.T. White has been both a helpful partner in the lab and a source of support ever since the Kuroshio cruise. Many of the lab optode calibrations in this work were done by her and Diane Perry.

Steven Emerson has been the advisor I hoped for throughout graduate school. His guidance and dedication to understanding the important questions in our work has kept me focused and made this project enriching and rewarding. I will miss the afternoons spent at his whiteboard, attempting to unravel a new layer of the puzzle.

DEDICATION

This thesis is dedicated to my family. My parents, David and Nancy, who supported and encouraged me, even, and especially, when I most resisted their efforts. To my brother, Josh, who has always been there for me and to whom I always look up to and try to impress while pretending that I am not. To my sister-in-law Elyse, who can relate all too well to these struggles, and to my nephew Saul, who has been a bright spot on many a late night. And finally to my girlfriend and partner, Allison, may we continue to enjoy the journey wherever it takes us.

Chapter 1

Introduction

During photosynthesis in the ocean, organic carbon is fixed and oxygen is produced in a stoichiometric ratio of $\Delta O_2/\Delta C = 1.45$ (Hedges et al. 2002). Organic carbon that is produced and leaves the upper ocean without being respired represents a net transfer of carbon from the atmosphere to the deep ocean. This biological export of carbon, also known as annual net community production (ANCP), is an important control on the carbon dioxide concentration in the atmosphere (Volk and Hoffert 1985).

In situ estimates of this carbon flux typically require measurements made at ocean time series sites where high frequency, accurate measurements are possible. Measurements must also be made over an entire annual cycle, as photosynthesis and respiration do not occur equally throughout the year. Global estimates of ANCP can be made using ocean color and backscatter measurements along with parameterizations relating primary production to carbon export (Westberry et al. 2012; Siegel et al. 2014). Satellite based calculations of carbon export have a limited number of ground truth sites for comparison, which makes it difficult to assess their accuracy.

The oxygen mass balance method of determining ANCP utilizes the stoichiometric relationship between oxygen production and organic carbon fixation to determine biological carbon export. By measuring oxygen fluxes out of the euphotic zone, one can infer the export of organic carbon over the course of a year. Most oxygen mass balance estimates of ANCP have found 3 ± 1 mol C m^{-2} yr^{-1} of export from the surface ocean regardless of location (Emerson 2014). In contrast, satellite-based estimates show a large increase in carbon export from the subtropics to the subarctic gyres and equator.

To reconcile remote sensing and in situ estimates of ANCP, we seek to expand the number and geographic range of in situ oxygen mass balance estimates by making oxygen measurements on profiling floats. This requires sufficient accuracy to resolve the air-sea difference in oxygen concentration and an alternative to simultaneous measurement of inert gas tracers typically used to separate the physical and biological processes creating supersaturation.

The air-sea flux of oxygen is the most important term in the mixed layer oxygen mass balance. The flux is driven by the supersaturation of the surface water, or the difference between the calculated concentration of gas at saturation and the measured concentration of gas in the water. Since this varies by only several percent annually, we must be able to measure oxygen accurately to a few tenths of a percent.

One of the major limitations for determining oxygen-based mass balance estimates of ANCP using in situ measurements on unmanned platforms is the accuracy of oxygen sensors. Aanderaa optodes are currently used on moorings and profiling floats, but have known drift problems prior to deployment (D'Asaro and McNeil 2013; Bittig and Körtzinger 2015). While careful calibration on deployment can deal with drift since the last laboratory calibration, any subsequent drift will create error in air-sea gas flux calculations. Recent studies have not found measurable drift in optodes on Argo floats post-deployment to levels of 1-3 % per year (Takeshita et al. 2013), but this is not accurate enough to determine drift that could significantly impact air-sea gas flux calculations.

In chapter 2, I describe our efforts to develop an in situ air calibration method for Aanderaa Optodes on profiling floats. We deployed 12 Argo floats equipped with 1 or 2 optodes in three locations in the Pacific Ocean: one in the northeast subarctic Pacific near Ocean Station Papa, 10 across the Kuroshio Extension in the northwestern Pacific, and one in the south subtropical Pacific. Each of these floats has been sampling for over 1 year and 9 have been deployed for over 2 years, allowing calculation of long-term in situ drift of the optodes.

In situ air measurements provided initial optode calibration to an accuracy of ± 0.1% and determination of subsequent drift to ± 0.1% yr^{-1}. Independent Winkler titrations made on deployment of the floats were the same as the air calibrations to ± -0.5%. For the float at OSP, its proximity to the OSP surface mooring allowed a comparison over 2.5 years, which revealed an accuracy of within ± 0.2%. Measurable drift after deployment was found in 3 optodes at a 95% confidence interval and 9 optodes at a 68% confidence interval out of the 14 optodes deployed for greater than 1 year. Optode drift was negative in 7 of the 9, with the largest magnitude -0.5% yr^{-1} and positive in 2 out of the 9, with a maximum of +0.5% yr^{-1}. In light of the variable drift rates observed here, I conclude that on-going in situ calibrations are necessary to accurately interpret Argo oxygen data in terms of air-sea fluxes. Additional recommendations for atmospheric air calibration of Argo optodes can be found in section 2.5.

In chapters 3 and 4, I detail two separate methods for interpreting in situ calibrated oxygen measurements from the floats we deployed in the Pacific. Chapter 3 describes calculation of ANCP from one year of float data at Ocean Station Papa. Because oxygen changes in the upper ocean result from both biological and physical processes, it is necessary to determine the physical fluxes in order to calculate the remaining net oxygen flux. Mooring or time series based oxygen mass balances typically use inert gases, such as nitrogen or argon, to estimate the physical contribution to oxygen fluxes (e.g., Emerson and Stump 2010). Instead, we calculate the abiotic oxygen flux using a 1-dimensional gas evolution model that incorporates float-determined temperature and salinity and is initialized with measured oxygen data. Abiotic oxygen fluxes are calculated through one year, and annual net community production is estimated as the difference between the measured, biological oxygen flux, and the calculated abiotic flux. For June 2012-June 2013, we calculate a summertime net community production of 1.4 ± 0.4 mol C m^{-2} and an ANCP of 0.7 ± 0.5 mol C m^{-2} yr^{-1}. While the summertime value is within the range of past measurements, the annual value is significantly lower than previous estimates. This is in large part due to inferred wintertime heterotrophy, which is necessary to balance the flux of oxygen from the atmosphere due to air injection by bubbles caused by high wind speeds and slightly undersaturated waters. The model also reveals that diapycnal diffusivity at the base of the winter mixed layer created a flux large enough to influence the annual oxygen mass balance in the upper 110 meters of ocean.

In chapter 4, I describe a method for interpreting float data in three areas of the Pacific Ocean: the Alaska Gyre, the southern subtropical Pacific gyre, and the Kuroshio Extension. The Kuroshio Extension is a region of strong carbon dioxide uptake by the ocean with large advective flow. Rather than act as true Lagrangian drifters, Argo floats spend the majority of their time at 1000m, before diving to 2000m and profiling to the surface. In a highly advective region such as the Kuroshio Extension, floats can surface in multiple water masses throughout their lifetime. In order to interpret float data in this region, I divided float profiles in the Kuroshio Extension into north, central, and south regions with distinct annual cycles of oxygen supersaturation using a combination of temperature-salinity relationships and geographic location.

The mean annual air-sea flux from the Alaska Gyre was -0.3 mol m^{-2} yr^{-1} (positive represents fluxes to the ocean), fluxes calculated for the northern, central, and southern Kuroshio Extension regions were 6.8, 10.5, and 0.5 mol m^{-2} yr^{-1}, respectively, and for the south subtropical Pacific near Samoa 0.6 mol O_2 m^{-2} yr^{-1}. Large wintertime fluxes into the ocean were primarily driven by bubble injection, which contributed greater than 50% of the total flux in the winter and significantly to net annual fluxes. Seasonal changes in solubility coupled with deep mixed layers allowed the North and Central KE regions to take up large amounts of oxygen, some of which was exported during mode water formation. The magnitude of the physical fluxes makes it unlikely that we will be able to use these data to calculate ANCP. However, summertime biological flux calculations are possible due to shallow mixed layers and the reduced impact from mixing. Summertime biological production in the mixed layers of the North, Central, and South KE regions averaged 2.6, 0.2, and 1.3 mol O_2 m^{-2}, respectively. Combined with our estimates of air-sea flux and subduction, these production estimates help us to start closing the mass balance for oxygen in the KE region.

This thesis demonstrates that in situ calibration of Aanderaa oxygen sensors can result in oxygen measurements with high enough accuracy for air-sea flux calculations. This makes it possible to use oxygen sensors on profiling floats to determine oxygen mass balance estimates of the biological carbon flux, something that was previously restricted to moorings and repeat hydrographic studies. Some areas of the ocean, such as the Kuroshio Extension, present difficulties with a 1-dimensional interpretation, but by partitioning data from multiple floats into biogeochemical regions we can still use oxygen fluxes to help constrain physical and biological processes in the ocean. This research shows the way to determine accurate air-sea oxygen fluxes on profiling floats. Calculations of ANCP using this data should eventually help constrain global biological carbon export from satellite data.

Chapter 2

Accurate oxygen measurements on modified Argo floats using in situ air calibrations

Abstract

Oxygen is an important tracer for biological processes in the ocean. Measuring changes in oxygen over annual cycles gives information about photosynthesis and respiration and their impact on the carbon cycle. Long-term, accurate oxygen measurements over wide areas are needed to determine changes in ocean oxygen content and oxygen deficient zones. Oxygen sensors have been increasingly mounted on Argo floats that profile between 2000 m and the ocean surface. These measurements are currently too inaccurate to calculate the air-sea gas flux, which is the dominant flux of oxygen in the surface ocean and typically driven by surface oxygen supersaturations of only ± several percent.

In this study we present data from 17 Aanderaa oxygen optodes mounted on 11 Argo floats specially modified to make atmospheric measurements for calibration. Optodes measure oxygen equally well in air and water, allowing the use of atmospheric oxygen to perform on-going in situ calibrations throughout the lifetime of the float. We find that it is necessary to make atmospheric measurements at night, that raising optodes higher into the air reduces variance in the air measurements, and that multiple measurements each time a float surfaces provides better data for in situ calibration. Initial optode calibration on deployment has an average uncertainty of ± 0.1% (1 σ) and optode drift can be calculated to ± 0.1% yr^{-1}. Measurable drift was determined in 3-9 optodes out of the 14 that were deployed for ~2 years. The maximum drift rate measured was -0.5% yr^{-1}, which is large enough to strongly impact calculations of air-sea oxygen fluxes.

2.1 Introduction

Oxygen is produced by photosynthesis in a stoichiometric ratio to the amount of organic carbon fixed and consumed when biological matter is respired. Any organic carbon that is produced in the upper ocean and respired at depth will be matched by an equivalent flux of oxygen out of the upper ocean. The movement of organic carbon from the surface ocean to the deep ocean is known as the biological carbon pump, a key component of the carbon cycle (Volk and Hoffert 1985).

Biological carbon export from the surface ocean is an important part of the carbon cycle but is difficult to measure due to the relatively small fraction of organic matter that leaves the surface ocean and the variability of export across space and time. Estimates of biological carbon export based on remote sensing data have sought to fill in gaps in our understanding of the magnitude and variability of this flux to the deep ocean (Westberry et al. 2008; Laws et al. 2011; Siegel et al. 2014). These estimates rely on in-situ validation measurements that are often limited to discrete times or fixed locations. Seasonal and interannual variability of carbon production, consumption, and export requires annual measurements, which further complicates in-situ validation (Emerson 2014).

Oxygen mass balance estimates of carbon export leverage the stoichiometric relationship between oxygen and organic carbon to use oxygen as a tracer for carbon export (Emerson et al. 1997, 2008). Emerson et al. (2008) concluded that a ± 0.5% error in mooring [O_2] measurements produces a ± 50% error in net biological production calculated using a mass balance method. The method's sensitivity to oxygen accuracy is due to the fact that oxygen supersaturation (the relative difference between the amount of oxygen the water can hold at equilibrium with the atmosphere and the actual oxygen content) varies by only several percent over the course of a year in most areas of the ocean. Much of the excess oxygen produced during photosynthesis drives a flux into the atmosphere that is a function of the degree of oxygen supersaturation (Liss and Merlivat 1986; Wanninkhof 1992). Therefore, in order to accurately estimate the biological carbon flux, high accuracy oxygen measurements or precise measurements of the difference in oxygen pressure between the surface ocean and atmosphere are needed.

Widespread, accurate oxygen measurements are also needed to determine the extent of oxygen minimum zones (OMZs), interior regions of the ocean depleted in oxygen due to degradation of large amounts of organic matter and limited ventilation (Kamykowski and

Zentara 1990; Helly and Levin 2004). Expansion of oxygen minimum zones has been documented over the past several decades and shown to cause changes in ecosystem composition (Diaz and Rosenberg 2008). OMZs are influenced by seasonal currents in addition to long term trends (Stramma et al. 2008), making it important have annual measurements over large areas, which is difficult using intermittent repeat hydrography cruises. The accuracy of oxygen titrations also decreases with lower oxygen concentrations, limiting researcher's ability to effectively determine temporal trends.

To date, most long-term studies of oxygen changes and fluxes have taken the form of either repeat hydrography comparisons (such as the World Ocean Circulation Experiment, e.g. Helm et al. (2011)) or time series stations (for example the Hawai'i Ocean Time-series in the North Pacific subtropical gyre (Bingham and Lukas 1996), Ocean Station Papa (OSP) in the Alaska Gyre (Whitney et al. 2007), and the Bermuda Atlantic Time Series in the subtropical Atlantic (Stanley et al. 2006)). These are invaluable to our understanding of oxygen dynamics and long-term changes, but are either limited in time resolution (repeat hydrography) or space (time series locations).

The Argo program has exponentially increased available temperature and salinity measurements through the use of profiling floats distributed throughout the ocean (Roemmich et al. 2009). While several hundred Argo floats have been deployed with oxygen sensors of various types (Gruber et al. 2009), these sensors have been insufficiently accurate to be used for determination of air-sea gas exchange. Takeshita et al. (2013) made an effort to post-calibrate all currently functioning oxygen sensors using a combination of WOCE climatology at depth and assumed saturation in the near surface. This does improve accuracy, but only to within ± 3% of surface oxygen, which is still not accurate enough to resolve long-term oxygen trends or make accurate estimates of air-sea oxygen flux.

Aanderaa oxygen optodes, which are typically thought to be stable in the field, have been troubled by sensor drift prior to deployment, rates of which have been documented at ~ 4-5% yr^{-1} (D'Asaro and McNeil 2013). Once deployed on Argo floats, optodes spend the vast majority of their time at 1000 m depth and 2-5°C, which likely accounts for their increased stability. However, given the logistical challenges in recovering deployed floats, few floats are re-visited after a significant amount of time and it is unlikely that drift of <1% yr^{-1} would be readily observed. Given that all studies of optode stability have shown significant drift prior to deployment, it seems logical that some drift would still occur post-deployment. To accurately estimate air-sea oxygen flux, drift of even a few tenths of a percent per year can become important.

In order to improve the accuracy of oxygen optodes on Argo floats and make them useful for studies involving air-sea fluxes or low-oxygen measurements, in situ calibrations are needed. Körtzinger et al. (2005) proposed using in situ atmospheric measurements to calibrate Argo oxygen floats. This method has been tested in a few smaller scale studies. Bushinsky and Emerson (2013) used measurements from air pumped down to a submerged housing to calibrate an optode in a calibration system designed for moorings. Emerson and Bushinsky (2014) compared one year of an air-calibrated Argo oxygen float to data from an independently calibrated surface mooring at Ocean Station Papa and found good agreement between calibrations (updated data from this float is presented in this study). Fiedler et al. (2013) conducted several one and two month deployments off the Cape Verde Islands testing in-situ air calibrations with an accuracy of ± 2 μmol kg^{-1}, while Bittig and Körtzinger (2015) performed a 1.5 year experiment off the West African coast and were able to use air measurements for calibration by implementing a correction method for wave splashing of the optode. Both the Fiedler et al. and Bittig and Körtzinger studies used floats equipped with external air bladders that could raise the oxygen optodes higher out of the water in an attempt to achieve a cleaner air sample. Johnson et al. (2015) utilized single air measurements from profiling floats to determine an average gain correction for optode measurements and found no evidence for long-term drift greater than ± 1% error after deployment.

These studies have begun to demonstrate the utility of air measurements for in situ oxygen calibration and in the case of Johnson et al. (2015), seek to quantify post-deployment drift. However, it is unclear if single atmospheric measurements are sufficient to precisely measure atmospheric oxygen. Splashing by surface waves, storms with rapidly changing pressure that would impact expected atmospheric pO_2 and high winds that could induce evaporative cooling on the optode surface, and other atmospheric phenomenon could impact individual optode measurements, making it important to further explore how best to use atmospheric oxygen for in situ calibrations.

In this study, we describe our efforts to develop a method for in situ calibration of oxygen optodes on profiling floats. Optodes were calibrated in the laboratory against Winkler measurements to characterize optode behavior and sensitivity. Next, optodes deployed on modified Argo floats (hereafter referred to as Special-Oxygen-Sensor Argo floats, or SOS-Argo) at Ocean Station Papa and in the Kuroshio Extension were calibrated multiple times upon deployment by ship-based Winkler calibration casts. Finally, the Argo floats described in this study sampled the atmosphere repeatedly at each surfacing to calibrate the sensor using atmospheric pO_2, allowing determination of deployment calibration and long-term drift.

2.2 Methods

2.2.1 Lab calibrations

Water calibration: Optodes were calibrated in the lab prior to deployment according to the general procedure described in (Bushinsky and Emerson 2013). Calibrations were performed from 1-21°C (a minimum of 5 temperatures across this range) and from 0-125% oxygen saturation. Optodes were submerged in a well mixed, temperature controlled water bath. Saturations above zero were reached by bubbling nitrogen or oxygen gas to strip oxygen out or add oxygen to the water. Diffusion across the top surface of the water bath was limited by floating pieces of foam. Calibration experiments used artificial seawater with salinity between 32 and 35 prepared according to Kester et al. (1967). Replicate Winkler measurements were made at each oxygen and temperature combination (approximately 30-45 points per optode).

Zero oxygen measurements were carried out across all temperatures by saturating a beaker with sodium sulfite (Na_2SO_3, ~5g/500ml seawater) to strip out oxygen. The beaker was placed inside a temperature controlled cooler and $[O_2]$ in the beaker was initially lowered by bubbling with N_2 gas.

Winkler titrations yield oxygen concentration ($[O_2]$), while Aanderaa optodes theoretically respond to the partial pressure of oxygen (pO_2) in water (Demas et al. 1999; Stokes and Somero 1999; Tengberg et al. 2003). The concentration of oxygen, $[O_2]$, is related to its pO_2, through the Henry's Law coefficient, $K_{H,C}$:

$$[O_2] = K_{H,O2} \times pO_2 \tag{2.1}$$

Winkler measurements were matched with optode readings taken in between the start and end of Winkler sampling. Winkler replicates were used for the calibrations only if the percent standard deviation of the replicate was less than 0.2% in saturated water. The precision of Winkler titrations is a function of the smallest increment of sodium thiosulfate titrant added to the solution. The 0.2% s.d. threshold was scaled for lower oxygen samples relative to the oxygen concentration in order to retain low oxygen measurements. Optode data were removed if the measurements changed by more than 0.05% during the Winkler sampling period.

If both optode and Winkler samples met the above criteria, raw optode response (phase, units of degrees) was plotted against temperature and Winkler-measured oxygen to calculate calibration coefficients (Figure 2.1). Calibration surfaces were fit to Winkler derived pO_2 using the Stern-Volmer-derived equation from Uchida et al. (2008). Any data point with a residual (difference between the Winkler pO_2 and the calculated surface) greater than 2 standard deviations from the mean of the absolute value of the residuals was removed and the calibration coefficients were recalculated. See Table 2.1 for total calibration points used for each optode. Calibrations were performed over the course of 1-2 weeks to avoid optode drift during the duration of the run.

Air response: Optode air response for all KE optodes was measured in the lab in a similar method to Bushinsky and Emerson (2013). Humidified air was pumped into a fully opaque, submerged chamber containing up to four optodes and held at several temperatures between 2-21°C, while the pressure was measured using a Paroscientific Model 223A-101 pressure transducer (accuracy ±0.01% (Wearn and Larson 1982)). Atmospheric pO_2 was calculated according to:

$$pO_2^{atmos} = \left(P_{Atm} - pH_2O\left(\frac{RH}{100}\right)\right) X_{O2} \tag{2.2}$$

where pO_2^{atmos} is the partial pressure of oxygen expected in the atmosphere, P_{atm} is the total air pressure measured by the Paroscientific pressure sensor, pH_2O is the water vapor pressure (Zeebe and Wolf-Gladrow 2001), RH is the relative humidity in percent (assumed to be 100%

for lab measurements), and X_{O2} is the mole fraction of oxygen in the atmosphere (X_{O2} = 0.20946 (Glueckauf 1951)). Air response was measured within two weeks of water calibrations.

2.2.2 Float modifications

SOS-Argo floats are modified Apex profiling floats constructed at the University of Washington and designed to accommodate an air calibration period while staying within the operational requirements for the Argo program. All floats had an optode on a 61cm stalk above the end cap (Figure 2.2) and 6 of the floats had a second optode at either ~10cm (close to standard Argo optode height (Körtzinger et al. 2005)) or 20 cm height. The variable heights were used to determine the necessary elevation above the sea surface to reduce the influence of waves on the sensor during air measurements. Stalks were milled from polyether ether ketone (PEEK) tubes, with an outside diameter of 20.3 mm and a through hole of 4 mm. Stalks were threaded into the float end caps with an O-ring seal. To maintain stability despite the increased mass higher on the float's vertical axis, float hulls were made from carbon fiber instead of aluminum in order to lower the center of gravity.

Float firmware was modified to allow air measurements after surfacing. Upon surfacing, each float entered a telemetry phase, during which the GPS location and data files were transmitted. After finishing telemetry, but prior to initiating a dive, the optode(s) were sampled in the atmosphere according to an adjustable interval and duration. Data from the surface period was stored in a separately transmitted file.

2.2.3 Field Data

Float Deployments: The initial deployment at Ocean Station Papa (float S/N 8397) was designed to test physical and firmware modifications. The float was deployed at 50.0 N, 144.8 W from the CCGS John P. Tully on June 2, 2012 and has been operating since on a 5-10 day cycle (Figure 2.3). Float 8397 has completed 227 profiles as of August 2015. Four comparison hydrocasts with Winkler oxygen measurements were performed near the float. Argo floats sample as they rise to the surface, making timing of comparison casts and matching Winkler and optode measurements difficult. For the initial deployment period, the float was programed to profile as quickly as possible, with approximately 18-19 hours between profiles. The first three calibration casts were between 1.7-5 km away from the termination location of a float profile and were sampled between approximately 0.5 hours ahead of a profile termination and 2.5 hours after. For the fourth calibration cast, the ship waited for the float to surface and transmit its location before moving in to sample, 0.7 km away and 0.75 hours after profile termination. The fourth cast was only to 20 m away to further reduce the time difference between Winkler samples and optode measurements.

In February and March 2013 ten floats were deployed from the R/V Melville at roughly equal spacing (alternating single and dual optode configurations) between 30 N, 146 E, and 40 N, 150 in the Kuroshio Extension region (Figure 2.3). Deployments were performed as part of a University of Washington student cruise. KE floats have completed between 182 and 194 profiles as of August 2015.

Comparison casts were performed immediately prior to deployment on the northern cruise track, and tracked for a second comparison cast along the return, southern cruise track. Surfacing locations were predicted based on drift track and floats were instructed to surface only once the R/V Melville was in the area of the float. Float surfacing could only be scheduled at least one profile in advance, so ship position and float surfacing were predicted 1-3 days in advance. Prior to expected surfacing, the Melville was positioned ~9 km away from predicted surfacing location. Each float was allowed to surface, a position was received, and the Melville approached the location but stood off to allow the float to complete its telemetry cycle and a surface air sampling period. After the float began its dive the ship moved to its location and performed a CTD comparison cast. This procedure shortened the time between float data collection and calibration casts to ~2-4 hours. For all hydrocasts, replicate Winkler samples were taken at 24 depths down to 2000m, with more samples near the surface.

In-situ air calibration: Air measurements were made after every float surfacing. Initial float profiles for both OSP and KE were on a minimum cycle in order to maximize communication opportunities. Subsequent profiles for OSP were moved to a 5-10 day cycle and altered to surface only during nighttime. KE floats were instructed to only surface at night throughout their deployment. At times float surfacing time has drifted into the daytime and had to be reset, resulting in periods without nighttime measurements.

On surfacing, each optode measured atmospheric oxygen ($p\mathrm{O}_2^{\mathrm{optode}}$) every 2 minutes for 1 hour. For calibration of float measurements, true atmospheric oxygen ($p\mathrm{O}_2^{\mathrm{atmos}}$) was calculated from equation (2.2) using optode temperature and National Centers for Environmental Prediction (NCEP) reanalysis pressure and relative humidity data interpolated to the location and time of float surface air periods. The NCEP relative humidity product is an estimate for the RH at 10m above sea surface, which was then extrapolated to optode height in the same manner as Bittig and Körtzinger (2015).

2.3 Results

2.3.1 Lab results

Water calibrations: Root mean square errors (RMSE) of calibration surface fits to lab Winkler data averaged 0.27% of atmospheric pO_2 for the KE optodes and 0.60% for the OSP optodes (Table 2.1). OSP optodes were calibrated first, over 6 weeks, which allowed sensor drift to impact the calibration surface fit. An average of 6 out of 42 points were removed for the KE floats according to the Winkler and optode criteria outlined in section 2.2.1. Optodes are theoretically a good instrument with which to measure low oxygen water. The response of the platinum porphyrine foil is more sensitive at low partial pressures of oxygen than at high values. One way to check how well our calibration surfaces are explaining optode response at low oxygen is to observe the impact of adding or removing zero oxygen measurements (made in water with oxygen stripped by sodium sulfite) from the surfaces. The difference between optode output in near anoxic water using calibration coefficients that include and do not include zero oxygen data is ± 1 umol/kg. This gives good confidence that our low oxygen Winklers are adequately constraining the calibration surface at low oxygen values. For calculation of oxygen concentrations above 20% saturation, addition of zero oxygen points to the calibration surface had a smaller impact than the error in the calibration surface.

Air response: In order to assess the ability of optodes to measure pO_2 in air, optode air measurements were made multiple times from 1-21°C and compared to that expected based on the air pressure and temperature (equation 2.2). The mean offset of optode response (for the 15 KE optodes) between and measured expected pO_2^{atmos} was -0.2 ± 0.4% (Figure 2.4). Thus, there was no statistically significant difference between optode response in air and water. This experiment relies on an accurate lab calibration performed close enough in time to the air measurements to avoid any issues with drift. This contrasts with our previous work, in which we showed an offset in air measurements that varied with temperature (Bushinsky and Emerson 2013, Figure 2.8). A likely cause of the previously seen offset was drift over the ~8 months between optode calibration and air response experiments. A second potential cause of the offset or observed temperature dependency is that the optode tested in the previous study (an Aanderaa 4330F) was a fast response optode that lacked the optical isolation layer covering the sensing foil. It is possible that the presence or absence of the optical isolation layer changes the refraction at the edge of the foil, allowing a different amount of fluoresced light to escape and be measured by the photoreceptor in air compared to water.

2.3.2 Field results

In situ calibration against air: Averaged OSP float pO_2 measurements from each air period are plotted in Figure 2.5 with pO_2^{atmos} calculated from equation (2.2) using optode temperature and NCEP relative humidity and pressure. Both the upper (blue) and lower (red) optode measurements calculated using lab calibrations are lower than predicted pO_2^{atmos} (black) due to sensor drift prior to deployment. Lower optode atmospheric measurements at OSP have a larger variance during each sample period (an average of ± 0.35% s.d.) than upper measurements (± 0.23%, Table 2.2). Lower OSP optode measurements are also higher than upper, though this could be due to a lower rate of drift prior to deployment. The average standard deviation for air period averages for all dual optode floats was ± 0.69% for lower optodes and ± 0.32% for upper optodes. This difference likely due to increased splashing by waves, allowing surface oxygen supersaturation to influence lower optode air measurements.

To compare expected pO_2^{atmos} with measured pO_2^{optode} we calculate the percent offset between optode measurements and air pO_2 ($\mathrm{d}pO_2 = \left[(pO_2^{\mathrm{optode}} - pO_2^{\mathrm{atmos}})/pO_2^{\mathrm{atmos}}\right] \times 100$) with pO_2^{atmos} calculated as in equation (2.2). When plotted against the local time of day, mean $\mathrm{d}pO_2$ and the variance at OSP increase to a maximum at local noon (Figure 2.6) and a minimum variance during nighttime hours. This diurnal change correlates best with time of day, rather than measured temperature, estimated relative humidity, or other parameters. We therefore suspect this is due to light interference with the optical sensor and scheduled all floats to surface at night. Any periods during which float profiles ended during daytime were removed from analysis of air measurements and only nighttime (22:00 – 05:00 local) measurements were used for atmospheric calibrations.

To assess the need for multiple air measurements after each surfacing, nighttime air period means were calculated from increasing numbers of air measurements taken every 2 minutes during the 1 hour air period. The mean of each air period was subtracted from the means made with fewer air measurements and the standard deviation of these mean offsets for a representative optode (SN 854 on float 8381) is plotted in Figure 2.7. For all optodes, the standard deviation of the mean difference between the first measurement in an air period and that air period's average is ± 0.61%. Increasing the number of air measurements to 10 reduced the difference from the air period mean to ± 0.17% and after 20 measurements the difference in means was ± 0.08%.

Variance in air period averages was highest during periods of changing atmospheric conditions. We thus filtered atmospheric data by removing air measurements in which: the standard deviation of dpO_2 changed faster than 0.2% over ten minutes, P_{atm} changed by more than 0.1% over the air sampling period, or air temperature changed by more than 1°C over the air sampling period. The initial 10 minutes of measurements were removed in order to allow water to drip off of the sensor and reduce the effect of possible evaporative cooling.

Daytime (gray), and nighttime unfiltered (blue) and filtered (red) data for the OSP float are plotted in Figure 2.8. Mean standard deviations for unfiltered air periods were 2-3.5x larger than filtered air periods. As mentioned above, air periods that occurred during daylight had large standard deviations (error bars in Figure 2.8) and were biased high. During the period from Dec 2013 – Oct 2014 the OSP float began surfacing during the early morning instead of the middle of the night and this anomaly can be seen in the data.

In general, lower optode air measurements display a seasonal cycle that indicates higher values in the summer when surface waters are supersaturated and is likely the result of splashing by waves (see Bittig and Körtzinger 2015). This is especially evident in the unfiltered data, but is still partially visible in the filtered dataset. Overall, filtered air periods have the smallest standard deviations for both the upper and lower optodes. The remaining filtered air period averages are used to determine the initial calibration of pO_2 on deployment and any subsequent drift.

The black lines in Figure 2.8 are linear regressions against filtered air period dpO_2 for the OSP optodes. The y-intercept of the linear regression at the time of float deployment represents the sensor drift between the time of optode calibration and deployment. The slope of the linear regression is the rate of drift during the deployment. Confidence intervals plotted around the regression are ± 1 (gray area) and 2 (blue area) standard deviations. Air period averages were used to calculate linear regressions instead of all individual air measurements. This assumes that there is some significant variability between air periods and that measurements within each air period are not entirely independent. The OSP optodes measured pO_2 lower than expected atmospheric by -4.2 ± 0.1% (Upper) and -3.0 ± 0.1% (Lower, ± 1 σ) (Table 2.3). Note that the individual optode differences from expected are not the same and indicate optode-specific drift. The Winkler comparison cast for this float shows a difference between optode and Winkler of -4.5 ± 0.2% (upper) and -3.8 ± 0.2% (lower), which differs from the air calibration by 0.3 and 0.8%, respectively (Table 2.4).

Linear regressions for all KE floats were made against filtered air periods and are plotted with the regression lines and confidence intervals in Figure 2.9. Linear regressions are used because we are interested in correcting long-term drift only and do not think seasonal fluctuations are part of that drift. Regressions are made only on whole years of data to avoid seasonal biasing from incomplete years. The difference between Winkler comparison measurements and initial in situ air calibration is plotted with each optode's atmospheric measurements in Figure 2.9 (yellow squares). The average difference for all optodes between Winkler measured optode offset and dpO_2 from atmospheric calculations is -0.5 ± 0.7% (Winkler minus dpO_2, Table 2.4). The time and space differences between float profile measurements and Winkler comparison samples is a potential problem for calibration of floats using surface measurements on deployment. Comparison of temperature and salinity plots for float profiles and ship comparison casts indicated that 5 of the KE comparison casts sampled water with different properties than the matched float profiles (data not shown).

Any significant optode drift during deployment will show as a data trend away from the initial intercept in Figure 2.9 (dashed gray lines). To determine whether a given trend was measurable, confidence intervals around the linear regressions in Figures 2.8 and 2.9 were calculated as:

$$C.I._{\%} = t_{\left(1-\frac{q}{100}\right)[v]}\sqrt{\frac{s_{Y\cdot X}^2}{\sum x^2}} \tag{2.3}$$

where q is the percent confidence interval, t is the Students t-distribution critical value derived from a table of t-values (Rohlf and Sokal 2003) for the given confidence interval and degrees of freedom, v (number of measurements, n – 2), $\sum x^2$ is the sum of the square differences of x (time in days of each air period) and the mean time, and $s_{Y\cdot X}^2$, the unexplained variance (Sokal and Rohlf 2003). The unexplained variance is calculated from:

$$s_{Y\cdot X}^2 = \frac{\sum d_{Y\cdot X}^2}{v} \tag{2.4}$$

where $\sum d_{Y\cdot X}^2$ is the unexplained sum of squares, or the sum of the square difference between each air period average and the prediction for that time from the linear regression. For a time series with consistent variance, longer time periods over which measurements are taken (which increases $\sum x^2$) and more measurements (n, which increases v) will result in smaller confidence intervals.

Of the 13 optodes with long enough time series to check drift, 3 displayed measurable drift at 95% confidence intervals (2 σ, blue areas) and 9 were measurable at 68% (1 σ, gray areas). Both of the optodes on the OSP float are drifting at a rate of -0.5% yr^{-1} and the optode on float 5328, the southernmost KE float, has drifted at -0.4% yr^{-1}. The average in situ drift rate for all optodes is -0.1% yr^{-1}, with a range in most drift rates of -0.5 to 0.2% yr^{-1}. One outlier, the lower optode on float 8387 with a drift rate of 0.5% yr^{-1}, has a relatively large spread in the air data.

Plotting filtered atmospheric data for all KE optodes revealed excursions in $\mathrm{d}p\mathrm{O}_2$ at temperatures above 21°C for KE floats in warmer waters (data not shown). These temperatures fall outside of the lab water calibration range and were therefore removed from the regression to atmospheric data. Air measurements above 21°C for floats 5328, 7665, 8372, 8375, 8382, 8387, and 8394 are not plotted in Figure 2.9. Using the linear regression to remaining atmospheric data for each optode, we can determine a high temperature correction for those optodes by calculating the difference between actual air measurements and the linear fit to the filtered atmospheric data. This allows a final oxygen calculation for surface waters.

2.4 Discussion

2.4.1 Assessment of in situ atmospheric calibration

The OSP float was deployed 8 km from the OSP mooring site (50°N x 145°W, Figure 2.3). Mounted on the mooring bridle was an optode calibrated according to the same lab procedure described in 2.1 and subsequently corrected to Winkler measurements taken from the R/V Tully upon deployment in June 2012 and again in August 2012 and June 2013. In June 2013 a new mooring was deployed with an oxygen optode that was also calibrated to Winkler measurements on deployment and in August 2013 before an electrical malfunction in December 2013. A third mooring deployment in June 2014 provides another 5 months of Winkler calibrated data.

The continued proximity of the OSP float to the surface mooring provides a long-term source of comparison. The 2.5 year mooring time series (black line) is plotted in Figure 2.10 with the float surface supersaturation from each profile (blue line and x's). The mean difference between the mooring optode ΔO_2 calibrated to in situ Winkler measurements and float optode ΔO_2 calibrated to air measurements is 0.2%. This comparison is updated from Emerson and Bushinsky (2014) when only 1 year of float data was available. While we would not expect exact agreement between float and mooring given their spatial separation, there is no long-term bias between these two independently calibrated oxygen measurements.

In situ air calibrations naturally depend on our ability to accurately measure atmospheric oxygen. Splashing water, mismatches between measured pO_2 and pressure data, rapidly changing temperature, or any other factor that will impact dpO_2 and degrade the quality of the calibration. We approached these problems by raising the optode higher out of the water, making many measurements during each air period, and then filtering the data to remove likely bad data. Raising the optodes to 61cm reduced the average s.d. for air periods by half (Table 2.2). Lower optodes exhibited stronger seasonal cycles in dpO_2 than upper (Figure 2.9) and all of the KE lower optodes were taller than typical optode deployment height. Since there is no reason to expect the mean around the seasonal cycle in dpO_2 is the true value, a simple averaging will not suffice for determining the correct offset. It is probable that this cycle is biased by differences in wave energy, wind speed, and temperature changes throughout the year.

Bittig and Körtzinger (2015) adjust for wave splashing by assuming the optode is measuring a mix of water and air and adjust the data such that there is no difference between water and air measurements at 100% saturation. Implementing this method with nighttime data from the first year of data collected by the lower optode on the OSP float yields an initial offset of -2.8 ± 0.4%, comparable to the offset found in this study of -3.0 ± 0.1% (Table 2.3). The difference in confidence intervals may be due to the difference in time periods used for the offset calculation. However, the seasonal cycle in dpO_2 cannot be explained for all optodes by splashing. For example, the upper and lower optodes of float 8381 follow anti-correlated seasonal cycles (Figure 2.9). The lower optode dpO_2 maxima occur during the summer, when splashing by supersaturated water could explain elevated optode air measurements, but the upper optode measured minimum values in its seasonal cycle at these times.

2.4.2 Optode drift evaluation

The percent change in optode response calculated relative to air calibration on deployment for all optodes in this study is plotted in Figure 2.11A. Factory calibrations (black x's), lab calibrations (blue circles), and air calibrations illustrate a roughly linear drift prior to deployment. The linear relationship shows that the first order problem with the factory calibration is drift, rather than inaccuracy in the calibration. Plotting all optodes with multiple calibrations and normalizing to the [O_2] calculated using the air calibration on deployment yields an average drift of -7.2 ± 1.5% yr^{-1} at near saturation values. This drift rate is comparable to the initial, post factory calibration drift rate illustrated in D'Asaro and McNeil (2013) of ~6.3 % over the first year.

Post deployment drift is more than an order of magnitude lower than pre-deployment drift. The three optodes that showed measurable drift at a 95% confidence interval averaged drift of approximately -0.5% yr^{-1}. Of the 9 optodes that measurably drifted at a 68% confidence interval, 7 optodes displayed an average decrease in sensitivity of -0.4% yr^{-1} and 2 optodes increased in sensitivity by 0.4% yr^{-1}. All float optodes spend the majority of their time at ~1000 db in the dark, with temperatures that never vary more than a few degrees. Surface conditions for the two floats with optodes that showed measurable drift at 95% C.I. are very different. Float 8397 is in the northeast Pacific subarctic gyre where a strong seasonal cycle in light and temperature causes seasonal cycles in surface supersaturation of ~6-10%. Float 5328 is in the western side of the subtropical gyre where surface waters are ~15°C warmer and the seasonal amplitude of oxygen supersaturation is only ~4%. Most of the other surface conditions experienced by the floats fall in between these two extremes, suggesting optode-specific differences in drift rates rather than differences due to environmental conditions. Interestingly, all optodes presented in this paper were equipped with sensing foils cut from the same sheet. It is therefore unlikely that the observed differences in drift rates are due to variations in the sensing foils.

This is the first time drift has been measured in deployed Aanderaa optodes. Previous studies that found no drift in optodes deployed on profiling floats had a few significant differences from the current study. Takeshita et al. (2013) calibrated already deployed optodes using climatological data that could not resolve changes of less than several percent. Even at the highest rates of drift measured in this study, it is unlikely that any of these optodes will display a post-deployment drift of greater than 3% over their expected float lifetimes of 4-5 years. Johnson et al. (2015) applied an air calibration technique similar to what is done here but using only one air measurement each time a float surfaces. This introduces additional variance to the air measurements (Figure 2.7) that would make these small, but important rates of drift difficult to detect. Tengberg et al. (2006) and Bittig and Körtzinger (2015) each tested 1 optode on a profiling float for over a year and found no drift. However, in this study it appears that drift rate, and possibly direction, are optode specific and the particular optodes in those studies may not have drifted or drifted at rates too low to detect over the deployment period.

Over the 4-5 year expected lifetime of these floats, drift rates of -0.5% yr^{-1} are important for gas flux calculations. Assuming typical summertime conditions at OSP and an oxygen supersaturation of 4%, a -0.5% yr^{-1} reduction in measured saturation would reduce the oxygen flux out of the ocean by ~12% after one year and ~50% after 4 years (Liang et al. 2013; Wanninkhof 2014). Because of the asymmetry of O_2 supersaturation, this effect is also not uniform throughout the year. Wintertime errors in the oxygen flux would be even greater; assuming a typical surface undersaturation of -1% ΔO_2, a -0.5% error results in a 44% increase in the oxygen flux to the ocean while a -2% error results in an flux overestimate of 175%.

2.4.3 Low oxygen measurements

Determining oxygen accurately at these low concentrations is important for measuring and understanding oxygen minimum zones. The cutoff for severe hypoxia is ~22 μmol kg^{-1}, or ~10% saturation (Hofmann et al. 2011) which underscores the need to understand optode response and drift in this region of the calibration curve.

In order to monitor and correct for drift at low oxygen values, it is necessary to know how the calibration surface changes with drift. If drift is a change in sensitivity that is a uniform percent of measured pO_2, then calibration points at near saturation values can be used to adjust low oxygen values as well. The best evidence we have for how the optodes drift at low oxygen comes from the ship comparison casts in the Kuroshio Extension, where Winkler samples in the oxygen minimum can be compared to the optode drift corrected to the atmospheric calibrations.

The oxygen minimum in this region is between 1000-1400m deep and has a concentration of ~[40] μmol kg^{-1}, or ~10% saturation. Drift calculated from the response change between factory calibrations, lab calibrations, and in situ Winkler measurements yields a change in optode response of -23 ± 3.2%, in the oxygen minimum, far higher than drift measured in the surface ocean at saturation (Figure 2.11). While Winkler titrations are less accurate at low $[O_2]$, this rate is dependent on multiple Winkler replicates averaged within the oxygen minimum and larger than could be explained by titration error.

Johnson et al. (2015) argues that a simple gain correction can be used with atmospheric measurements for the entire water column, based on the minimal difference between factory calibrated optode measurements in oxygen deficient zones and zero. The $[O_2]$ offset for the KE floats plotted in Figures. 2.11A and 2.11B is 19.3 ± 4.2 μmol kg^{-1} at saturation and 7.0 ± 0.7 μmol kg^{-1} in the oxygen minimum implying that either an offset correction or single drift rate can be applied linearly to the entire calibration surface. Bittig and Körtzinger (2015) provide more evidence for linear drift across all oxygen saturations by performing multiple calibrations on an optode through time. They do observe an “oxygen independent offset” near zero which could be similar to what we observe here.

2.5 Conclusions

Air measurements provide a method for accurate in situ calibration of oxygen optodes. We have demonstrated that they can be used to determine both initial offset and subsequent drift to a few tenths of a percent. Raising the optodes further out of the water provides a cleaner signal with less noise from splashing waves, making it easier to characterize long-term drift. Optodes drift rapidly prior to deployment, and we have shown here evidence for continued drift after deployment in 3 optodes using a 95% confidence interval and 9 optodes using a 68% confidence interval. The observed drift is great enough that it will significantly impact air-sea oxygen flux calculations from these floats. It is unknown whether all optodes continue to drift post deployment, but the observed drift in ~1/4 to 1/2 of optodes in this study argues strongly for the need to monitor in situ drift rates in order to calculate air-sea gas fluxes.

Optodes show promise for low oxygen measurements, but drift needs to be better understood and categorized to explain the differences seen here between drift at saturation and drift at low oxygen values. Aspects of the method described here, such as nighttime air measurements and filtering of atmospheric data can be applied to currently deployed Argo oxygen floats or used to guide interpretation of float air data. Future deployment of SOS-Argo floats or similar floats with elevated optodes capable of atmospheric measurement will help to greatly enhance the utility of profiling floats for determining air-sea oxygen fluxes throughout the ocean.

To summarize, we recommend the following for future in situ atmospheric calibrations:

- Measurements should be made at night or only nighttime data should be used for air calibrations
- Repeated measurements should be made at each air period, both because the initial measurement may not be representative of an average and multiple measurements allow filtering to remove highly variable air periods
- Filtering atmospheric data can reduce variance in air measurements and improve accuracy if air periods are biased during certain times of the year
- Raising optodes higher out of the water will reduce the variance in air periods

The following uncertainties must still be dealt with:

- Optode calibrations must be performed across the entire temperature range expected for atmospheric conditions
- A simple gain correction does not appear to adequately correct low oxygen data

2.6 Tables

Table 2.1. Summary of lab calibration fits and removed points.

	Lab Calibration			
SN	Initial	Removed	Final	RMSE (%)
OSP				
895	60	35	25	0.49
896	59	30	29	0.71
KE				
842	52	9	43	0.20
852	52	7	45	0.20
854	31	2	29	0.30
861	31	3	28	0.21
863	52	6	46	0.21
865	52	8	44	0.18
866	52	14	38	0.27
890	31	2	29	0.33
891	32	3	29	0.35
892	31	2	29	0.27
894	31	1	30	0.32
897	52	8	44	0.20
898	32	4	28	0.45
938	52	7	45	0.27
941	52	10	42	0.37
Mean				0.31

Laboratory optode calibrations against Winkler measurements. Each optode is an Aanderaa 4330 listed by serial number (SN). The number of Winkler replicate and optode response pairings across all oxygen saturations and temperatures are indicated as those initially collected (Initial), the number of points removed (Removed), and the final number of points (Final) used for the calibration. Calibration coefficients and surfaces were fit to the data for each optode as in Figure 2.1. Root mean square error (RMSE) is calculated from the residuals of the Winkler replicates minus the optode oxygen calculated using the surface fit.

Table 2.2. Mean standard deviation for upper and lower optodes.

	Mean air period σ	
Float SN	61 cm	25 cm
8397[1]	0.23	0.35
8372	0.38	0.91
7661	0.44	0.92
8381	0.26	0.49
8382	0.32	0.70
8387	0.30	0.80

Mean standard deviation for upper and lower optodes on all dual optode floats in this study. Each air period, consisting of ~30 atmospheric measurements is averaged, with the mean standard deviation shown here. Mean s.d. for lower optodes was 2x that of upper optodes.

[1] The lower optode on float 8397 was mounted on a 10 cm stalk.

Table 2.3. Linear regressions to unfiltered and filtered air period averages.

				Unfiltered air period averages			Filtered Air period averages			Differences (unfiltered – filtered)	
UW Float #	WMO #	Optode SN	Position (Upper/Lower)	n	Intercept (% ± σ)	Slope (% yr^{-1} ± σ)	n	Intercept (% ± σ)	Slope (% yr^{-1} ± σ)	Intercept difference	Slope difference
8937	5903743	896	U	81	-4.1 ± 0.1	-0.5 ± 0.0	63	-4.2 ± 0.1	-0.5 ± 0.0	0.1	0.0
		895	L	81	-3.0 ± 0.1	-0.6 ± 0.0	48	-3.0 ± 0.1	-0.5 ± 0.1	0.0	0.0
5328	5904029	852	U	148	-1.6 ± 0.1	-0.3 ± 0.1	43	-1.6 ± 0.1	-0.4 ± 0.1	0.0	0.1
8372	5904026	941	U	147	-3.0 ± 0.1	-0.2 ± 0.1	65	-3.2 ± 0.1	-0.2 ± 0.1	0.3	0.0
		938	L	147	-3.9 ± 0.1	-0.3 ± 0.1	16	-3.7 ± 0.1	-0.2 ± 0.1	-0.1	-0.1
8375	5904030	898	U	137	-3.4 ± 0.2	-0.4 ± 0.2	75	-3.2 ± 0.2	-0.3 ± 0.2	-0.1	-0.1
8387	5904027	897	U	139	-2.4 ± 0.1	-0.1 ± 0.1	84	-2.7 ± 0.1	0.1 ± 0.1	0.3	-0.2
		863	L	139	-4.2 ± 0.1	0.0 ± 0.1	26	-4.3 ± 0.2	0.5 ± 0.2	0.1	-0.4
8394	5904031	861	U	139	-3.3 ± 0.2	0.3 ± 0.1	75	-2.6 ± 0.1	0.0 ± 0.1	-0.7	0.3
7661	5904024	894	U	27	-1.9 ± 0.2						
		892	L	27	-4.3 ± 0.2						
7657	5904032	842	U	21	-3.7 ± 0.2						
8382	5904025	890	U	142	-5.6 ± 0.2	0.1 ± 0.2	63	-5.0 ± 0.2	0.2 ± 0.2	-0.7	-0.1
		891	L	142	-3.7 ± 0.1	0.0 ± 0.1	13	-3.1 ± 0.2	-0.2 ± 0.2	-0.6	0.2
7665	5904033	866	U	145	-2.6 ± 0.1	-0.1 ± 0.1	85	-2.7 ± 0.1	0.0 ± 0.1	0.1	-0.1
8381	5904028	854	U	138	-2.8 ± 0.1	0.2 ± 0.1	116	-2.8 ± 0.1	0.2 ± 0.1	0.0	0.0
		865	L	138	-3.4 ± 0.1	0.1 ± 0.1	46	-2.8 ± 0.2	-0.3 ±0.1	-0.6	0.4
Mean					± 0.1	-0.13 ± 0.1		± 0.1	-0.12 ± 0.1		

Comparison of intercept and slopes calculated for linear regressions to unfiltered and filtered air period averages. For each optode, UW float number, World Meteorological Organization (WMO) number, serial number (SN) of optode, position on the float (upper are on a 61 cm stalk, lower on a 25 cm stalk), n (the number of air period averages used in the regression), and the intercept and slope ± 1 σ are listed. Unfiltered data include all air periods for a float, while filtered data removed air periods during which atmospheric conditions were rapidly changing as described in section 2.3.2. The differences between unfiltered and filtered intercepts and slopes area also calculated. Floats 7661 and 7657 did not operate for long enough to filter data or calculate drift rates. No means are calculated for the intercepts as these represent optode specific drift from lab calibrations. Optodes with more time in between calibration and deployment will drift more. Pre-deployment drift rates are plotted in Figure 2.11.

Table 2.4. Comparison of air calibration to Winkler measurements.

Float SN	Optode SN	Position (Upper/Lower)	Air calibration intercept (% ± σ)	Winkler Cal. (% ± σ)	Difference (Winkler – Air calibration)
8937	896	U	-4.2 ± 0.1	-4.5 ± 0.2	-0.3
	895	L	-3.0 ± 0.1	-3.8 ± 0.2	-0.8
5328	852	U	-1.6 ± 0.1	-2.3 ± 0.2	-0.7
8372	941	U	-3.2 ± 0.1	-3.5 ± 0.1	-0.2
	938	L	-3.7 ± 0.1	-4.2 ± 0.1	-0.5
8375	898	U	-3.2 ± 0.2	-4.6 ± 0.2	-1.4
8387	897	U	-2.7 ± 0.1	-2.8 ± 0.4	-0.2
	863	L	-4.3 ± 0.2	-4.4 ± 0.4	-0.1
8394	861	U	-2.6 ± 0.1	-3.1 ± 1.0	-0.6
8382	890	U	-5.0 ± 0.2	-4.2 ± 0.3	0.8
	891	L	-3.1 ± 0.2	-2.4 ± 0.3	0.7
7665	866	U	-2.7 ± 0.1	-3.5 ± 0.0	-0.8
				Mean difference:	-0.5 ± 0.7

Initial air calibration of optodes compared to Winkler measurements from nearby hydrocasts. Air calibrations are based on the intercept at time of deployment of the linear regression to filtered atmospheric data in Figure 2.9. Winkler calibration is the mean and standard deviation of surface measurements from deployment and re-visitation hydrocasts. Winklers for float 8381 were not matched well in space or time and therefore not included in this comparison.

2.7 Figures

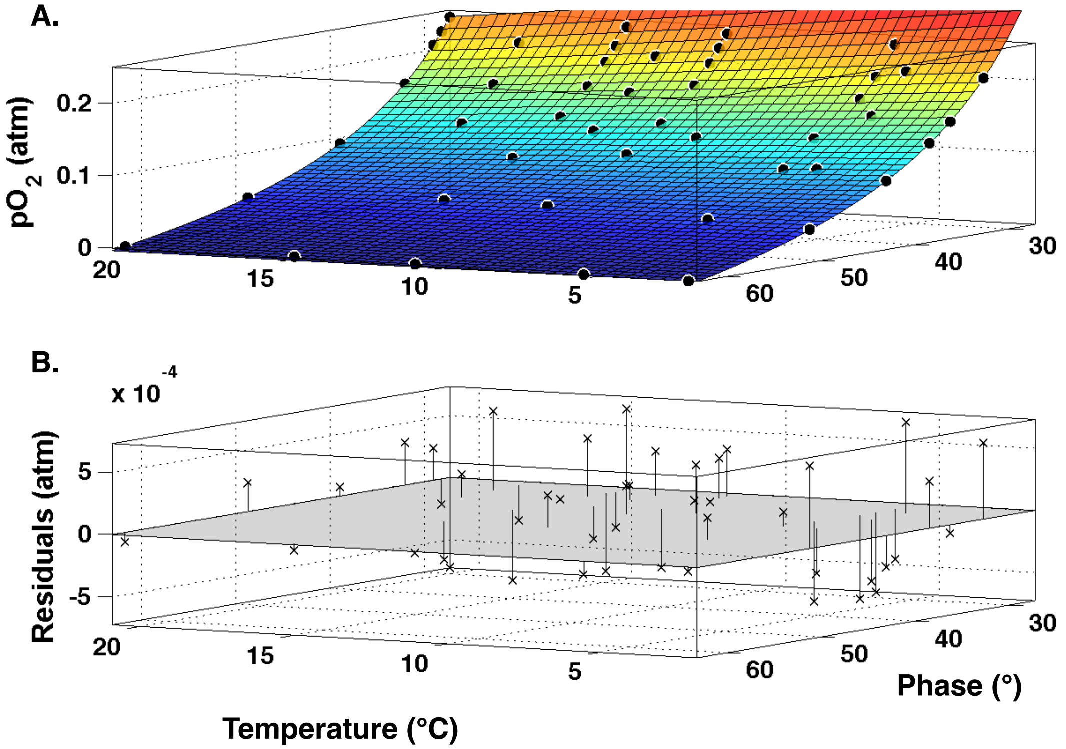

Figure 2.1. Example calibration surface fit and residuals for optode 863, deployed on float 8387 in the Kuroshio Extension. Optode measured temperature and phase were matched to Winkler replicates (black circles, A). Calibration coefficients were determined according to Uchida et al. (2008), shown as the colored surface, with colors representing levels of equal *pO_2*. Residual *pO_2* was determined for each Winkler replicate (B). Calibration points that do not meet measurement criteria were removed (see text): 4 data points were removed from this calibration because replicate Winkler measurements were greater than 0.2%, 0 points were removed because the optode phase measurement drifted by more than 0.05% during Winkler sampling, and 2 points were removed because residuals fell outside of 2 s.d. of the mean surface. A total of 6 out of 52 calibration points removed before the final coefficient determination, which was typical of most optode calibrations.

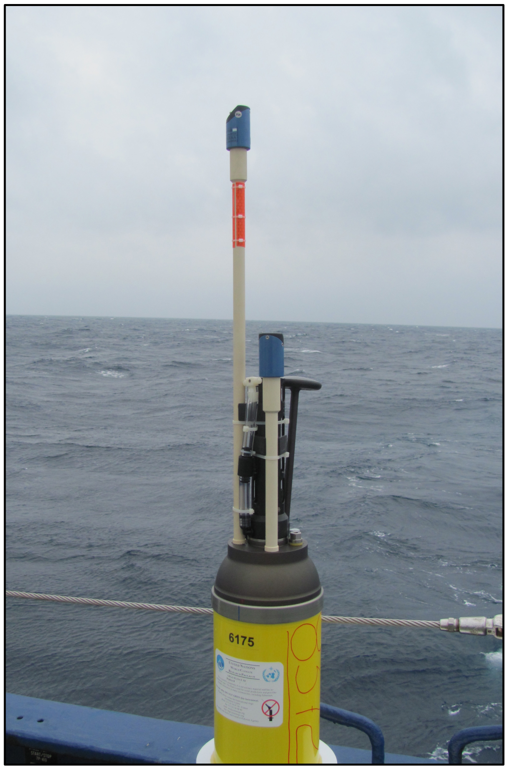

Figure 2.2. An SOS-Argo float in the dual optode configuration bound for deployment in the Kuroshio Extension. Both optode stalks are supported with cable ties and brackets against the CTD mast. 5 floats deployed in the KE had this configuration of two optodes, with the higher optode at 61 cm above the float end cap and one optode at 25 cm above the end cap. The other 5 floats only had one optode in the upper position. The SOS-Argo float deployed at OSP had two optodes, with the lower optode only 6 cm above the end cap.

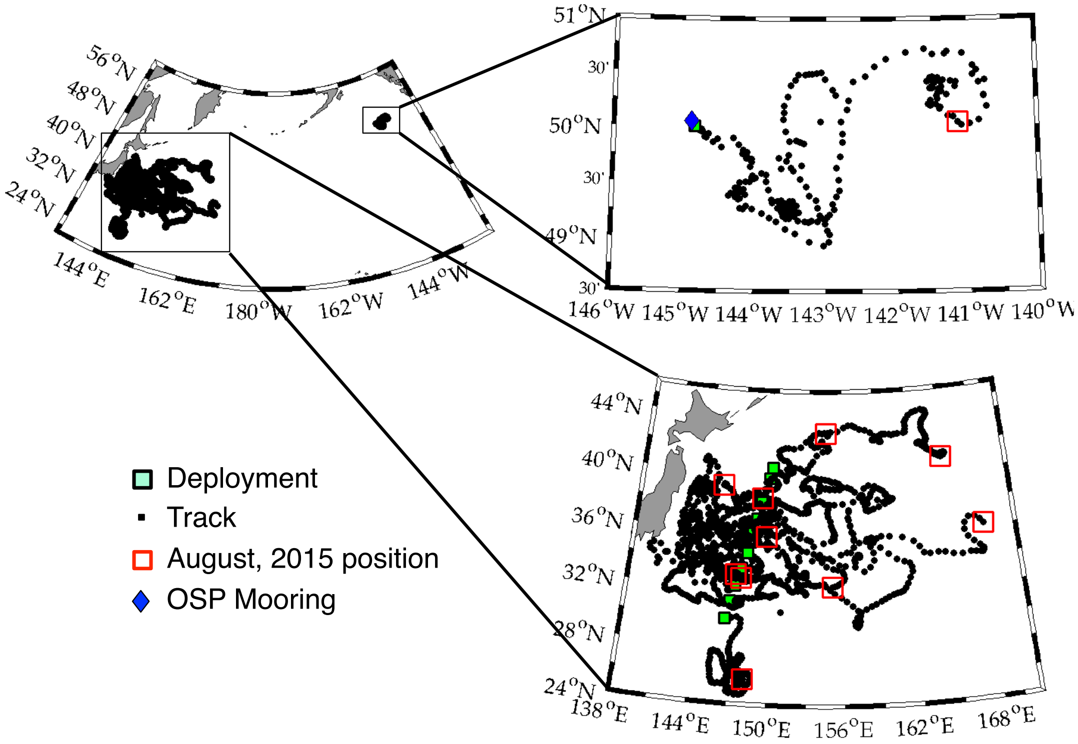

Figure 2.3. SOS-Argo float deployment locations and tracks. Float deployment locations are indicated by green squares, drift tracks by black points, and location as of August, 2015 by red squares. The OSP float (upper right) was deployed at 50.0 N, 144.8 W on June 2, 2012, near the OSP mooring. Its proximity to the mooring and the oxygen optode on its bridle allowed for validation of the in situ air calibration method. The Kuroshio Extension float deployments were from February-March 2013.

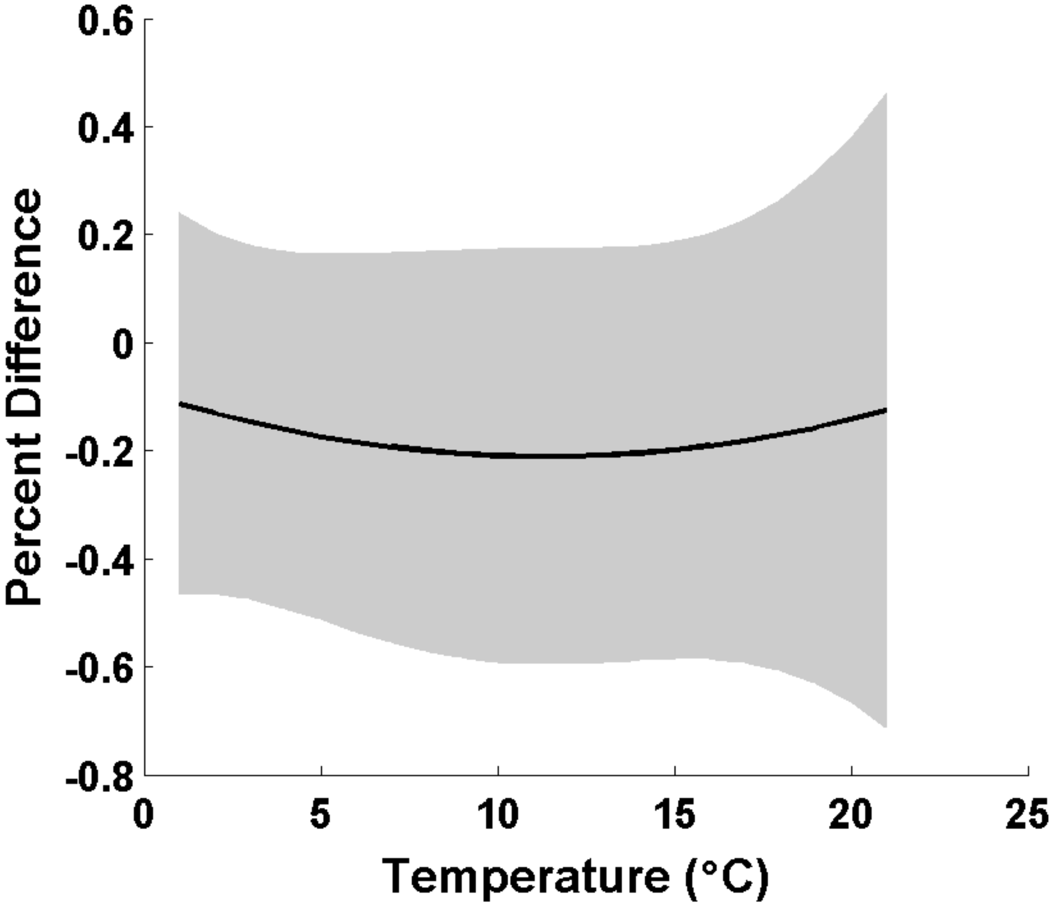

Figure 2.4. Percent difference between optode pO_2 air measurements and calculated atmospheric pO_2 according to equation 2.2 in laboratory experiments with 15 Aanderaa optodes. The average of all optodes is shown with the black line and the ± 1 s.d. is in gray.

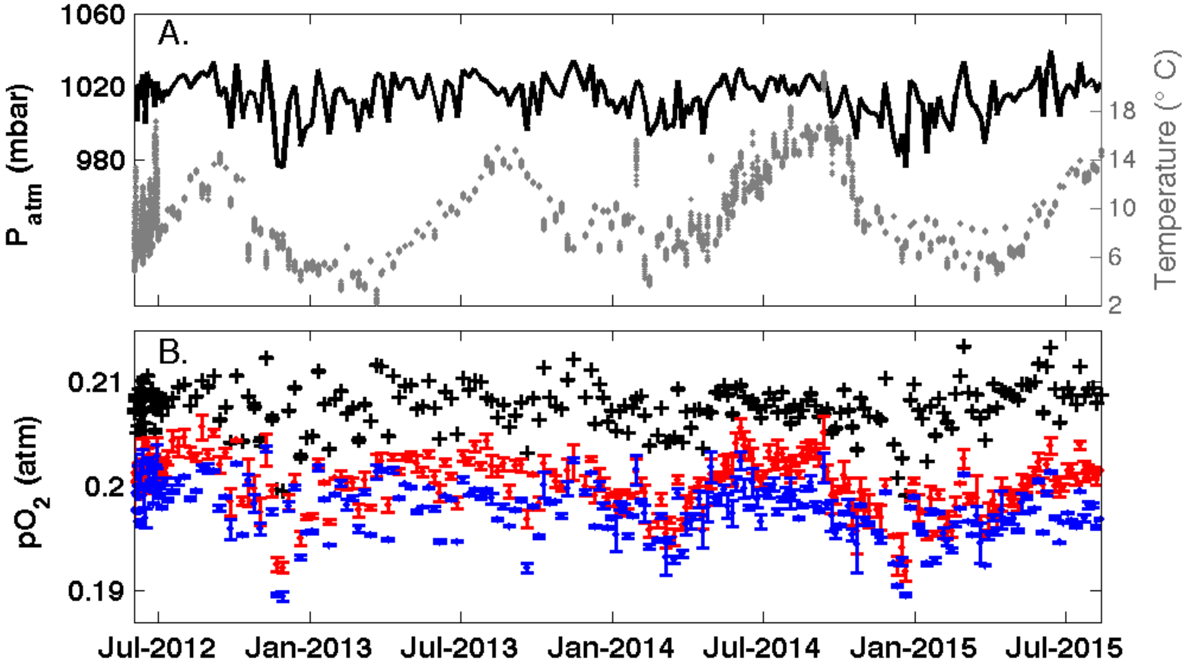

Figure 2.5. Atmospheric conditions and upper and lower optode pO_2 for OSP float. (A) Atmospheric pressure (black) and optode temperature in air (gray). (B) Black symbols are atmospheric pO_2 calculated according to equation (2.2), using NCEP determined sea level pressure and relative humidity. During each air period, measurements were made every 2 minutes for ~1 hour. Blue and red symbols are upper and lower optode air period averaged pO_2, respectively. The mean standard deviation for all air period averages (error bars, ± 1 s.d.) is ± 0.23% for the upper optode and ± 0.35% for the lower.

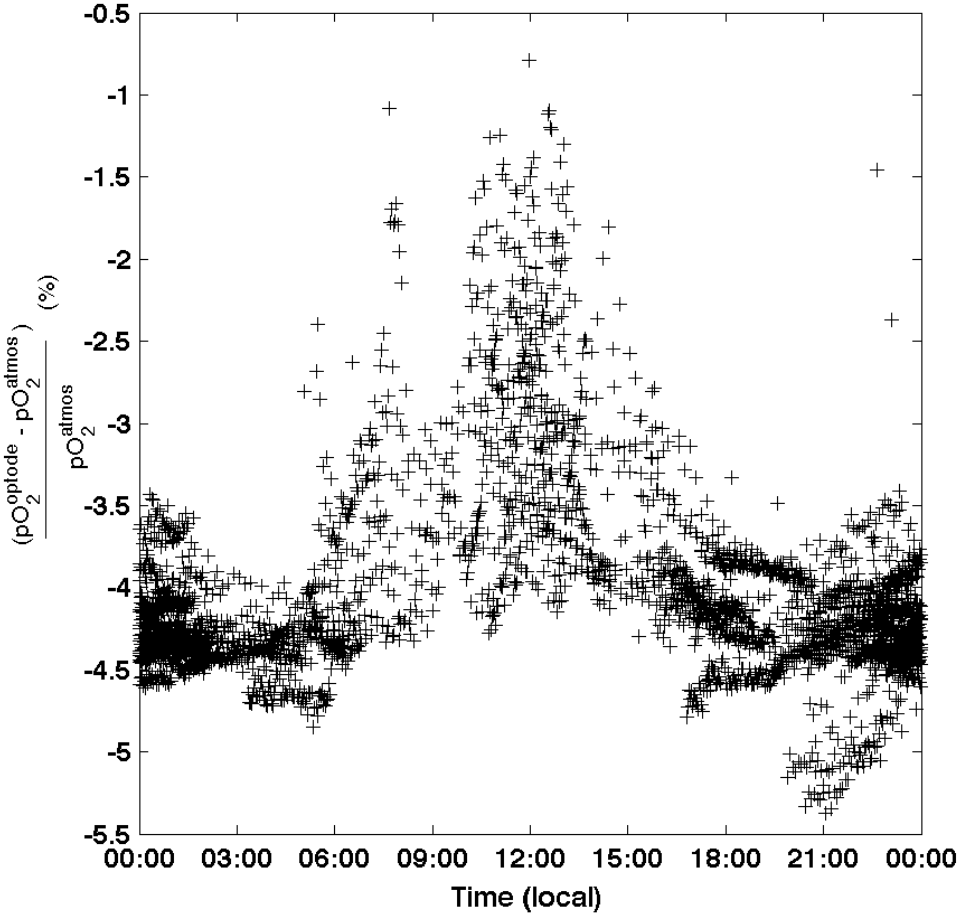

Figure 2.6. Uncorrected optode air measurements vs. local time of day. Air measurements from the OSP upper optode during the first 6 months of deployment are plotted as the percent difference between optode and atmospheric pO_2 determined using NCEP atmospheric data and equation 2.2. Local noon corresponds to the highest mean and variance in optode air measurements. After determination of this relationship surface measurements were shifted to nighttime only.

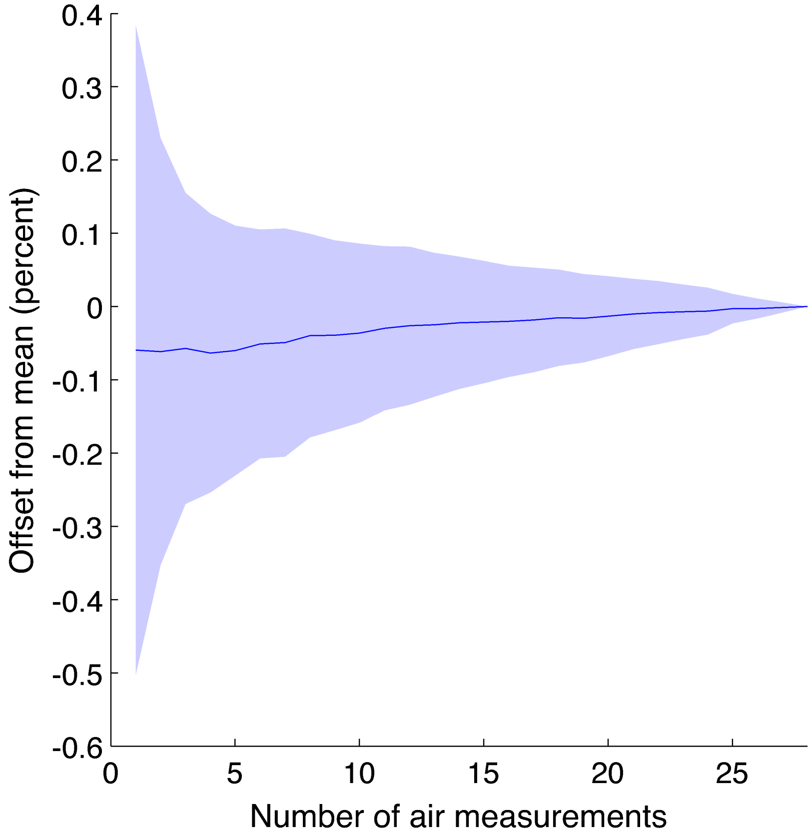

Figure 2.7. Optode air period mean offsets with increasing numbers of atmospheric measurements. After each profile, the optode, mounted on a 61cm stalk, made measurements every 2 minutes for ~1 hour. For each surface air period, the mean percent difference from atmospheric pO_2 is calculated with all points (n=28) and subtracted from means calculated with increasing numbers of data points. The blue line is the mean and blue area the standard deviation of 171 nighttime air periods for a representative optode on a float deployed in the Kuroshio Extension (SN 8381). Averaging more air measurements reduces the mean standard deviation of the air period offsets. For 14 optodes, the mean standard deviation of the first measurement is ± 0.61%. This decreases to ± 0.17% after 10 measurements and ± 0.08% after 20 measurements. By definition, at 28 measurements, the mean standard deviation is 0.

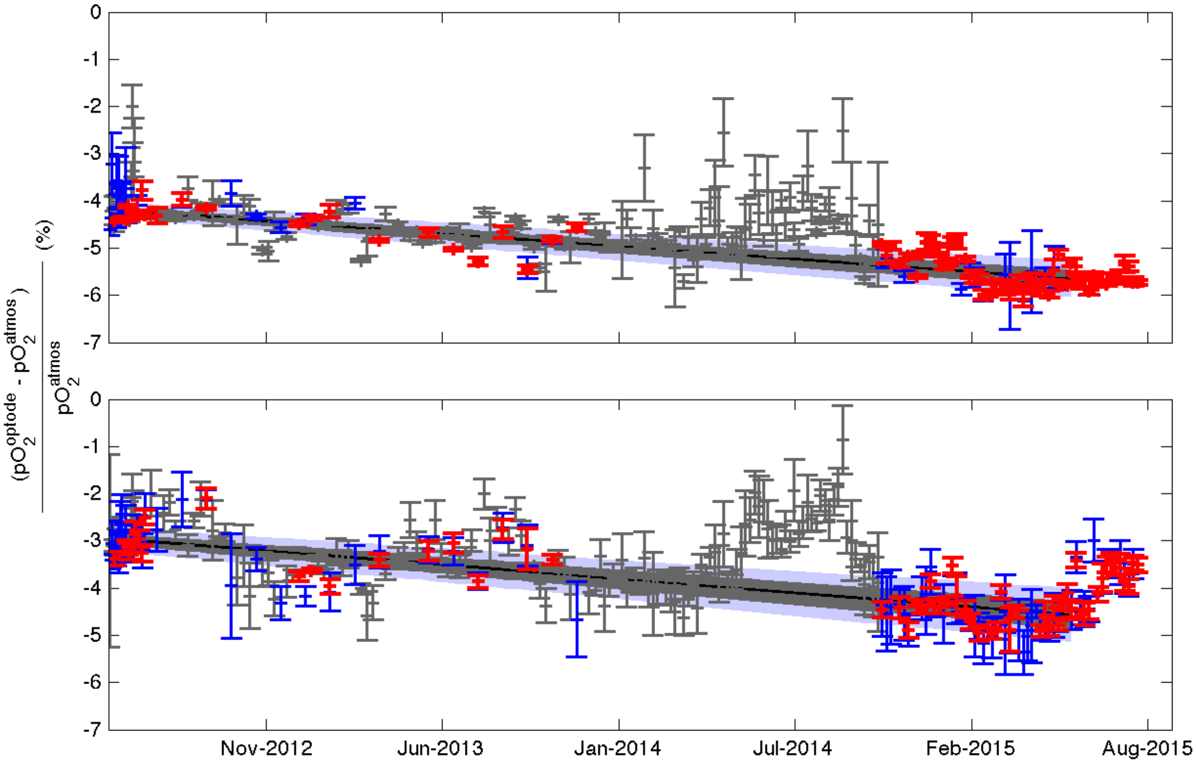

Figure 2.8. Comparison between optode air measurement and calculated pO_2 over three years of the OSP deployment for the upper (top) and lower (bottom) optodes. Percent difference between optode pO_2 calculated using laboratory calibrations and atmospheric pO_2 from equation (2.2) is plotted for all air periods (gray), nighttime (blue), and nighttime that passed the filter described in section 3.2 (red). Error bars represent ± 1 s.d. around the mean for each air period. Solid black lines are the linear regression to the filtered (red) measurements, from which the offsets are used to correct the data in Figure 2.9. The pronounced seasonal cycle in the lower optode is likely due to splashing from waves or spray. During the period from December 2013 to September 2014 the floats were surfacing during daytime, which is the reason for the departure from the trend and the large standard deviation during this time. Linear regressions to the filtered data are black lines, bounded by ± 1 σ (gray areas) and ± 2 σ (blue areas) confidence intervals calculated according to equations (2.3) and (2.4).

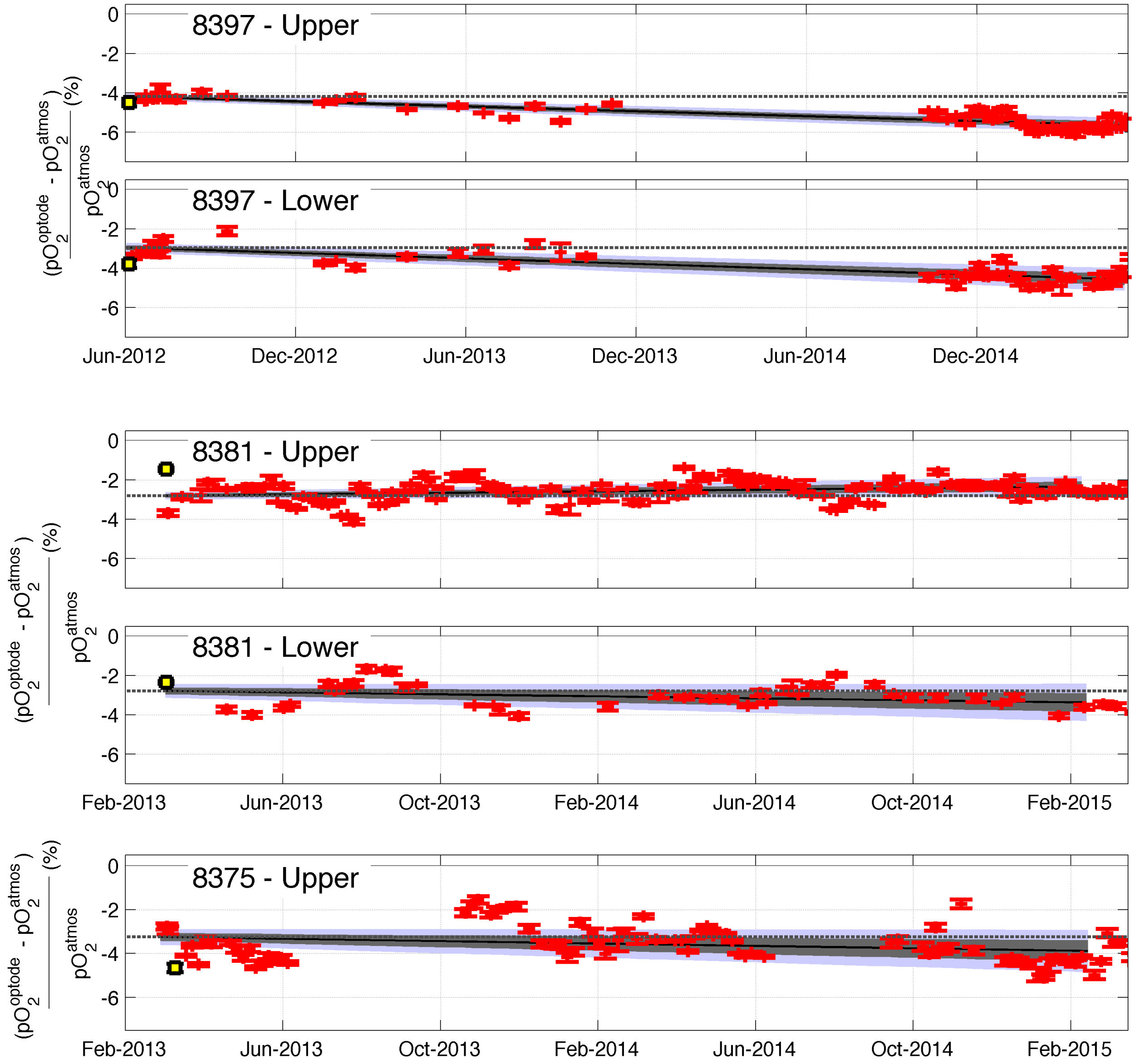

Figure 2.9. Filtered air measurements from 14 optodes over ~two annual cycles. Red symbols are the percent difference between optode and atmospheric pO_2 calculated from equation (2.2). Error bars represent ± 1 s.d. of the mean for each air period. Data from upper, and lower if present, optodes are plotted for all floats and have been filtered according to the criteria outlined in section 2.3.2. Solid black lines are linear regressions to dpO_2, with ± 1 σ and ± 2 σ confidence intervals in gray and blue areas, respectively. Dashed black lines are the intercepts of the linear regressions calculated at time of deployment, which represents the initial in situ calibration of the optode on deployment and the drift since laboratory calibration (Table 2.3). Data trends away

from the initial intercept lines indicates drift. For 3 of the 14 optodes, drift was measurable at ± 2 σ and for 9 of 14 optodes drift was measurable at ± 1 σ. Yellow squares are the difference between Winkler and optode measurements matched for calibration casts (Table 2.4). Note that the time scale for float 8397, deployed at OSP, starts one year earlier than the rest of the floats.

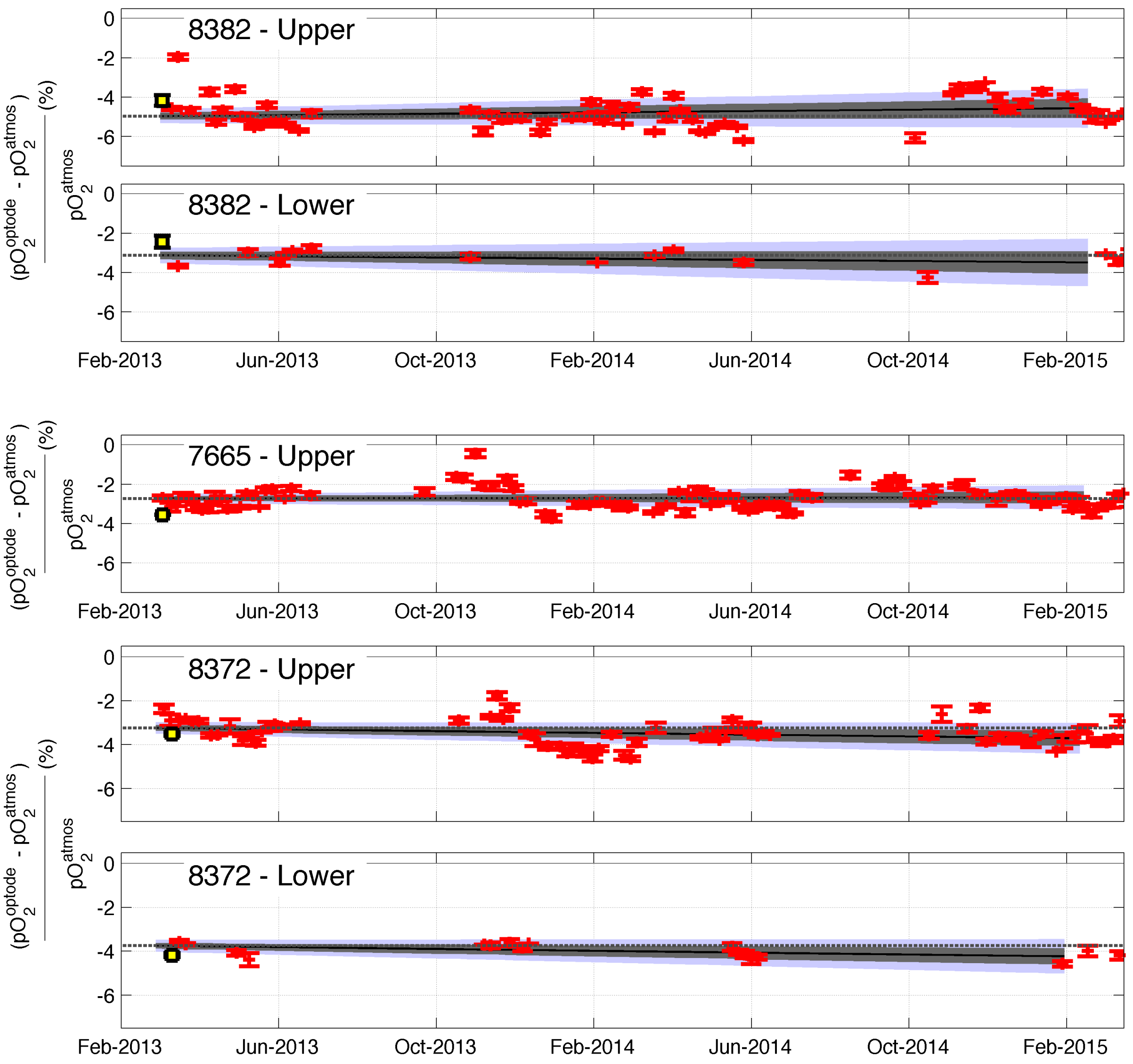

Figure 2.9 (continued).

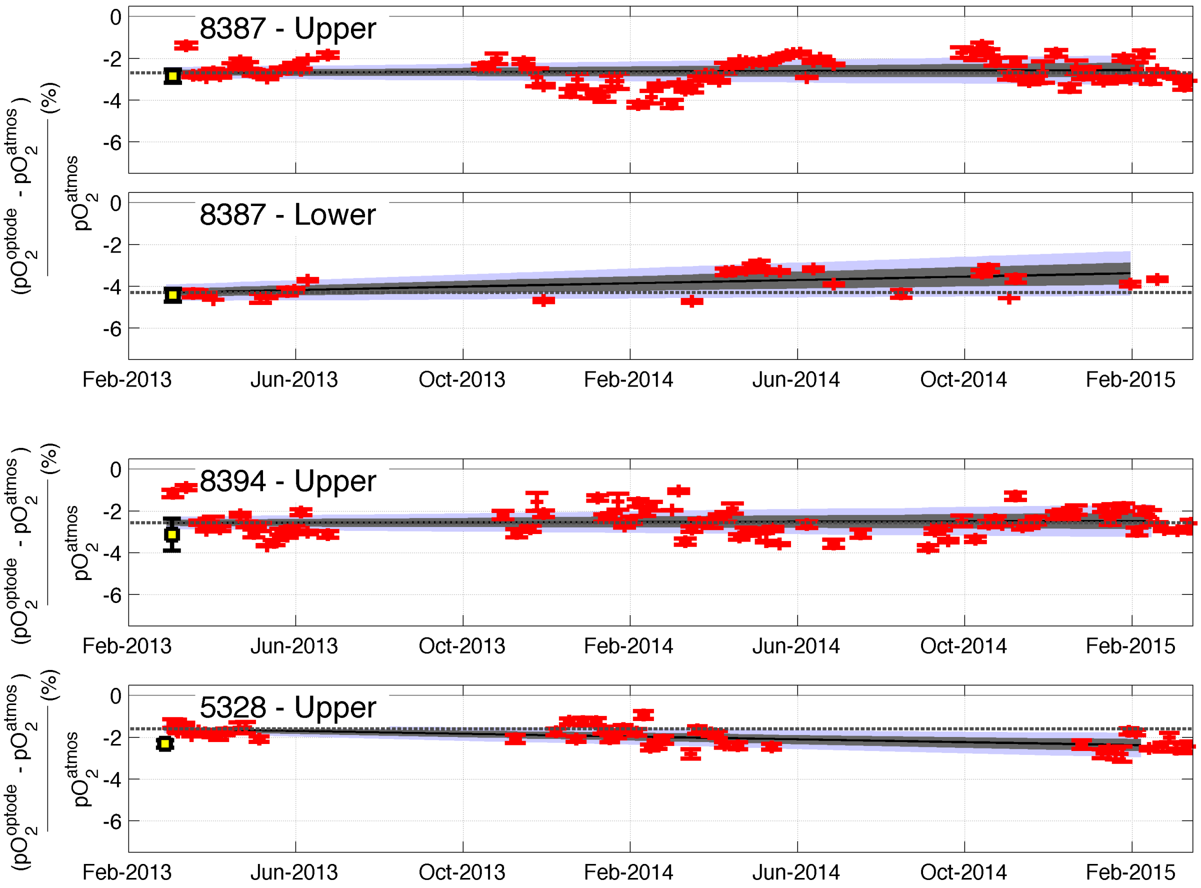

Figure 2.9 (continued).

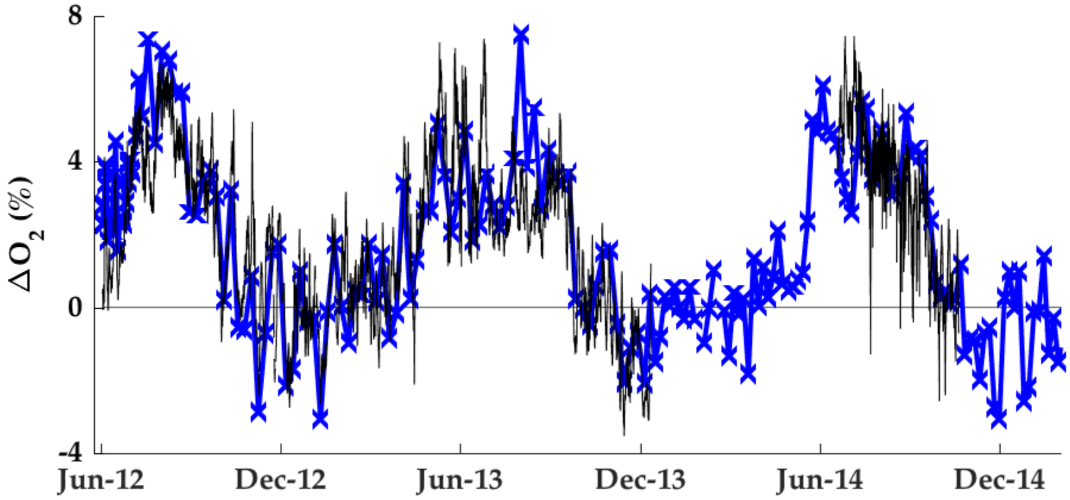

Figure 2.10. Surface ocean oxygen supersaturation in the subarctic Pacific. O_2 concentrations were determined from optodes on a mooring at OSP (black) and an Argo float (blue). Mooring data are corrected to O_2 concentration determined by Winkler titrations sampled on deployment and subsequently in August 2012, February 2012, June 2013, and August 2013. Float data were calibrated to air measurements for both initial offset and subsequent drift.

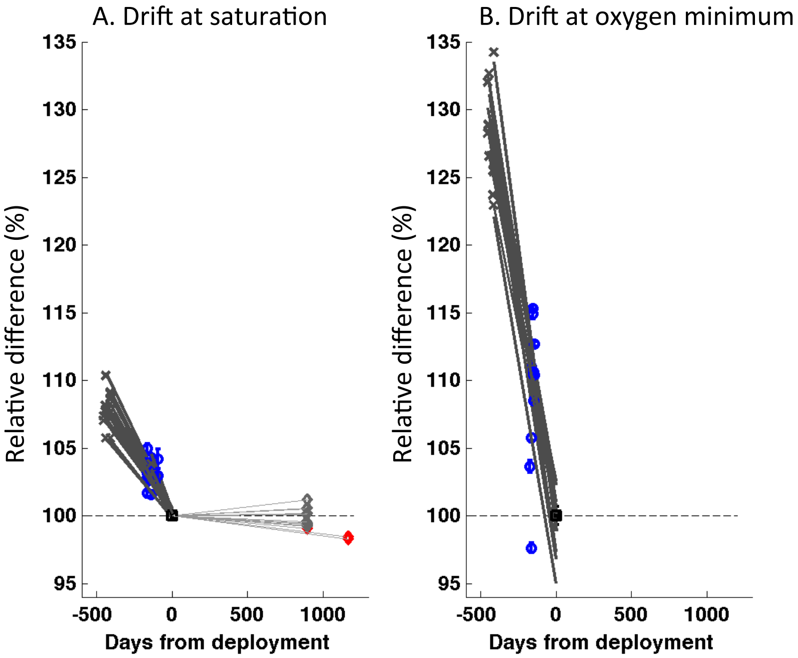

Figure 2.11. The change in optode sensitivity versus time in surface waters (ave. [O_2] 275 µmol kg^{-1}) and at the O_2 minimum (ave. [O_2] 40 µmol kg^{-1}). Percent change in optode sensitivity relative to that calculated at deployment is on the Y-axis. Near atmospheric measurements (A) are calculated using: factory calibration (gray x's), lab calibrations (blue circles), in situ atmospheric calibrations (black square), and in situ drift rates (gray and red diamonds). Oxygen minimum values are the percent differences of the factory calibrations (gray x's) and laboratory calibrations (blue circles) plotted relative to Winkler-determined O_2 values from one of the deployment casts (black square). Black lines in both plots are the linear fit to pre-deployment values with a slope of -7.2 ± 1.5% yr^{-1} at saturation and -23 ± 3.2% yr^{-1} in the oxygen minimum. Gray lines (A) are the drift rate post-deployment in the surface ocean. Red symbols indicate the three drift rates that are measurable at a 95% confidence interval.

Chapter 3

Marine biological production from remote in situ oxygen measurements

Abstract

Evaluating the organic carbon flux from the surface ocean to the interior (the marine biological pump) is essential for predictions of ocean carbon cycle feedback to climate change. One approach for determining these fluxes is to measure the concentration of oxygen in the upper ocean over a seasonal cycle, calculate the net O_2 flux using an upper ocean model, and then use a stoichiometric relationship between oxygen evolved and organic carbon produced. Applying this tracer in a variety of ocean areas over seasonal cycles requires accurate O_2 measurements on autonomous vehicles. Here we demonstrate this approach using an O_2 sensor on a profiling float that is periodically calibrated against atmospheric pO_2. Using accurate data and a model that includes all physical and biological processes influencing oxygen, we determine an annual net community production (ANCP) of 0.7 ± 0.5 mol C m^{-2} yr^{-1} in the Northeast Pacific Ocean (50°N, 145°W) from June 2012 to June 2013. There is a strong seasonal cycle in net biological oxygen production with wintertime fluxes caused by bubble processes critical to determining the annual flux. Approximately 50% of net autotrophic production during summer months is consumed by net respiration during the winter. The result is a biological pump in the subarctic ocean that is less than that determined by similar methods in the subtropics to the south, and significantly lower than that predicted by satellite remote sensing and global circulation models.

3.1 Introduction

Net carbon export from the upper ocean draws CO_2 from the atmosphere to the ocean and fuels respiration in the aphotic deep sea (e.g., Toggweiler and Sarmiento 1985; Volk and Liu 1988). While ocean climate models predict that feedback to the future levels of atmospheric pCO_2 caused by changes in the annual net carbon production (ANCP) should be of second order (Bopp et al. 2013), climate induced changes in the biological pump will have an important influence on the distribution and stability of the oxygen minimum zones of the ocean (Hofmann and Schellnhuber 2009; Kwon et al. 2009). The location and intensity of low oxygen concentrations is important for the survival of benthic organisms and greatly influences the nitrogen cycle (Altabet 2007; Deutsch et al. 2007).

There have been several recent attempts to use satellite remote sensing to determine the global distribution of the biological pump (Laws et al. 2011; Westberry et al. 2012; Siegel et al. 2014). Net biological carbon export determined in this way is often used as the boundary condition for the biogeochemical component of climate models (Yool et al. 2013). The remote-sensing based methods predict strong geographic variability in the biological pump—variations of at least a factor of four between the subtropical lows and higher values in the equator and subarctic latitudes (Laws et al. 2011; Westberry et al. 2012). Verifications of the satellite-determined carbon export have been attempted locally but are limited to select locations were it has been possible to do time-series studies of upper ocean mass balances of carbon, oxygen and nutrients (Juranek et al. 2012; Emerson 2014). A compilation of annual organic carbon export estimates by mass balance methods indicates that they range between 2 and 4 mol C m^{-2} yr^{-1} in the open ocean with no clear latitudinal dependence (see Emerson (2014), Table 2), but with near-shore values that are about twice this (Munro et al. 2013).

It is unresolved whether satellite-predicted carbon export values are more variable than reality or if the experimental results are simply too few to capture true ocean variability. This conundrum can be solved by a much broader distribution of ANCP determinations, but it must be done primarily by in situ measurements on autonomous platforms because of the great expense of ship-based annual time-series measurements. A method of achieving these ends is instrumenting profiling floats and gliders with oxygen sensors (Gruber et al. 2009; Johnson et al. 2009). Only a few studies of upper ocean oxygen mass balance have been done this way (Nicholson et al. 2008; Riser and Johnson 2008; Fiedler et al. 2013), however, because of accuracy issues with autonomous oxygen sensors. Calibration drift (D'Asaro and McNeil 2013) has necessitated in situ calibration of oxygen sensors in order to achieve sufficient accuracy for determining air-sea oxygen fluxes. Aanderaa optodes, the sensors currently used most frequently on autonomous vehicles, are more stable in the field than in the lab, but few long-term calibrations of deployed sensors have been conducted to establish stability at the accuracy needed to resolve air-sea gas exchange (Takeshita et al. 2013; Emerson and Bushinsky 2014).

Open ocean surface oxygen concentrations depart by only a few percent from atmospheric equilibrium (e.g. Emerson et al. 2008) requiring accuracies on the order of ± 0.2-0.4 % to determine air-water exchange fluxes. We achieve these accuracies by calibrating the Aanderaa optodes in the laboratory as a function of temperature and oxygen concentration, and then calibrating them in situ against atmospheric pO_2 to determine the air-water difference in pO_2 when the floats surface after collecting ascending profiles of T, S, and O_2. Performing multiple calibrations may eventually prove to be unnecessary, but the most important part for long-term data interpretation will be the in situ atmospheric calibrations. Much of the calibration procedure is described elsewhere (Bushinsky and Emerson 2013; Emerson and Bushinsky 2014; Bushinsky et al. 2015).

We present a seasonal cycle of oxygen data from a profiling float deployed near Ocean Station Papa (OSP, 50°N x 145°W). OSP is a time series site with a long history of O_2 measurements and prior mass balance estimates of C export. Production in the region is controlled by light and iron availability resulting in a strong seasonal cycle. We solve the problem of accuracy by in situ calibration of the sensor against the atmosphere and show that these data can be interpreted in terms of annual net community production and biological carbon export. It should now be possible to apply this method widely to many ocean locations and, together with satellite-determined remote sensing, evaluate the global geographic distribution of the biological pump and its evolution with time.

3.2 Methods

3.2.1 Optode Calibration and Float Deployment

Oxygen concentrations were determined using an Aanderaa optode sensor on a ~60 cm long polyether ether ketone pole attached to the end cap of an Argo float constructed at the University of Washington. This insures that the optode will measure purely atmospheric pO_2 rather than a mixture of surface ocean and atmosphere because of being splashed by surface ocean water. Firmware is adjusted to continue reading when the float is at the surface.

The Aanderaa optode (model 4330) was calibrated in the laboratory at atmospheric pressure across 9 oxygen saturations (0-115%) and 5 temperatures (1-21°C). The calibrated sensor was then exposed to a moist atmosphere of known pressure to check for differences in sensitivity in water and air. Within the errors of our measurements the sensor accuracy is identical in air and water. Details of these tests are presented in Bushinsky and Emerson (2013) and Chapter 2 of this thesis.

On deployment, air measurements of atmospheric pO_2 after each profile were compared to expected atmospheric pO_2 derived from National Center for Environmental Prediction (NCEP) reanalysis data to provide an initial calibration point (Chapter 2). The track of the O_2-Argo float and measured oxygen supersaturation (ΔO_2) as a function of depth is indicated in Figure 3.1. Winkler samples were taken from CTD casts after each of the first four profiles and measured $[O_2]$ agreed with optode oxygen calibrated to air measurements. A long-term drift of ~0.4%/yr was determined from the air measurements and used to perform a linear drift correct of the oxygen data. A 1.5 year comparison of oxygen supersaturation with the nearby OSP mooring (independently calibrated against ship-based Winkler samples) confirmed final drift-adjusted calibration (Emerson and Bushinsky 2014).

3.2.2 Upper Ocean Oxygen Mass Balance Model

The mass balance of oxygen in the mixed layer (mol O_2 m^{-2} d^{-1}) is controlled by air-water exchange, $F_{A\text{-}W}$, horizontal and vertical advection, F_H and F_W, entrainment of waters below the mixed layer, F_E, vertical mixing, $F_{\kappa z}$, and net biological oxygen production (or consumption), J_{O2} (Emerson and Stump 2010):

$$\frac{d(h[O_2])}{dt} = F_{A-W} + F_H + F_W + F_E + F_{\kappa z} \pm J_{O2} \qquad (3.1)$$

Brackets indicate concentration (mol m^{-3}) and h (m) is the depth of the mixed layer determined by the vertical density profile derived from float temperature and salinity measurements (de Boyer Montégut et al. 2004). Each of the terms on the right hand side of the above equation, except for J_{O2}, is expanded into its component terms consisting of a mass transfer coefficient, advection velocity or eddy diffusion coefficient times the oxygen concentration or concentration gradient.

The abiotic upper-ocean model compartmentalizes the upper 150 meters of the ocean into a variable height mixed layer box with 1.5 meter boxes below (Figure 3.5) in which equation 3.1 is solved for all the terms except J_{O2}. Mixed layer depth and gas solubility are determined from float measured temperature and salinity. In this way we derive an "abiotic oxygen" distribution that is stepped forward in time from the initial condition determined by the measured O_2 profile just after deployment in June. The bottom oxygen boundary at 150 m is set to the measured oxygen gradient at that depth. Calculated ANCP is not sensitive to changing the bottom boundary depth. The abiotic oxygen flux is calculated every 3 hours from each physical term ($F_{A\text{-}W}$, F_H, F_W, F_E, and $F_{\kappa z}$). Net biological oxygen production is equal to the difference between the measured (subscript B) and calculated (subscript A) terms:

$$\left.\frac{d(h[O_2])}{dt}\right|_B - \left.\frac{d(h[O_2])}{dt}\right|_A = \left(F_{A-W_B} - F_{A-W_A}\right) + \left(F_{H_B} - F_{H_A}\right) + \left(F_{W_B} - F_{W_A}\right) + \left(F_{E_B} - F_{E_A}\right) + \left(F_{\kappa z_B} - F_{\kappa z_A}\right) \pm J_{O2} \qquad (3.2)$$

where $d(h[O_2])/dt$ represents the change in oxygen concentration for each box at each time step. Each flux term is described below.

3.2.2.1 $F_{A\text{-}W}$: Air-Sea Gas Exchange

Gas exchange at the air-sea boundary of the mixed layer box is the most important term in the oxygen mass balance. Air-water exchange is modeled as the sum of diffusive interface exchange, F_S, and transport by bubbles due to breaking waves, F_B ($F_{A-W} = F_S + F_B$). Multiple air-sea gas flux parameterizations were compared to N_2 data derived from a Gas Tension Device deployed at OSP (see Emerson and Stump (2010) for description of N_2 determined from these measurements). The best fit to the N_2 data was derived using the model of Liang et al. (2013), which explicitly separates diffusive gas exchange, large bubbles that exchange with the water, and small bubbles that collapse and inject all of their gas into the water (Figure 3.2). The diffusive component is the product of a mass transfer coefficient (k) times the surface concentration difference from saturation ($F_S = k([C] - [C]_S)$) where k is a function of wind speed and Schmidt number. Transport by bubbles ($F_B = f(U_{10}, \Delta_P)$) is divided into small bubbles, which are purely a function of wind speed (U_{10}), and large bubbles, which get driven deeper at higher wind speeds, increasing the effective gas solubility through increased hydrostatic pressure (Δ_p, Liang et al. (2013)). Both small and large bubbles play a large role in the wintertime influx of oxygen.

3.2.2.2 F_H: Horizontal Advection

Horizontal advection is calculated for the mixed layer box using World Ocean Atlas climatological gas saturation [*Kalnay et al.* 1996; *Garcia et al.* 2010] and NCEP reanalysis surface currents. Saturation differences between the float location and source waters determined by current speed are used to calculate oxygen flux. Because climatological data includes biological effects, horizontal advection fluxes are used in the abiotic model to determine gas evolution but not when determining the difference between abiotic and biotic fluxes. This is an approximation, but the magnitude of the horizontal advective flux is small and not a significant contributor to ANCP.

3.2.2.3 F_W: Vertical Advection

To calculate the vertical advective flux, Ekman pumping (suction) velocities were calculated from Advanced Scatterometer derived wind stress fields (Bentamy et al. 2008). The flux of oxygen due to Ekman pumping was calculated in the direction of the flow by multiplying the velocity times the concentration difference between two adjoining boxes.

3.2.2.4 F_E: Entrainment

Entrainment is the rate of deepening of the mixed layer times the vertical gradient in gas concentration. This redistributes gas between the mixed layer and the water below, but results in no net gas flux once integrated to the deepest depth of the seasonal mixed layer.

3.2.2.5 $F_{\kappa z}$: Diapycnal Eddy Diffusion

The diapycnal eddy diffusion flux between the top and bottom of each box is calculated as a function of the diapycnal diffusivity coefficient (κ_z) times the concentration gradient between boxes. Diffusivity at the base of the mixed layer, defined as the 20 meter depth interval below the mixed layer depth, calculated from heat and salt balances derived from a surface mooring, seaglider, and profiling floats at OSP (Cronin et al., submitted, 2015) indicates a seasonal cycle in κ_z with a maximum in April and a minimum in October. We used a seasonally varying κ_z that fell in between the heat and salt derived κ_z climatologies presented in (Cronin et al., submitted, 2015) (Figure 3.3). κ_z decreases with depth from the base of the mixed layer to background values of 10^{-5} m^{-2} s^{-1} (Whalen et al. 2012) using a 1/e scaling observed by Sun et al. (2013) from microstructure measurements (example decay profile, Figure 3.4). The model was run with both a uniform κ_z throughout the water column and the seasonally varying, enhanced κ_z at the boundary between the mixed layer and the box below.

At every time step, each flux in equation 3.2 is calculated and new oxygen concentration and saturation are determined for each box. For comparison with model output, float data are binned into two-week averages and interpolated to the model time and depth resolution. In addition to the flux calculations, the float measured [O_2] (Figure 3.6A) was compared to modeled [O_2] (Figure 3.6B) and evaluated at each time step to determine $d(h[O_2])/dt$ (left side of equation 3.2). This represents the difference in oxygen storage between the measured data and model output (Figure 3.6C). J_{O2} is integrated over the depth of the seasonal mixed layer (115m) and over one annual cycle (June 2012 – June 2013). This approach differs from previous mass balance models at OSP because the abiotic model is run out a full year, including the winter months where supersaturations are close to zero.

3.2.3 Error Analysis

Monte Carlo error analyses were run for the most important flux contributors to the oxygen balance, both individually and together. Each parameter was varied according to an input error that represents ± 1 SD of the modeled uncertainty (Table 3.1). 200 iterations were performed for each individual flux and 1500 iterations for all errors simultaneously. The largest source of error in this study is uncertainty in the air-sea gas flux. In Wanninkhof (2014), the total error in the air-sea gas flux is estimated as approximately ± 20%. Liang et al. (2013) does not give an error estimate, but we assume that each component of $F_{A\text{-}W}$ (diffusive exchange, large bubbles, and small bubbles) contains a portion of the total error. We assigned a ± 15% error to each component of $F_{A\text{-}W}$; this assumes the errors are uncorrelated, which is unlikely but is a reasonable first estimate. The square root of the mean of the squared errors yields a total error of ± 26%, which gives a slightly more conservative estimate than Wanninkhof (2014).

Optode oxygen measurements in air allow calculation of the pO_2 difference between air and water (ΔpO_2). ΔpO_2 drives the air-sea flux of oxygen and because the same sensor is measuring both water and air, ΔpO_2 is independent of the optode calibration. Therefore, error in the oxygen measurements is due to our ability to measure ΔpO_2. Uncertainty in the air measurements is approximately ±0.1%.

The final significant source of error is the background diapycnal diffusivity coefficient. Error in the background κ_z (10^{-5} m^2 s^{-1}) is reported in Ledwell et al. (1993) as ± 20%. However, a wintertime κ_z estimate of 1.5×10^{-5} m^2 s^{-1} is reported as well. We chose an error of ± 50% for the background κ_z in the model. Error in mixed layer κ_z was taken from Cronin et al. (submitted, 2015), which indicated a confidence bound for both heat and salt balance derived κ_z climatologies of approximately the same order of magnitude as the derived diffusivity coefficients. We therefore chose an error of ±100% for the mixed layer κ_z.

3.3 Results and Discussion

3.3.1 ANCP Calculated from Float Data and Gas Model

The main feature in float measured ΔO_2 (Figure 3.1) is the strong supersaturation in and immediately below the mixed layer in summer (the surface depth interval indicated by the thick line in Figure 3.1), which gives way to near and slightly undersaturated water in the winter. Supersaturations vary from several percent above atmospheric equilibrium (positive values) in summer to less than one percent undersaturated in winter.

Measured oxygen (Figure 3.6A) and modeled abiotic oxygen (Figure 3.6B) are compared to determine the difference in oxygen concentration throughout the water column (Figure 3.6C). The difference represents the biologically produced oxygen stored in the water column, which, together with the difference in fluxes, represents the net biological oxygen production. Summertime production values (Apr. – Sept. only), which are most comparable to previous studies, yield ANCP of 2.0 ± 0.5 mol O_2 m^{-2} yr^{-1} (1.4 ± 0.4 mol C m^{-2} yr^{-1}, $\Delta O{:}C=1.45$) by assuming no net production in winter (Oct. – Mar.). Estimates of ANCP based on the full year of data are lower, with a total of 1.0 ± 0.7 mol O_2 m^{-2} yr^{-1} (0.7 ± 0.5 mol C m^{-2} yr^{-1}), with wintertime respiration offsetting about half of the summer production.

The importance of the different terms in the mass balance can be evaluated by successive estimates of ANCP using increasingly more realistic approaches to the calculation (Table 3.2). The simplest approach, and one that is unavoidable if one is dealing with a time series of surface-ocean-only oxygen measurements (Quay et al. 2012; Juranek et al. 2012), is to assume that over the annual cycle there is no net time rate of change and that mixing and advection are unimportant, i.e., the first and last terms on the right hand side of equation 3.1 must be equal. Using a gas exchange parameterization that does not explicitly include bubble processes (Wanninkhof 2014) yields an inferred ANCP of 3.1 mol O_2 m^{-2} yr^{-1} (2.1 mol C m^{-2} yr^{-1}, row 1 of Table 3.2). Increasing the complexity of the calculation by including the gas exchange model of Liang et al. (2013), which incorporates explicit bubble fluxes, yields an ANCP of 0.2 mol O_2 m^{-2} yr^{-1} (0.1 mol C m^{-2} yr^{-1}). Both the models with and without bubbles result in similar outgassing of oxygen during the supersaturated summer months, but the model without bubbles predicts far less gas input from the atmosphere during winter when high winds create bubbles that insert gases into the water. A greater flux of oxygen from the atmosphere due to bubbles results in a lower inferred biological production in order to match the observations.

Finally, including diapycnal eddy diffusion impacts the entire water column by removing oxygen according to the gradient at the depth of the winter mixed layer (~115 m). The oxygen gradient at this depth is negative (decreasing oxygen with increasing depth), so diapycnal eddy diffusivity removes oxygen from the upper water column. With no diapycnal eddy diffusion, influx from bubbles would nearly balance efflux from air-sea surface according to the previous discussion (ANCP = 0.1 mol C m^{-2} yr^{-1}). Employing a background value of the eddy diffusion coefficient ($\kappa_z = 10^{-5}$ m^2 s^{-1}) increases this value by 0.3 mol C m^{-2} yr^{-1} and using diapycnal eddy diffusion at the base of the mixed layer determined from heat flux (Cronin et al., submitted, 2015) (Figure 3) increases it to a total of 0.7 mol C m^{-2} yr^{-1} (Table 3.2, Figure 3.7B).

The roughly equal importance of background κ_z and mixed layer κ_z is due to the seasonal cycle of the mixed layer depth. For most of the year the mixed layer is well above its deepest depth (~115 m), so the background κ_z is responsible for the slow diffusion of oxygen out of the upper ocean. κ_z at the base of the mixed layer is most important during the winter months, when the mixed layer comes into contact with deep, low-oxygen waters. Addition of horizontal and vertical advective fluxes to the model reduces the final calculated ANCP by a small but insignificant amount.

In summary, the most significant flux terms in the abiotic oxygen model are surface air-sea gas exchange, injection by bubbles and the flux from diapycnal diffusion (Figure 3.7A). On an annual basis, diffusive gas exchange and diapycnal diffusion act to remove oxygen from the water column and are balanced by bubble fluxes and net biological production injecting oxygen into the upper ocean. Diffusive gas exchange exhibits a seasonal cycle that follows the mixed layer oxygen supersaturation. During summer months, high surface supersaturations and low wind speeds cause a strong flux out of the water column (negative values in Fig. 3.7A) before winter undersaturation results in diffusion of oxygen back into the mixed layer. During the winter, with no bubble injection, the small diffusive flux of oxygen into the surface ocean would result in little inferred change in net biological production. With bubble injection, the large physical flux of oxygen into the water requires net respiration to maintain that same slightly undersaturated water.

The small error for the oxygen sensor could not be achieved without in situ atmospheric calibration. The advantage of the in situ calibration of optodes to atmospheric oxygen is that it is possible to directly measure the air-water difference in oxygen, which determines the flux. Uncertainty in the initial oxygen calibration or in the atmospheric pressure estimate does not change the gas flux. As long as the same pressure product is used for both calibration and subsequent mass balance analysis, uncertainty in atmospheric pressure adds no error to the ANCP calculation.

3.3.2 Evaluation of ANCP Relative to Prior Estimates

Emerson (2014) compiled ANCP calculations at OSP from a variety of mass balance and sediment trap studies in addition to satellite and model based estimates. Both oxygen and nitrate mass balances suggested ANCP of 2.3 ± 0.6 mol C m^{-2} yr^{-1}. These values, however, used only data from the summer months and assumed the wintertime contribution was negligible. The net wintertime oxygen loss observed in this study implies that respiration outweighs production at this time of the year, which has a significant impact on the annual carbon export.

Net heterotrophy during the winter at first seems to be in conflict with earlier sediment trap and thorium mass balance studies showing particle export throughout the year (Charette et al.

1999; Wong et al. 1999) with a total annual flux of 0.5 mol C m^{-2} yr^{-1} at 200m (Timothy et al. 2013). However, it is possible that dissolved organic carbon (DOC) production can allow both year-round particle export and wintertime net heterotrophy. If a significant fraction of the summertime production is in the form of semilabile DOC, the net heterotrophy observed in this study during the winter could be driven by the consumption of accumulated DOC even as low rates of autotrophy drive particle export. While there appear to be no studies of seasonal variability in surface DOC for the North Pacific subarctic ocean, the magnitude of seasonal change elsewhere has been reported as 5-30 μM (Hansell and Carlson 2001). We observe a decrease of ~1 mol O_2 m^{-2} (~0.7 mol C m^{-2}) from the summertime max to the wintertime low (Figure 3.7B). A decrease of this magnitude would require the respiration of approximately 9 μM DOC (assuming an average mixed layer depth of ~75 m during this time), which falls within the range of observed seasonal variability in epipelagic DOC.

Using an ecosystem model coupled to satellite derived chlorophyll and carbon, Siegel et al. (2014) arrive at a particulate organic carbon flux of approximately 2.5 mol C m^{-2} yr^{-1} for the northeastern subarctic gyre. This value agrees with the oxygen and nitrate mass balances compiled in Emerson (2014), but again is higher than the annual estimate from this study. Summertime rates of NCP are similar between our study and the satellite-predicted fluxes, thus differences in the winter NCP rates must account for the lower ANCP determined here. Sonnerup et al. (2013) used CFC-derived transit times and AOU along a North Pacific transect to calculate an organic carbon export of ~0.5 ± 0.2 mol C m^{-2} yr^{-1} at 50°N. This technique should integrate seasonal cycles in net production and is very close to the value we predict for the subarctic Pacific.

3.4 Conclusions

We used accurate, year-long measurements of oxygen from a profiling float achieved by in situ calibration and an upper ocean model to determine annual net community production and the magnitude of the biological pump in the subarctic Pacific Ocean. Because we were able to determine accurate, frequent year-round flux estimates, it has been possible to show that there is net respiration during darker, less productive times of year. Interpretation of surface ocean oxygen measurements in terms of annual net community production requires an accurate model for bubble processes in regions where there are high winds in the wintertime. Furthermore, diapycnal diffusion of low oxygen waters into the upper ocean is a significant term in the upper ocean oxygen mass balance.

Our results agree with independent latitudinal trends of the biological pump determined from apparent oxygen utilization rates evaluated with tracer age in the upper thermocline (Sonnerup et al. 2013), but are at odds with predictions from satellites and ocean global circulation models. The number and geographic distribution of experimentally-determined measurements of the biological pump will have to be increased to accurately inform satellite and global circulation models of this essential biogeochemical boundary condition. This could be achieved by year-long upper-ocean oxygen mass balances determined from in situ measurements on remote platforms.

3.5 Tables

Table 3.1. Monte Carlo error analysis for the ANCP model.

Parameter	Error (%)	ANCP (mol C m^{-2} yr^{-1})
Oxygen	0.1	0.7 ± 0.2
F_{a-w}	~26	0.7 ± 0.3
κ_{ML}	100	0.7 ± 0.1
κ_{Deep}	50	0.7 ± 0.2
P_{ATM}	0.5	0.7 ± 0.01
All	**-**	**0.7** ± 0.5

Each input term was varied with the standard deviation of the error matching the % listed above. Individual parameter Monte Carlos were run 200 times and total, with all parameters, was run through 1500 iterations. We used a constant value ($\Delta O_2 : \Delta OC = 1.45$) to convert net biological oxygen production values into ANCP values.

Table 3.2. NCP calculated with increasing model complexity.

Mechanism	Summer (mol C m^{-2})	Annual (mol C m^{-2} yr^{-1})
a. $F_{a\text{-}w}$, no bubbles	-[*]	2.1
b. $F_{a\text{-}w}$, w. bubbles	-[*]	0.1
c. $F_{a\text{-}w}$, bubbles + diap. mixing		
$\kappa_z = 10^{-5}$ m^2 s^{-1}	1.5 ± 0.4	0.4 ± 0.4
κ_z based on heat/salt flux	1.3[†] ± 0.4	0.7 ± 0.5

Calculating ANCP from O_2 data using progressively more complete terms in the abiotic model to illustrate the importance of different physical processes in evaluating the net biological O_2 production. (a) Considering only the air-sea flux calculated from float data and a gas exchange parameterization that does not explicitly include bubbles (Wanninkhof 2014). (b) The same flux calculation using a gas exchange parameterization that includes bubbles (Liang et al. 2013). (c) Using the abiotic model described by equation 3.2 and two κ_z configurations: the first with a constant water column κ_z and the second with a κ_z that is enhanced at the base of the mixed layer and decays to the background κ_z of 10^{-5} m^2 s^{-1} 20 m below.

[*] (a) and (b) are calculated using data only and assume no net change in oxygen over an annual cycle. Summer values are not shown because these would represent an oxygen flux due to both biology and changes in solubility.

[†] For these runs horizontal and vertical advective fluxes were not included. Addition of the advective fluxes slightly increases summer production to 1.4 ± 0.4 mol C m^{-2} yr^{-1}.

3.6 Figures

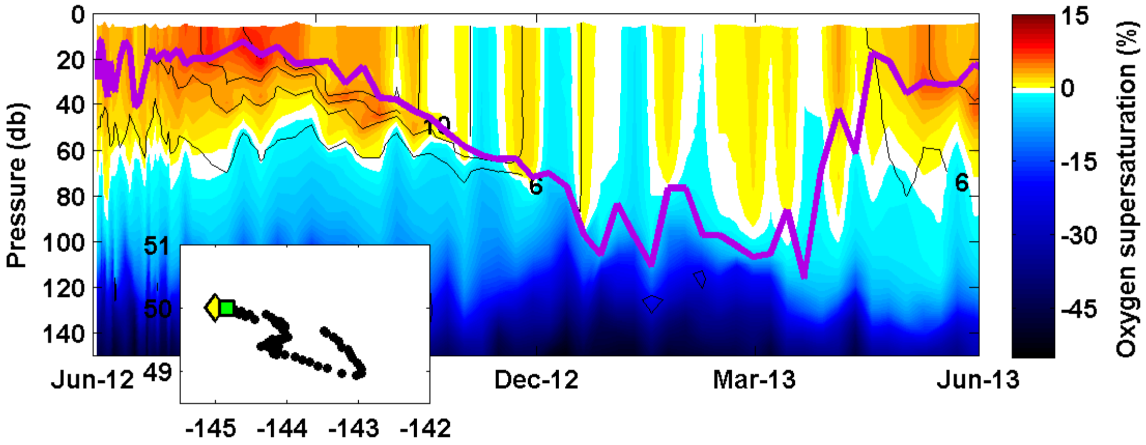

Figure 3.1. Oxygen supersaturation, ΔO_2 (%) = ($[O_2]-[O_2^s]$) / $[O_2^s]$) X 100 as a function of depth and time in the Northeastern Subarctic Pacific. The heavy line represents the mixed layer depth using a 0.2 °C potential temperature change from 10 m (de Boyer Montégut et al. 2004). Lighter lines are constant temperature contours, and colors are ΔO_2. The float track for the oxygen data presented in the inset shows the initial deployment (green square) and the position of the OSP mooring (yellow diamond).

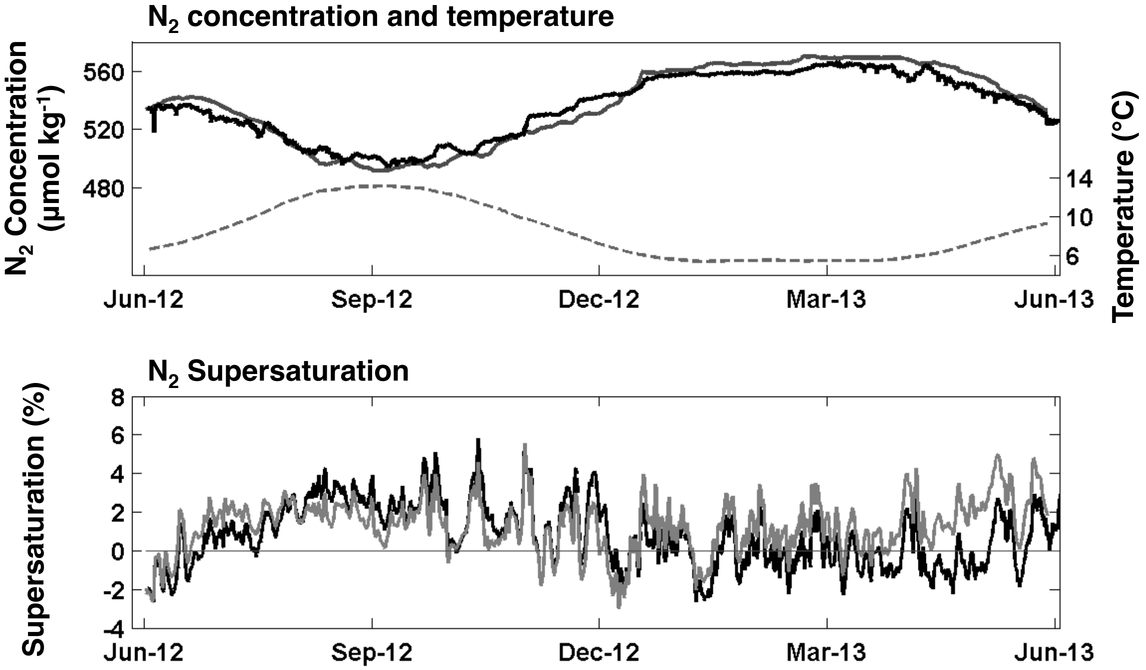

Figure 3.2. N$_2$ concentration and Ocean Station Papa temperature (top) and N$_2$ saturation (bottom). Data (black lines) are calculated from total gas pressure measured by a Gas Tension Device. Temperature (dashed gray line) is measured from a SeaBird Electronics 16 Plus conductivity, temperature, and depth sensor. Modeled data (gray lines) are from the 1-dimensional abiotic gas model using the Liang et al. 2013 gas parameterization.

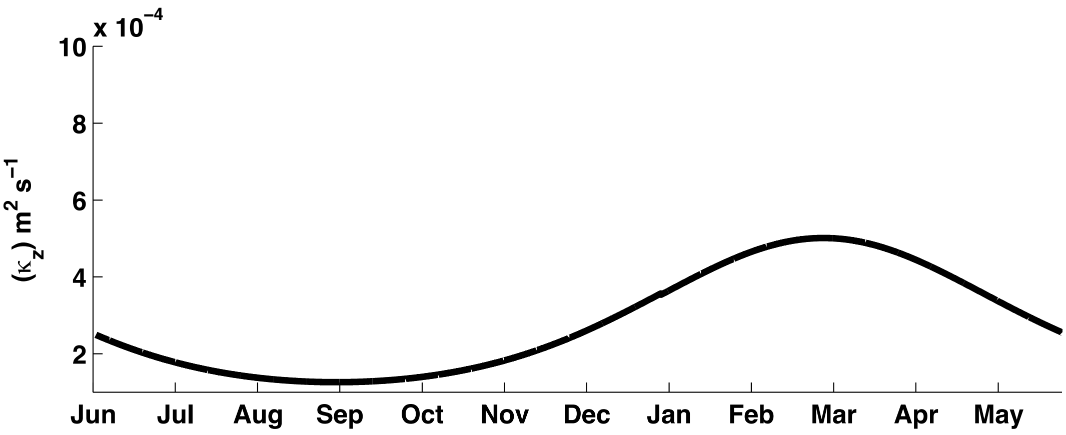

Figure 3.3. Seasonal variation in the diapycnal eddy diffusion coefficient (κ_z) at the base of the mixed layer used in the abiotic model. The magnitude, amplitude, and seasonal cycle were chosen to best fit the κ_z climatology from heat and salt budgets calculated at OSP (Cronin et al., submitted, 2015).

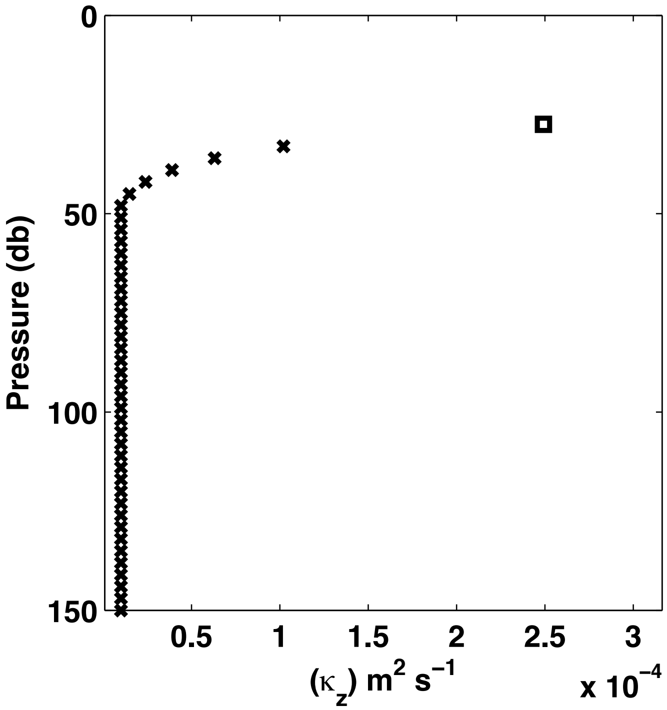

Figure 3.4. Example of the diapycnal diffusivity coefficient (κ_z) profile with depth from June 2012. κ_z for diffusion between the mixed layer and the box below (square) is determined by the seasonal cycle shown in Fig. 3.3. The diffusivity coefficients for deeper boxes (x's) follow an exponential decay over 20 m (Sun et al. 2013) to the background value of $\kappa_z = 10^{-5}$ m^2 s^{-1}.

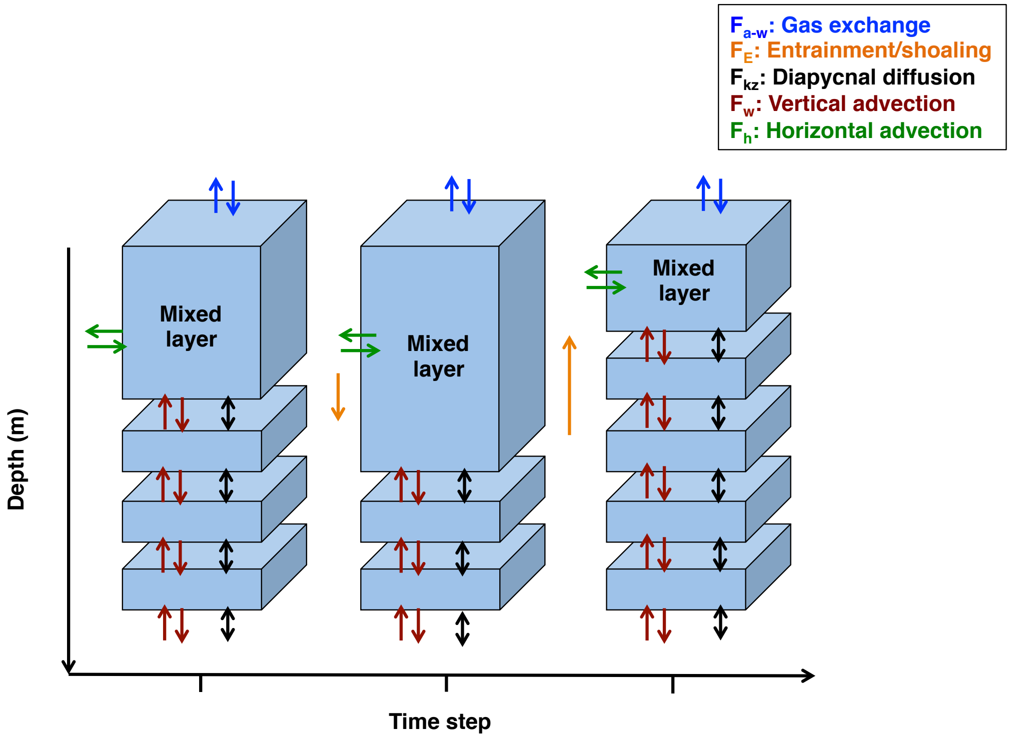

Figure 3.5. Schematic showing three time steps with the mixed layer deepening and shoaling between time steps. F_{a-w} (air-water gas exchange, blue arrows) and F_h (horizontal advection, green arrows) are calculated for the mixed layer only. F_E (entrainment/shoaling, orange arrows) redistributes oxygen between boxes but results in no column-integrated change in the oxygen inventory. F_w (vertical advection, red arrows), moves oxygen according to uniform Ekman velocities calculated from satellite derived wind stress and the oxygen difference between adjacent boxes. F_{kz} moves oxygen between all boxes according to the diapycnal eddy diffusivity coefficient and the oxygen gradient.

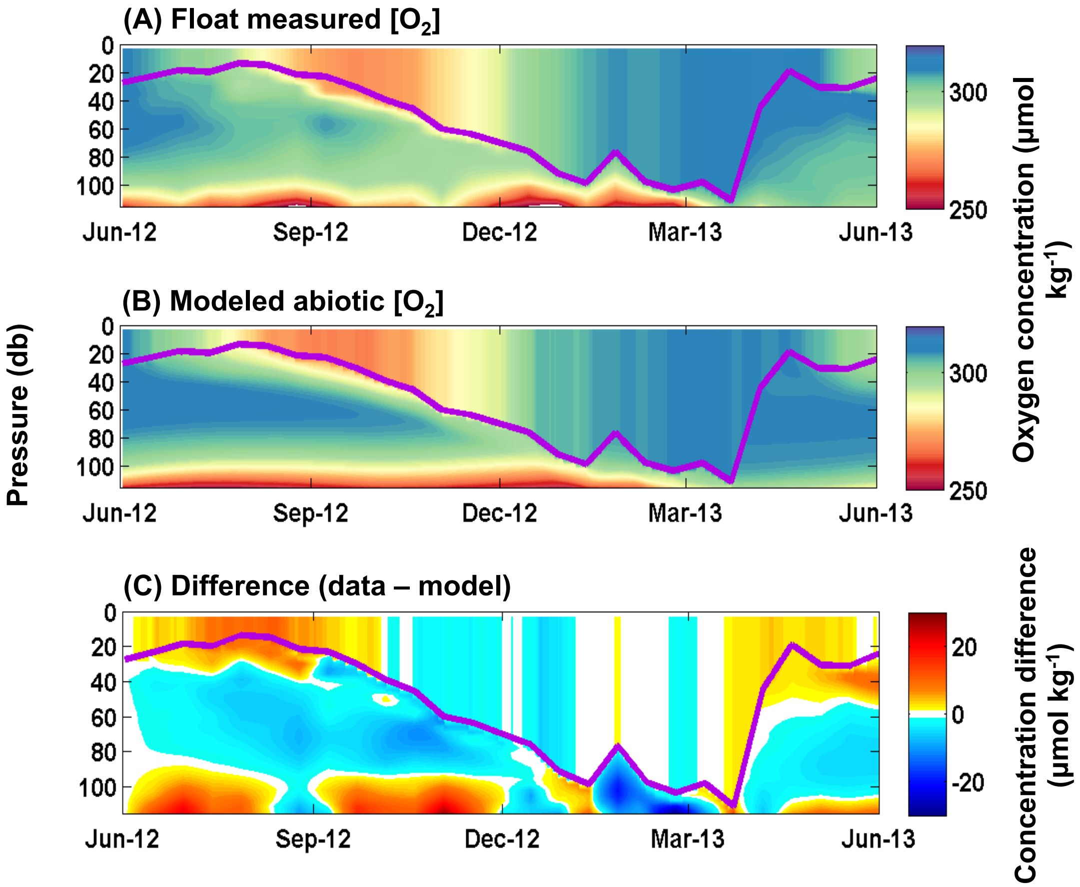

Figure 3.6. Float measured [O_2] (A), model-produced abiotic [O_2] (B), and the difference (C) as a function of pressure and time in the upper ocean for June 2012 – June 2013. Changes in [O_2] throughout the year are largely controlled by solubility, with differences between the measured and modeled data showing areas of biological production and respiration. The difference (C) between the measured and modeled [O_2] is due to biological processes. Areas of high and low [O_2] around 100-110m are the result of heaving isopycnals in the data that are not reproduced in the model. While this can result in temporary mismatches in calculated stored biological O_2, it does not have a significant impact on the total ANCP.

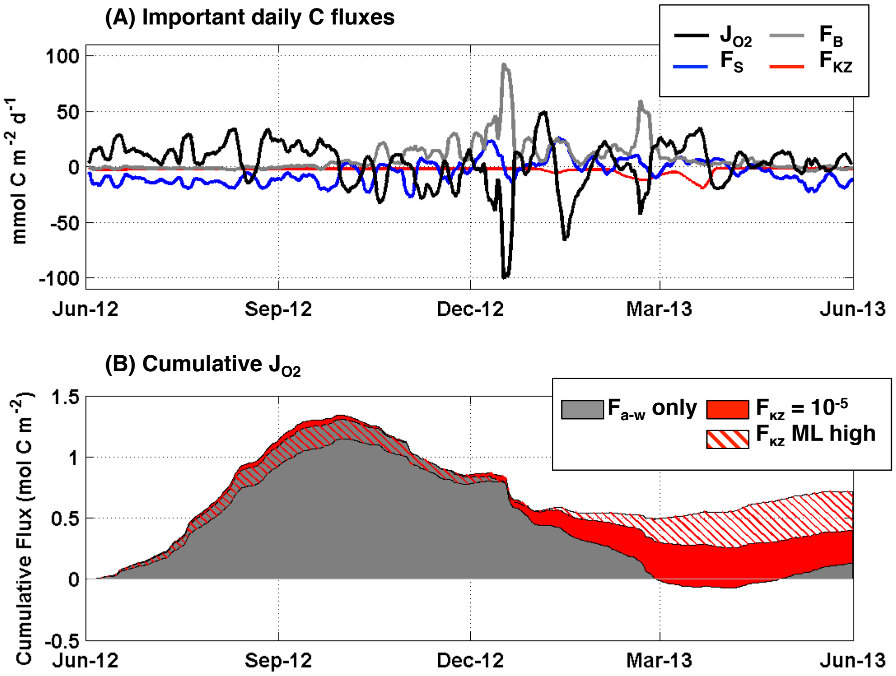

Figure 3.7. Daily and cumulative fluxes of carbon used to calculate upper ocean ANCP. (A) Modeled daily abiotic oxygen fluxes in units of carbon showing the most important terms and the calculated biological production, J_{O2} (in units of C). Positive values represent addition of oxygen (organic carbon) to the ocean. For clarity, fluxes are smoothed using a 3 week running mean. Air-sea surface gas exchange (F_S) and bubble (F_B) fluxes are the constituent components of $F_{a\text{-}w.}$ (B) Cumulative biological production (J_{O2}) for three model runs. Increasing values mean biological oxygen is being produced in the upper ocean; flat indicates no change with time; and a downward trend marks a decrease in the flux. Values at the very end represent the annual magnitude of J_{O2} for each model run.

Chapter 4

Seasonal oxygen supersaturation and air-sea fluxes from profiling floats in the Pacific

Abstract

The Pacific Ocean is a heterogeneous basin that includes regions of strong CO_2 fluxes to and from the atmosphere. The Kuroshio Extension (KE) is a current associated with the largest CO_2 flux in to the Pacific Ocean, which extends across the Pacific basin between the subarctic and subtropical regions. The relative importance of the biological and physical processes controlling this sink are uncertain. Because oxygen is stoichiometrically linked to changes in dissolved inorganic carbon due to photosynthesis and respiration and subject to many of the same physical drivers as CO_2 flux, in situ oxygen measurements may help determine the processes driving this large CO_2 flux.

In this study, we used Argo profiling floats with modified oxygen sensors to estimate oxygen fluxes in several areas of the Pacific. In situ air calibrations of these sensors allowed us to accurately measure air-sea oxygen differences, which largely control the flux of oxygen to and from the atmosphere. In this way, we determine air-sea oxygen fluxes from profiling floats, which previously did not measure oxygen accurately enough to make these calculations. Argo floats park at 1000m depth in between profiles and do not act as strictly Lagrangian drifters in the upper ocean. In areas such as the Kuroshio Extension, this can create difficulties in determining the seasonal cycle of supersaturation and oxygen flux from individual floats. To characterize different areas around the Kuroshio Extension, we separated oxygen measurements from different floats into 3 regions based on geographical position and temperature-salinity relationships: North KE, Central KE, and South KE. We then used these regions and floats in the Alaska Gyre and subtropical South Pacific gyre to develop seasonal climatologies of oxygen supersaturation and air-sea flux.

Mean annual air-sea oxygen fluxes (positive fluxes represent addition of oxygen to the ocean) were calculated for the Alaska Gyre of -0.3 mol m^{-2} yr^{-1} (2012-2015), for the northern Kuroshio Extension, central Kuroshio Extension, and southern Kuroshio Extension (2013-2015) of 6.8, 10.5, and 0.5 mol m^{-2} yr^{-1}, respectively, and for the south subtropical Pacific near Samoa (2014-2015) of 0.6 mol m^{-2} yr^{-1}. Air-sea gas exchange was calculated using a parameterization that explicitly calculates diffusive exchange and bubble injection. The air-sea flux due to bubbles was greater than 50% of the total flux for winter months and essential for determining the magnitude and, in some cases, direction of the cumulative mean annual flux. Increases in solubility due to wintertime cooling coupled with a deepening mixed layer were responsible for 30-50% of the mean annual oxygen flux in the Kuroshio Extension. The magnitude of the air-sea fluxes in the north and central KE regions makes it unlikely that we will be able to determine a meaningful annual biological flux from oxygen measurements. However, we can use the seasonal cycles in regional fluxes to determine the magnitude of summertime biological production, and the contribution of subduction and water mass formation to the net annual flux in the Kuroshio Extension and annual net community production in the Alaska Gyre and south subtropical Pacific.

4.1 Introduction

Over an annual cycle, the largest CO_2 flux into the northern Pacific ocean is found in the western Pacific, in and around the Kuroshio current and its extension into the North Pacific Transition Zone (NPTZ) (Takahashi et al. 2002, 2009) (Figure 4.1). The Kuroshio brings warm water north, where it cools and mixes with nutrient rich waters, simultaneously increasing solubility and stimulating biological production. The Kuroshio Extension (KE) continues across the Pacific, dividing the subarctic Western Subarctic Gyre (WSG) and Alaska Gyre (AG) in the northwest and northeast, respectively, from the North Pacific subtropical gyre to the south. The location of the Kuroshio Extension and its meanders varies seasonally (Jayne et al. 2009), as does the NPTZ and its associated chlorophyll front (Bograd et al. 2004; Ayers and Lozier 2010). The WSG and AG are high nutrient, low chlorophyll (HNLC) regions that show strong seasonal cycles in production (Harrison et al. 2004). In contrast, the subtropical gyres north and south of the equator are oligotrophic regions with much smaller seasonal cycles in temperature and production (Nicholson et al. 2008).

The uptake of CO_2 is driven by solubility, biology, and mixing, with the differentiation of the impact of each process a subject of on-going research (Takahashi et al. 2002; Chierici et al. 2006; Ayers and Lozier 2012). Strong temporal variability in the physical drivers of gas flux, temperature and winds, plus changes in biological parameters such as light and nutrient availability, produce large seasonal variations in the strength of the CO_2 flux. Spatial heterogeneity of water mass properties creates distinct ecological regions. Many studies have worked to characterize the bounds of these regions and determine their biogeochemical characteristics and resulting ecological properties. Longhurst et al. (1995) divided the Pacific north of the NPTZ into ecological domains based on nutrient supply, further subdividing these domains into biogeochemical provinces defined by physical parameters.

Determining the processes driving CO_2 exchange in the Pacific Ocean is difficult given the spatial and temporal scales involved. Takahashi et al. (2002) determined the magnitude of CO_2 flux caused by seasonal temperature-induced solubility changes and attributed the remainder of the observed CO_2 uptake to biological export. This method assigns approximately equal responsibility for the CO_2 flux to solubility and biology, though physical terms such as mixing are included in the biological term. Ayers and Lozier (2012) modeled physical controls on the NPTZ and found that biology and geostrophic advection of dissolved inorganic carbon (DIC) were of approximately equal importance to the total CO_2 flux. However, because the flow of the Kuroshio from south to north cools the water, driving an influx of CO_2, this mechanism is still fundamentally a solubility driven pump, though different than the seasonal cycle in temperature at a fixed physical location.

The air-sea oxygen flux is driven in the same direction by solubility changes as CO_2, but during biological production oxygen is produced while DIC is consumed. Oxygen measurements can be used to determine biological carbon export (Emerson et al. 2008; Emerson and Stump 2010). The amount of oxygen produced during photosynthesis is in a stoichiometric ratio to the amount of organic carbon fixed. Over an annual cycle, and assuming no net physical inputs, any oxygen produced during photosynthesis but not consumed by respiration is related to the amount of organic carbon fixed that sank out of the upper ocean as part of the biological carbon pump (Volk and Hoffert 1985). Net oxygen production associated with CO_2 drawdown provides evidence of biological production at least partially driving the air-sea CO_2 flux. Alternatively, an observed air-sea O_2 flux in the same direction as the CO_2 flux implies solubility changes are driving the flux.

The recent deployment of Argo profiling floats equipped with oxygen sensors has greatly expanded the availability of in situ oxygen measurements over annual cycles. Oxygen produced during photosynthesis will increase the saturation state of the surface ocean, as will increases in sea surface temperature, resulting in a flux from the ocean to the atmosphere. In order to accurately measure the net production or consumption of oxygen from surface measurements, it is essential to accurately estimate the air-sea flux of oxygen. The air-sea oxygen flux is primarily a function of the concentration difference from saturation. Because this difference can often be as small as a percent, accuracy in oxygen measurements is paramount for an accurate determination of the air-sea flux.

In this study we use modified Argo floats capable of in situ atmospheric measurements to accurately estimate the annual cycles of oxygen supersaturation in the Alaska Gyre, the Kuroshio Extension, and in the subtropical South Pacific. We then use these measurements to determine mean air-sea fluxes for these regions.

4.2 Methods

4.2.1 Special Oxygen Sensor Argo Float Deployments

Argo floats used in this study (Special Oxygen Sensor (SOS)-Argo) are modified APEX floats developed at the University of Washington designed to allow in situ atmospheric calibration of the oxygen optodes (Emerson and Bushinsky 2014; Bushinsky and Emerson 2015; Bushinsky et al. 2015). The optodes (Aanderaa model 4330) are raised on stalks to measure atmospheric pO_2 after surfacing with minimal interference from surface waves and splashing. Oxygen optodes are known to drift significantly at STP (D'Asaro and McNeil 2013; Bushinsky and Emerson 2013; Takeshita et al. 2013; Bittig and Körtzinger 2015; Johnson et al. 2015) and recent evidence indicates a the potential for a smaller, but still significant drift after deployment (Bushinsky et al. 2015). The atmospheric measurements after each profile provide a long-term calibration to correct for drift, both prior to deployment and during float operation. Floats profile every 10 days, parking at 1000m depth in between measuring oxygen, temperature, salinity, and pressure from 2000m to the surface.

Floats were deployed at 3 locations: in the Alaska Gyre at Ocean Station Papa (OSP, 1 float, June 2012), in the Kuroshio Extension (8 floats, March 2013), and in the equatorial Pacific near Samoa (1 float, January 2014) (Figure 4.2, Table 4.1). The OSP and Samoa floats stayed relatively stationary, moving less than 300 km from their initial deployment locations. KE floats have drifted in a much larger area, though staying near the KE region. Floats are named according to their deployment location (Table 4.1).

4.2.2 Calibration of oxygen sensors

The SOS-Argo oxygen optodes were calibrated using in situ atmospheric measurements. After each profile, 30 air samples were taken over a one-hour period. These atmospheric measurements were compared to expected atmospheric pO_2 based on reanalysis pressure and humidity data from the National Centers for Environmental Prediction (NCEP). Initial calibration and subsequent drift corrections were based on a linear fit to the offset between measured and expected atmospheric pO_2 (see Bushinsky et al. (2015) for more details). Three of the optodes had measurable drift of -0.5% yr^{-1}, 6 optodes drifted at slower rates, including 2 that indicated positive drift, and 5 showed no measurable drift.

4.2.3 Air-sea gas exchange flux

The air-sea exchange of oxygen is comprised of two pathways, diffusive gas exchange and bubble injection, both of which are governed by the degree of oxygen supersaturation and wind speed. We chose a gas flux parameterization (Liang et al. 2013) that explicitly includes two types of bubbles, large and small, to accurately estimate the air-sea oxygen flux. The model parameterizations presented below were derived from a 3-dimensional numerical bubble model developed to determine the effect of bubbles on mixed layer circulation. This model was able to reproduce measured noble gas ratios and in situ seasonal N_2 measurements made on a surface mooring at Ocean Station Papa (Bushinsky and Emerson 2015; Emerson and Bushinsky 2015). The total air-sea oxygen flux ($F_{A\text{-}W}$) is the sum of the air-sea interface exchange (F_S), small, completely collapsing bubbles (F_C), and large, partially collapsing bubbles (F_P):

$$F_{A-W} = F_S + F_C + F_P \qquad \text{mol m}^{-2}\ \text{d}^{-1}, \tag{4.1}$$

F_S is a function of oxygen concentration ($[O_2]$, μmol kg^{-1}) difference from saturation times a air-sea interface mass transfer coefficient ($k_{S,O2}$):

$$F_S = k_{S,O2}\left(\left[O_{2,sat}\right] - [O_2]\right)\frac{\rho_w}{10^6} \qquad \text{mol m}^{-2}\ \text{d}^{-1}, \tag{4.2}$$

Liang et al. (2013) uses the NOAA_COARE linear relationship between k_S and the air-side friction velocity (U_a^*) to evaluate the wind speed (U_{10}, m s^{-1}) and Schmidt number (S_{O2}) dependent mass transfer coefficient:

$$k_{S,O2} = 1.3\times10^{-4} U_a^* \left(\frac{S_{O2}}{660}\right)^{-0.5} \quad \text{m s}^{-1}, \tag{4.3}$$

where

$$U_a^* = {C_d}^{0.5} U_{10} \qquad \text{m s}^{-1}, \tag{4.4}$$

and 660 is the Schmidt number for CO_2 in seawater at 20°C. The air-side friction velocity, U_a^*, is the product of a dimensionless drag coefficient and wind speed ($C_d = 0.0012$ below 11 m s^{-1}, ($0.49+0.065 \times U_{10}$) x 10^{-3} between 11 and 20 m s^{-1}, and 0.0018 above 20 m s^{-1}). Note that a positive flux means that oxygen is going into the ocean and a negative flux represents gas lost to the atmosphere.

Small bubbles that completely collapse add gas to the water as a function of wind speed but are independent of saturation state:

$$F_C = 5.56(U_w^*)^{3.86} X_{O2} \quad \text{mol m}^{-2}\,\text{s}^{-1} \tag{4.5}$$

where X_{O2} is the mole fraction of oxygen in the atmosphere. U_w^* is the water-side friction velocity calculated using U_a^* and the densities of air (ρ_a) and water (ρ_w):

$$U_w^* = \left(\frac{\rho_a}{\rho_w}\right)^{0.5} U_a^* \qquad \text{m s}^{-1} \tag{4.6}$$

Large bubbles that are pushed into the ocean and rise back to the surface without collapsing and exchange gas according to the saturation state of the surrounding water:

$$F_P = 5.5\,(U_w^*)^{2.76} \left(\frac{S_{O2}}{660}\right)^{-2/3} \left([1+\Delta_P]\left[O_{2,sat}\right]\frac{\rho_w}{10^6} - [O_2]\frac{\rho_w}{10^6}\right) \text{mol m}^{-2}\,\text{s}^{-1} \tag{4.7}$$

Δ_P is the fractional increase in saturation concentration due to the higher pressures experienced by bubbles driven down to deeper depths at high wind speeds:

$$\Delta_P = 1.5244 {U_w^*}^{1.06} \tag{4.8}$$

For air-sea flux calculations, temperature, salinity, and surface oxygen concentration are determined from float measurements. Sea level pressure, used to calculate oxygen saturation state, is derived from NCEP reanalysis output. Wind speed is calculated from Advanced Scatterometer (ASCAT) wind vectors (Bentamy et al. 2008). Air-sea fluxes were calculated on a daily time step, with float measurements interpolated to match. This matches the wind speed temporal resolution used in the Liang et al. (2013) flux parameterization and prevents excessive averaging of high wind speeds that can drive strong, but potentially brief air-sea fluxes.

Emerson et al. (2008) identified uncertainty in the oxygen measurement as contributing ~50% error to estimates of net oxygen production, primarily due to the impact of uncertainty in oxygen supersaturation on the air-sea flux estimate. In addition to improving the accuracy of the oxygen sensors through air calibration, as described above, measurements of atmospheric oxygen provide a direct calculation of the partial pressure difference between air and water, the quantity that controls the air-sea flux.

Uncertainty in the NCEP atmospheric pressure would normally contribute directly to error in either atmospheric calibration of oxygen sensors or calculation of the oxygen saturation concentration for air-sea gas flux calculations. However, using the same pressure measurement for both calibration of the oxygen sensor and air-sea mass transfer coefficient results in significantly reduced error.

4.2.4 Separation of float measurements into biogeochemical provinces

To account for float movement between different ecological provinces in the KE and group float supersaturations from different profiles, floats profiles were grouped based on both latitude and longitude as well as temperature-salinity (TS) plots. Assigning float profiles to different regions based purely on geographic location (Figure 4.3A) ignores seasonal movement in water mass locations. Comparing TS of surface samples (Figure 4.3B) allows profiles and measured supersaturations to be grouped into similar water masses.

The North KE region (blue) and Central KE region (green) were separated along line 2 in Figure 4.3B, which corresponds to the boundary between the main Kuroshio Extension current and the WSG. This boundary moves north and south seasonally, which causes overlap of the profile locations in Figure 4.3A. The South KE region was divided from the Central KE region in TS space along line 1 with the addition of profiles east and south of line 4 (Figure 4.3A), which displayed a similar seasonal cycle in oxygen supersaturation to the rest of the South KE region. Finally, profiles in coastal waters with very high oxygen supersaturation (20-60%) were removed from the North KE region and not considered part of the typical seasonal cycle by filtering out measurements colder and fresher than line 3. Floats OSP (8397) and SSP (8485) are used to represent the Alaska Gyre and the south subtropical Pacific gyre, respectively. These regional criteria create distinct groupings of float surface measurements that show different seasonal cycles of supersaturation and air-sea fluxes. Float deployment locations, identifying information, and contribution to each of the KE regions are described in Table 4.1. Regional separation of measurements is used for Figures 4.6, 4.7, and 4.8. All KE floats except KE-N contributed profiles to multiple KE regions. KE-N only surfaced in the North KE region. Several floats (KE-C2, 3, 4, and 6) all surfaced in each KE region at different times in their deployments.

4.3 Results

4.3.1 Seasonal changes in O_2 supersaturation

Mixed layer oxygen supersaturations (ΔO_2), temperature, and mixed layer depth for all floats are plotted in Figure 4.4, arranged from north to south. Data is divided into April-March annual cycles for 2012-2013 (green), 2013-2014 (blue), and 2014-2015 (red). Measured ΔO_2 ranged from -10 to 53%. Mixed layer depths were calculated from float measured temperature, salinity, and pressure profiles according to de Boyer Montégut (2004) using the potential temperature threshold. All floats displayed mixed layer depths shallower than 20 m during the summers. The deepest mixed layer depth recorded was 410 m (float KE-N) during the March 2012 in the Kuroshio Extension and the shallowest wintertime mixed layer was 82 m, observed in the southern subtropical gyre from float SSP. Mixed layer depth is important to interpretation of supersaturations because it represents the volume of water that can readily exchange gas with the atmosphere. With a deep mixed layer, any given flux of oxygen to the ocean will result in a smaller change in ΔO_2, maintaining the air-sea gradient in pO_2 and resulting flux.

The two northernmost floats, OSP and KE-N, display similar seasonal cycles in ΔO_2 and temperature (Figure 4.4). Both exhibit supersaturations of several percent in the summer months (May-August), with KE-N reaching slightly higher ΔO_2. During the winter, both floats measured ΔO_2 at and slightly below saturation, with deepest mixed layer depths of ~110 (OSP) - 175 m (KE-N).

The floats deployed in the middle of the KE, floats KE-C1-6, measured a wide range in surface ΔO_2. These floats profiled in water masses with both the highest supersaturations and the most consistently undersaturated waters. Floats KE-C4 and KE-C5, both of which spent time close to the coast of Japan, measured supersaturations in excess 20% during April-May 2014. This period of supersaturation is associated with water over 10°C colder than measured in the previous year, indicating the floats were in a different water mass during that time. A little further south, float KE-C3 recorded undersaturations of -2 to -5% for both years of deployment, while the winter mixed layer depth varied between 100-300 m. Overall, winter mixed layer depths for this group of floats were deep, with all floats except KE-C1 being in excess of 200m.

The southernmost float deployed in the KE group, KE-S, shows more similarities in oxygen time series the float deployed near Samoa, SSP, than to the rest of the KE floats. ΔO_2 measured by both floats reach only a few percent supersaturated during the summer months (May – Oct for KE-S, Nov – Mar for SSP, in the southern hemisphere) and wintertime mixed layers deepened to ~80m with ΔO_2 is slightly below saturation. The seasonal range in temperature was much larger for KE-S (9.3°C) than SSP (2.4°C).

4.3.2 Air-sea oxygen fluxes by float

Air-sea oxygen fluxes were determined at a daily resolution as described in section 4.2.3. Water saturation state and wind speed drive gas flux, with summertime supersaturation due to warming and biology causing an efflux of oxygen and wintertime undersaturation from cooling, mixing, and biological processes an influx of oxygen during a typical annual cycle. In Figure 4.5, air sea fluxes calculated from each float are plotted from north to south, with monthly mean fluxes plotted in the top plot for each float and cumulative annual fluxes plotted below.

Floats OSP and KE-N show a roughly balanced seasonal cycle with summer efflux of oxygen offsetting winter influx. The largest summertime outgassing for these floats occurs from June-August, with an average daily flux of 20-30 mmol O_2 m^{-2} d^{-1} for OSP and 30-50 mmol O_2 m^{-2} d^{-1} for KE-N.

Air-sea fluxes calculated from floats positioned closer to the heart of the Kuroshio Extension (KE-C1-6) were not seasonally balanced, with a very strong influx of oxygen during the winter dominating the net flux. Relatively weak summertime outgassing was determined for most of these floats, with the exception of KE-C4 and KE-C5. Both of these floats showed several months of outgassing during April-June of the 2014-2015 season caused by the high oxygen supersaturations observed in Figure 4.4. Wintertime outgassing of 50-190 mmol O_2 m^{-2} d^{-1} resulted in cumulative annual fluxes of 10-15 mol O_2 m^{-2} yr^{-1}.

Float KE-S, south of the Kuroshio Extension measured a consistent supersaturation of 1-3% for 6 months, driving a small but steady outgassing of oxygen from May to October. A stronger, but shorter wintertime oxygen flux in to the ocean in January and February balances the summer outgassing, ending the annual cycle in a slight net influx of between 0-1 mol O_2 m^{-2} yr^{-1}. In the southern subtropical gyre, the near-saturation oxygen measured by float SSP results in a small net flux to the ocean that is only partially offset by summer outgassing.

Overall, the ΔO_2 time series measured by these floats show a remarkable consistency between the 2-3 years measured, especially given that most of these floats are in a region as complex as the Kuroshio Extension. However, it is clear that supersaturation features are shared between floats and that some atypical features, such as the extremely high supersaturations measured by KE-C4 and KE-C5, should be considered separately from the rest of the measurements made by those floats. In order to better group ΔO_2 measurements and construct mean seasonal cycles for the different regions of the Pacific represented here, we use TS relationships and geographic position to separate float profiles, the results of which will be covered in the next section.

4.3.3 KE Supersaturation and air-sea flux by region

Dividing the Kuroshio Extension float measurements into the regions described in section 4.2.4 and Figure 4.3 illustrates a north-south trend in both observed supersaturation (Figure 4.6) and calculated mean monthly air-sea fluxes (Figure 4.7). Weekly mean supersaturation for each region are blue lines in Figure 4.6 with ± 1 s.d. represented by blue shading. Float profiles from the North KE measure the strongest supersaturations, with a peak in May over 5% ΔO_2 (Figure 4.6B). The spring increase of ΔO_2 up to the peak in May has both the quickest increase in supersaturation and the largest variance of any time period in any region. Surface waters in the North KE stay generally supersaturated until mid-September, though with some floats measuring at or near saturation. From mid-October to the end of March this region is strongly undersaturated in oxygen, with a mean of -3 to -5% ΔO_2.

The strong seasonal cycle in the supersaturation of the North KE region drives both a strong outgassing of oxygen during the summer and a much stronger influx of oxygen to the ocean during the winter, resulting in a mean annual flux of 6.8 mol O_2 m^{-2} yr^{-1} (Figure 4.8). The seasonal cycle in oxygen flux in the North KE is similar in shape to the Alaska Gyre in the northeast Pacific but is overall stronger. The summertime outgassing is slightly stronger, lasts for longer, and peaks earlier than the equivalent flux in the Alaska Gyre. The wintertime flux of oxygen to the ocean has a monthly peak that is over twice as strong as the monthly mean flux in the AG.

The Central KE is only weekly supersaturated during the summer, with the mean ΔO_2 consistently between 1 and 3% with no obvious peak. Winter undersaturation in this region is strong, beginning in October, two months earlier than in the North KE, and lasting through to the beginning of March. At its peak undersaturation of -4 to -5% in January (Figure 4.6), the undersaturation drives an average flux of 100 mmol O_2 m^{-2} d^{-1} into the ocean (Figure 4.7). In contrast to the North KE region, the wintertime flux is only weakly balanced by a summertime outgassing of oxygen, which yields a much stronger mean influx of 10.5 mol O_2 m^{-2} yr^{-1} (Figure 4.8).

The South KE region has a smaller seasonal amplitude in saturation throughout the year than either of the more northern regions (Figure 4.6). The summertime is more consistently supersaturated than the Central KE, at 1-3% with a peak in June, but significantly less supersaturated than the North KE. Wintertime waters are mainly near saturation from October through March with a low in January and February of -1 to -2% ΔO_2. Air-sea oxygen fluxes in the South KE region range from -10 mmol O_2 m^{-2} d^{-1} in the summer to 20 mmol O_2 m^{-2} d^{-1} in the winter (Figure 4.7). The stronger winter fluxes only last for a few months and are approximately balanced by the longer duration of the weaker summer fluxes, giving a mean net flux of 0.5 mol O_2 m^{-2} yr^{-1} (Figure 4.8).

4.4 Discussion

4.4.1 Magnitude and spatial variability of oxygen fluxes

In this study, we found a roughly balanced seasonal cycle of air-sea oxygen flux in the Alaska Gyre, subtropical South Pacific, and southern Kuroshio Extension, and a strong annual influx of oxygen into the central and northern Kuroshio Extension. Ocean Station Papa, in the Alaska Gyre, has been the site of a number of previous studies net oxygen flux from the ocean. Previous studies found an average flux out of the ocean of 2.3 ± 0.6 mol O_2 m^{-2} yr^{-1} (Emerson 2014), but mainly considered summertime fluxes in the mixed layer. This study supports previous work by the authors (Bushinsky and Emerson 2015), which found that the wintertime oxygen flux into the ocean at OSP mainly offsets summertime outgassing, leading to net oxygen outgassing of -0.3 mol O_2 m^{-2} yr^{-1}.

In the Kuroshio Extension, the observed seasonal cycle in supersaturation matches previous patterns of winter-summer zonal differences (Boyer et al. 1999; Garcia et al. 2005) of a maximum winter-summer difference at 45°N, closest to our North KE region, that decreases to the south with near 0 winter-summer difference at the equator. Mean cumulative fluxes for each region match closely in magnitude and spatial pattern to modeled global oxygen fluxes. In McKinley (2003), strong oxygen fluxes to the ocean are calculated for the Kuroshio Extension area from a global ocean circulation and biogeochemistry model, from a flux in to the ocean of ~8-9 mol O_2 m^{-2} yr^{-1} in the area corresponding to the North and Central KE regions in this study to between 0-4 mol O_2 m^{-2} yr^{-1} in the South KE. Annual mean oxygen fluxes from six global climate models are compared in Resplandy et al. (2015), indicating similar patterns in the KE region of >10 mol O_2 m^{-2} yr^{-1} in the center of the KE, dropping off rapidly to the north and south. The values from the present study are 6.8 mol O_2 m^{-2} yr^{-1} (North KE), 10.5 mol O_2 m^{-2} yr^{-1} (Central KE), and 0.5 mol O_2 m^{-2} yr^{-1} (South KE) (Figure 4.8).

Oxygen and carbon dioxide fluxes are both influenced by physical and biological processes. Increases (decreases) in solubility from cooling (warming) of water will drive oxygen and carbon dioxide fluxes in the same direction, while photosynthetic production of organic carbon consumes dissolved inorganic carbon (DIC, lowering pCO_2) while producing oxygen. Mixing of deep, old water will bring up low oxygen water in roughly Redfield ratios to excess DIC. In the Kuroshio Extension region, the strong CO_2 flux into the ocean has been attributed to equal parts solubility and biology plus mixing (Takahashi et al. 2002) and to a mixture of biology and geostrophic advection of DIC (Ayers and Lozier 2012).

The annual fluxes in the Kuroshio Extension (Figure 4.8) are the sum total of summertime outgassing and wintertime influx to the ocean. The summertime flux to the atmosphere is driven by both biological production and the warming of the shallow mixed layer, which reduces the solubility and increases ΔO_2. We can estimate the portion of summertime outgassing that is due to changes in solubility by multiplying the average summer mixed layer depth by the temperature change from the start of the summertime outgassing to the start of winter, when the oxygen flux changes sign and gas moves into the ocean. The total mean summertime flux of oxygen in the

KE is -3.5, -0.9, and -1.7 mol m^{-2} yr^{-1} for the North, Central, and South KE regions, respectively. Of this, -0.9, -0.7, and -0.4 mol m^{-2} yr^{-1} can be explained from decreased solubility in the mixed layer, which results in a calculated summertime biological flux of -2.6 mol O_2 m^{-2} for the North KE region, -0.2 mol O_2 m^{-2} for the Central, and -1.3 mol O_2 m^{-2} for the South KE region. No significant increase in sub mixed layer oxygen is observed for any of these regions, implying that the majority of summertime NCP occurs in the ML. While this does not equal the annual net community production (ANCP), it does give an estimate for summertime production and an approximation of the portion of the total flux that could be due to biology.

Yasunaka et al. (2013) produced maps of March-July net community production for the North Pacific from DIC drawdown calculated from surface measurements of pCO_2 and estimates of alkalinity determined from empirical relationships to salinity and temperature. In the area that most closely matches our North KE region, Yasunaka et al. (2013) calculate an NCP of 14 ± 5 mmol C m^{-2} d^{-1}, which equates to 3 ± 1.1 mol O_2 m^{-2} over the summer productive period, equivalent to our summertime estimate of 2.6 mol O_2 m^{-2}. To the south, NCP rapidly decreases and is not calculated further south of 28°N in the Yasunaka et al. (2013) estimate, making it difficult to compare the Central and South KE regions, though the general pattern of higher NCP in the heart of the Kuroshio Extension and less to the south is consistent with our interpretation.

From the end of summer into the end of winter, cooling temperatures and deepening mixed layer depths allow the water to take up large amounts of oxygen. As the mixed layer deepens, it entrains the water and oxygen below until winds relax at the end of winter and the mixed layer shoals. If we compare the average oxygen concentration down to the depth of the deepest mixed layer at the start of the winter to the saturation oxygen concentration based on the mixed layer temperature at the end of the winter, we can calculate the approximate wintertime oxygen uptake due to solubility alone. Multiplying the change in concentration by the change in mixed layer depth gives the oxygen flux to the ocean below the summertime mixed layer depth. This solubility driven flux is 3.3 mol O_2 m^{-2} for the North KE, 5.7 mol O_2 m^{-2} for the Central KE, and 0.4 for the South KE. The amplitude of the seasonal change from the point of maximum outgassing at the end of the summer to the final annual net O_2 flux is 10.0, 11.2, and 2.1 mol O_2 m^{-2} for the North, Central, and South KE, respectively, of which the solubility driven flux is responsible for 33%, 51%, and 19%.

After the mixed layer shoals, this deep water is removed from contact with the atmosphere until the next seasonal increase in mixed layer depth. If the Kuroshio Extension water is roughly following its mean path to the northeast, this water will be replaced by fresh water in this location the following year. If these profiling floats were surface drifters, they would follow the current out into the central Pacific. Instead, due to differences in mean flow between the surface ocean and the deep ocean (Jayne et al. 2009), they have largely re-circulated in the Kuroshio Extension. This means that despite measuring a roughly unchanging seasonal temperature cycle, the change in solubility during the winter drives a strong flux of oxygen into the ocean in this region.

Changes in solubility partially explain how the ocean takes up oxygen, but if the water does not leave the region, solubility changes alone will not result in a net flux of oxygen. Of the oxygen that is taken up by the ocean and stored in the deep wintertime mixed layer, part is advected horizontally along the Kuroshio Extension and part is subducted during mode water formation (Suga et al. 2004, 2008). The site of subtropical mode water (STMW) formation occurs around the boundary between our North and Central KE regions, centered on the deepest wintertime mixed layer depths where subduction rates reach ~150 m yr^{-1}. Average subduction rates for the North, Central, and South KE regions are approximately 50 m yr^{-1}, 125 m yr^{-1}, and 50 m yr^{-1}, respectively. This is the height of the wintertime mixed layer that subducts down and out of contact with the atmosphere each year. This water is replaced by warmer water from the southwest that holds less oxygen. The approximate flux from wintertime subduction can be determined by multiplying the concentration difference between source waters and subducted waters by the subduction rate. Source waters for the North KE are mainly the Central KE, and the Central KE is supplied by the South KE (Suga et al. 2008). Average annual ML [O_2] for the Central and South KE regions provides an estimate of source [O_2] for the North and Central KE regions, respectively. South KE source [O_2] can be determined from World Ocean Atlas climatology. From these calculations, we determine a subducted flux of -2 mol O_2 m^2 yr^{-1} for the North KE, -1.6 mol O_2 m^2 yr^{-1} for the Central KE, and -1.4 mol O_2 m^2 yr^{-1} for the South KE.

These estimations comparing expected oxygen fluxes due to solubility and calculated fluxes from oxygen measurements do not include any vertical diffusion of oxygen. In Bushinsky and Emerson (2015), diapycnal diffusivity contributed -0.9 mol O_2 m^{-2} yr^{-1} to the annual flux. In the KE, with deeper mixed layer depths (reaching stronger negative oxygen gradients) and larger diapycnal diffusivity coefficients (Cronin et al. 2013, 2015) the removal of oxygen from diapycnal diffusion will be larger.

The total air-sea flux of oxygen to the ocean must be balanced by the sum of biological outgassing to the atmosphere and physical losses due to horizontal and vertical advection and diffusion. In the North KE, the annual net O_2 flux is 6.8 mol m^{-2} yr^{-1}. A calculated subduction flux of 2 mol O_2 m^{-2} yr^{-1} and a biological flux of -2.6 mol O_2 m^{-2} yr^{-1} leaves 7.4 mol O_2 m^{-2} yr^{-1} added to the ocean over an annual cycle that must be balanced by respiration, horizontal advection, and diffusion. The equivalent unexplained O_2 fluxes for the Central and South KE regions are 9.1 and 0.4 mol O_2 m^{-2} yr^{-1}, respectively. Given the large magnitude of the total flux and the component physical fluxes, it would be difficult to estimate the annual contribution of biology using a mass balance approach for the Kuroshio Extension region. A more detailed box model approach in the future may be able to help resolve horizontal advective losses from the KE regions.

Float SSP, in the south subtropical gyre, measured a net flux to the ocean of 0.6 mol O_2 m^{-2} yr^{-1}. Modeled O_2 fluxes in McKinley et al. (2003) and Resplandy et al. (2015) display an influx to the ocean directly on the equator in the eastern half of the Pacific that transitions to a moderate flux out of the ocean further into the South Pacific subtropical gyre. Float SSP falls in this area of modeled outgassing. With only one full year of data from float SSP it is unclear if this represents interannual variability or a disagreement between measurements and climate models.

4.4.2 Importance of bubbles to air-sea flux parameterization

Many gas flux parameterizations are developed for carbon dioxide and do not use explicitly defined bubbles, instead opting for a saturation and wind speed dependent gas exchange term that parameterizes the total air sea flux. Oxygen is less soluble and more influenced by bubble injection that forces gas into the ocean. In our calculations using the Liang et al. (2013) parameterization described in section 4.2.3, the combined large and small bubble flux was a significant portion of the total flux most months and regions (Figure 4.7). For 5 months in the winter (Nov-Mar for northern hemisphere floats, May-Sept. for SSP), bubble injection represented greater than 50% of the total oxygen flux into the ocean. In months when the oxygen supersaturation was close to zero, such as October in the Alaska Gyre (float OSP) or September in the Central KE (Figure 4.6), slight mean supersaturation drives a diffusive flux out of the ocean, but a larger bubble flux forces the net oxygen flux in to the ocean. The bubble flux is much less important during the summer, when low wind speeds and high supersaturations favor the diffusive transfer of oxygen across the air-water boundary.

In order to assess the impact of direct parameterization of bubbles, we re-calculated air-sea fluxes for the different regions using the Wanninkhof (2014) parameterization which can be calculated using equation (4.1), setting $F_c = F_p = 0$, and equation (4.2) where:

$$k_{O2} = 6.97\times10^{-7}(U_{10})^2\left(\frac{S_{O2}}{660}\right)^{-0.5} \qquad \mathrm{m\ s^{-1}}, \tag{4.9}$$

k_{O2}, the mass transfer coefficient, is more sensitive to wind speed in this parameterization than in the Liang et al. (2013) calculations, increasing the contribution by diffusive flux alone. The Wanninkhof (2014) parameterization was developed from bomb ^{14}C CO_2 measurements and purposeful tracer releases, but according to the paper is appropriate for other gases below 15 m s^{-1}, which covers the vast majority of data points in this study.

Mean annual fluxes into the ocean for all regions were between 1.2 and 4.8 mol m^{-2} yr^{-1} less using Wanninkhof (2014) than the Liang et al. (2013). The largest changes across all regions were due to an approximate 1/3 reduction in gas flux to the ocean during the peak winter flux. In the AG, where we calculated a relatively balanced cumulative flux of -0.3 mol O_2 m^{-2} yr^{-1}, the net oxygen flux out of the ocean increases by an order of magnitude to -3.2 mol O_2 m^{-2} yr^{-1}. The North and Central KE regions both saw a reduction in O_2 flux to the ocean of ~4.5 mol O_2 m^{-2} yr^{-1}, resulting in 2.5 and 5.7 mol O_2 m^{-2} yr^{-1} respectively. In the South KE and S. Subtropical Gyre, for which we calculated 0.5, and 0.6 mol O_2 m^{-2} yr^{-1} respectively, the sign of the flux changed to -0.9 and -0.6 mol O_2 m^{-2} yr^{-1}, or a net outgassing using the Wanninkhof (2014) parameterization.

The importance of bubble injection to the annual O_2 flux partially decouples the air-sea oxygen flux from ΔO_2 and therefore from temperature-induced solubility changes. The relationship between oxygen solubility and temperature is used to estimate future decreases in ocean oxygen content due to global warming (Keeling et al. 2010). The decoupling of oxygen fluxes driven by air-sea oxygen differences due, in part, to solubility, could have a significant impact on the relationship between warming and ocean oxygen content.

4.5 Conclusions

In this study, we show that air calibrated profiling floats can measure oxygen with sufficient accuracy to capture seasonal cycles in several regions of the Pacific Ocean. Air measurements using oxygen optodes provide the air-sea difference in the partial pressure of oxygen, which results in high accuracy of calculated fluxes regardless of the accuracy of pressure data. The result is seasonal cycles of percent supersaturation that can be separated by water mass and geographic area and used to estimate regional oxygen fluxes. Comparison of air-sea O_2 and CO_2 fluxes adds to our understanding of the drivers behind large-scale patterns of CO_2 uptake.

In the Kuroshio Extension regions, the annual flux of oxygen to the ocean is among the largest in the Pacific, despite water that is never undersaturated by more than ~4%. This is in large part due to bubble injection during the wintertime, which partially uncouples the oxygen flux from supersaturation. The solubility pump is likely responsible for 1/3 to 1/2 of the mean annual oxygen flux to the ocean. Between 1.4 and 2 mol m^{-2} yr^{-1} of this oxygen flux to the ocean is removed by the subduction of winter water high in oxygen. The seasonal cycle in mixed layer depth is a significant factor in the solubility pump and subduction. Without deep mixed layers in the winter, the surface ocean could not take up such large amounts of oxygen while still maintaining a low supersaturation. Furthermore, deep mixed layers are linked to mode water formation sites, which remove a significant fraction of water and oxygen each year.

With the large total and physical fluxes estimated in the KE, it would be difficult to estimate net annual biological production from these measurements, but we can estimate a summertime production of up to 2.6 mol O_2 m^{-2} in the North KE, with less production to the south. By comparing the fluxes we can estimate, biological production and winter subduction, we can assess the magnitude of the residual fluxes and potentially use these in the future to constrain fluxes due to horizontal advection and diapycnal diffusion, which must be very large for the North and Central KE regions. Explicit bubble injection in the air-sea flux parameterization is crucial to calculating an accurate total flux. Bubbles are especially important during winter months when wind speeds are high or ΔO_2 is close to saturation. Estimates of air-sea oxygen flux that do not include bubbles underestimate the wintertime input of oxygen and other insoluble gases to the ocean.

Estimates of regional oxygen supersaturation and air-sea flux over multiple years will help to constrain spatial and interannual variability in the oxygen cycle. The regions chosen for this study displayed clear differences in seasonal cycles, though still with intra-regional variability, for example in the Central KE. This could be evidence of variability within the region or evidence that the region should be separated further into smaller biogeochemical areas. The Kuroshio Extension represents a highly advective region with very large physical and biological fluxes of oxygen. Averaging multiple profiles within an area will remove some detail from specific physical and biological events, but provides a mean look at the area and helps to present a more comprehensive picture of regional biogeochemical variability, even in a complex region like the KE. With recent increases in the use of air measurements to calibrate profiling oxygen floats, more measurements over greater areas will soon allow calculation of basin-wide and global oxygen fluxes.

4.6 Tables

Table 4.1. Summary of float locations and number of profiles in each Kuroshio region.

Float name	UW float #	WMO #	Date deployed	Deployment position	Number of profiles in KE regions: North	Central	South
OSP	8397	5903743	Jun-02 2012	50.0N, 144.8W	-	-	-
KE-N	8381	5904028	Mar-04 2013	40.5N, 149.7E	175	0	0
KE-C1	7665	5904033	Mar-04 2013	39.3N, 149.3E	142	40	0
KE-C2	8382	5904025	Mar-03 2013	38.2N, 149.0E	61	118	2
KE-C3	8394	5904031	Mar-01 2013	34.7N, 147.9E	35	148	2
KE-C4	8387	5904027	Feb-28 2013	33.5N, 147.5E	77	77	34
KE-C5	8375	5904030	Feb-28 2013	32.3N, 147.1E	102	70	0
KE-C6	8372	5904026	Feb-28 2013	31.2N, 146.8E	31	122	37
KE-S	5328	5904029	Feb-27 2013	30.0N, 146.4E	0	22	172
SSP	8485	5904147	Jan-01 2014	15.8S, 159.0W	-	-	-

Argo float names, deployment information, and number of profiles in each study region for SOS-Argo floats built at the University of Washington. Float names stand for: OSP, Ocean Station Papa; KE-N, Kuroshio Extension-North; KE-C, Kuroshio Extension-Central; KE-S, Kuroshio Extension-South; and SSP, south subtropical Pacific. UW float # and WMO # are used to find data through the UW and the international Argo program. Kuroshio Extension regions are defined in section 4.2.4 and Figure 4.3. For each float, the number of profiles sorted into each KE region is listed. For example, Float KE-C6 primarily contributed data to the Central KE region (122 profiles), but also contributed 31 and 37 profiles to the North and South KE regions, respectively.

4.7 Figures

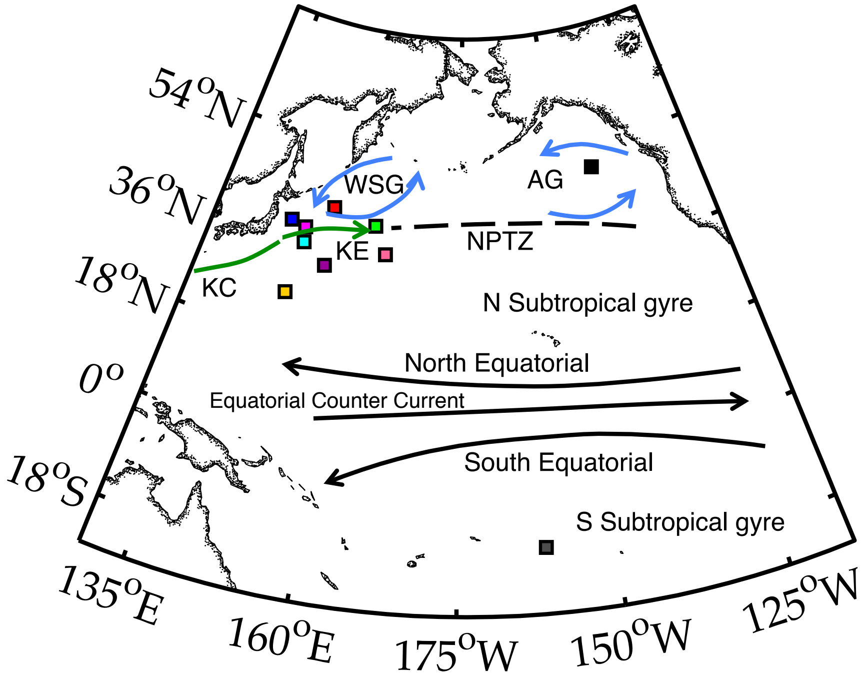

Figure 4.1. Important water masses near float locations in the Pacific. In the western Pacific, the Kuroshio Current (KC) brings warm water north into the Kuroshio Extension (KE), where it cools and continues into the North Pacific Transition Zone (NPTZ). The NPTZ is an area of enhanced chlorophyll and productivity that separates the subarctic Western Subarctic Gyre (WSG) and Alaska Gyre (AG) from the north subtropical gyre. The subtropical gyres in the north and south Pacific are oligotrophic regions bounded on the equator side by the west flowing equatorial currents. The location of the KE and NPTZ vary on seasonal and interannual timescales. August 2015 locations of the floats used in this study are indicated by colored squares that match the color scheme in Figures 4.2 and 4.7. Currents and water mass locations from (Hayward 1997; Harrison et al. 2004; Chierici et al. 2006; Ayers and Lozier 2010)

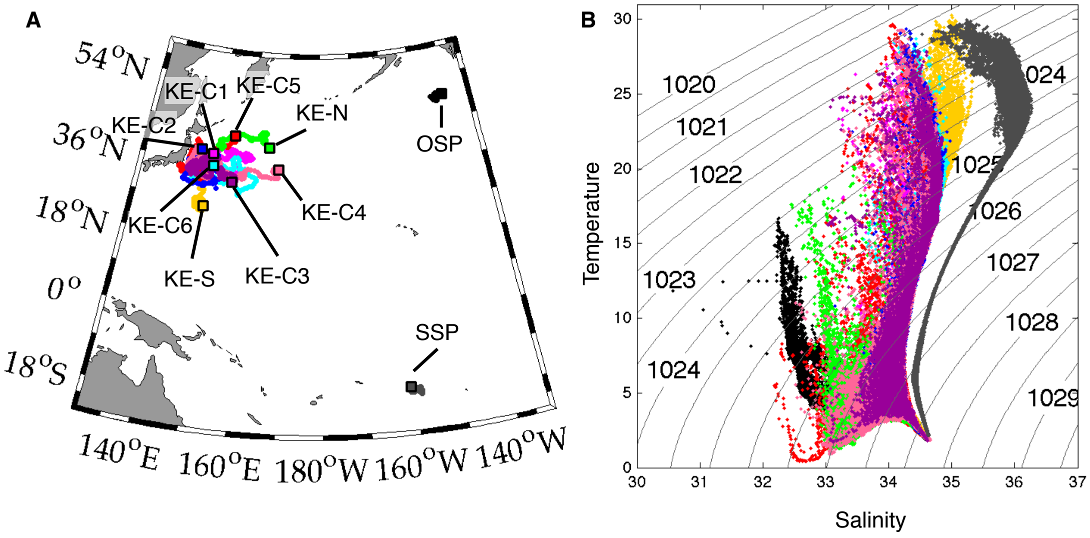

Figure 4.2. Float tracks and temperature/salinity plot. Float tracks (A) are marked by color, with the location as of August, 2015 marked with a black box and float serial number. Temperature and salinity from all float profiles (down to 2000 db) are plotted over isopycnals, showing the different water properties each float has passed through. At their deepest depth, each float enters common water with a temperature of ~2°C and a salinity of ~34.6.

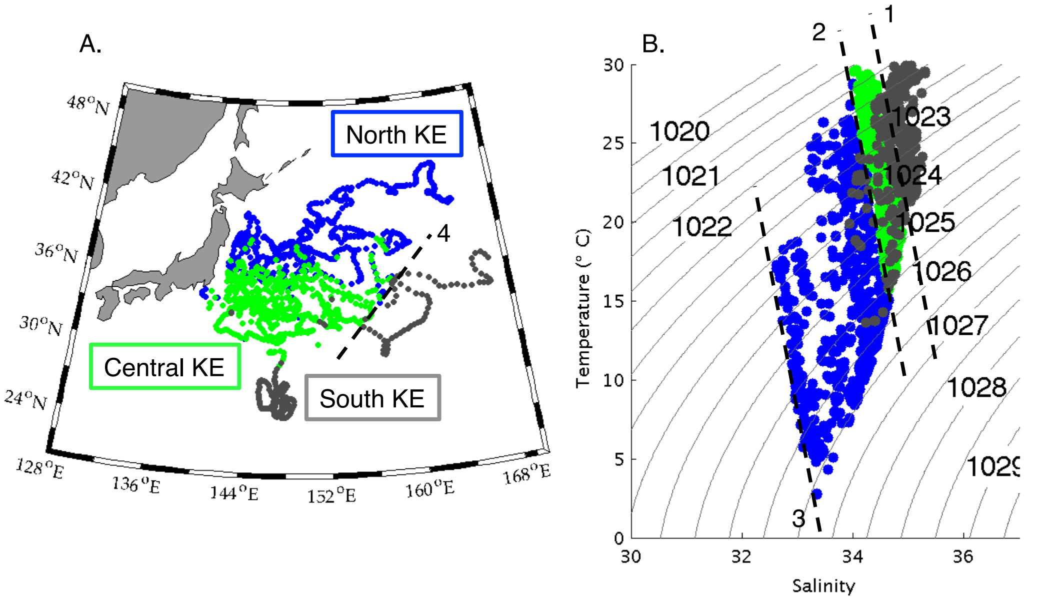

Figure 4.3. Kuroshio Extension region divided into three biogeochemical regions based on geographic location (A) and temperature salinity relationships of the surface measurements (B). The three regions (North KE, blue; Central KE, green; and South KE, gray) are primarily split along the black dashed lines in the TS plot (B). The North KE and Central KE regions were divided along line 2 in the TS plot. This separates surface measurements following the north and south seasonal movement of the KE. Colder, fresher coastal measurements with anomalously high oxygen supersaturations were removed from the North KE region along line 3. The Central KE and South KE regions were primarily split along line 1 in the TS plot, with the gray points east of line 4 in (A) added to the South KE region due to oxygen supersaturation measurements that matched closely with the rest of the region.

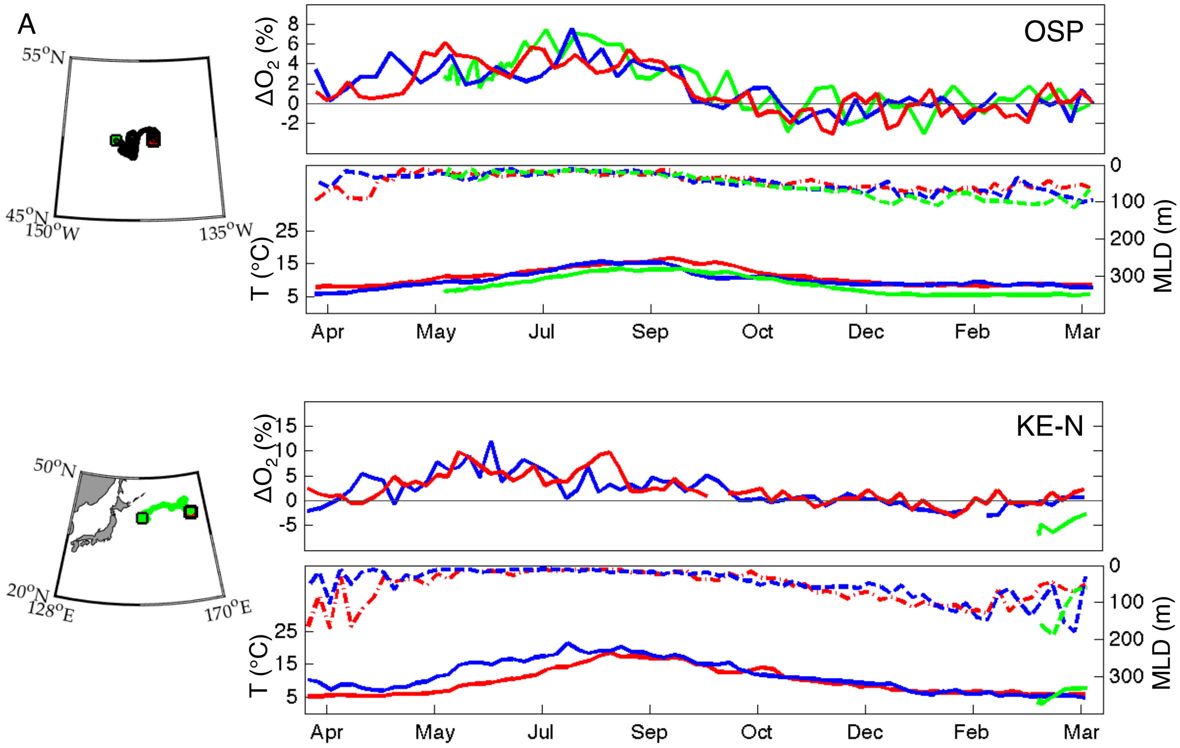

Figure 4.4. Oxygen supersaturation (ΔO$_2$), temperature (T), and mixed layer depth (MLD), and track plotted for all floats and labeled by float name. Each year of data are overlaid, with Apr. 2012-Mar. 2013 in green, Apr. 2013 – Mar. 2014 in blue, and Apr. 2014 – Mar. 2015 in red. Floats are organized roughly from North-South. Supersaturation, temperature, and mixed layer depth follow seasonal cycles of warming waters in the spring-summer associated with increased supersaturation and shallow mixed layer depths. From fall to winter mixed layer depths deepen and temperatures cool, increasing solubility and decreasing supersaturation. Floats KE-C4 and KE-C5 passed through cold, highly supersaturated waters in April and May 2014 that are clear outliers from the rest of the seasonal cycles. In order to accommodate the range of supersaturations measured (-10% – 53%), the y-axis limits for ΔO$_2$ are different for each float. Individual float tracks are plotted to the left of each pair of plots.

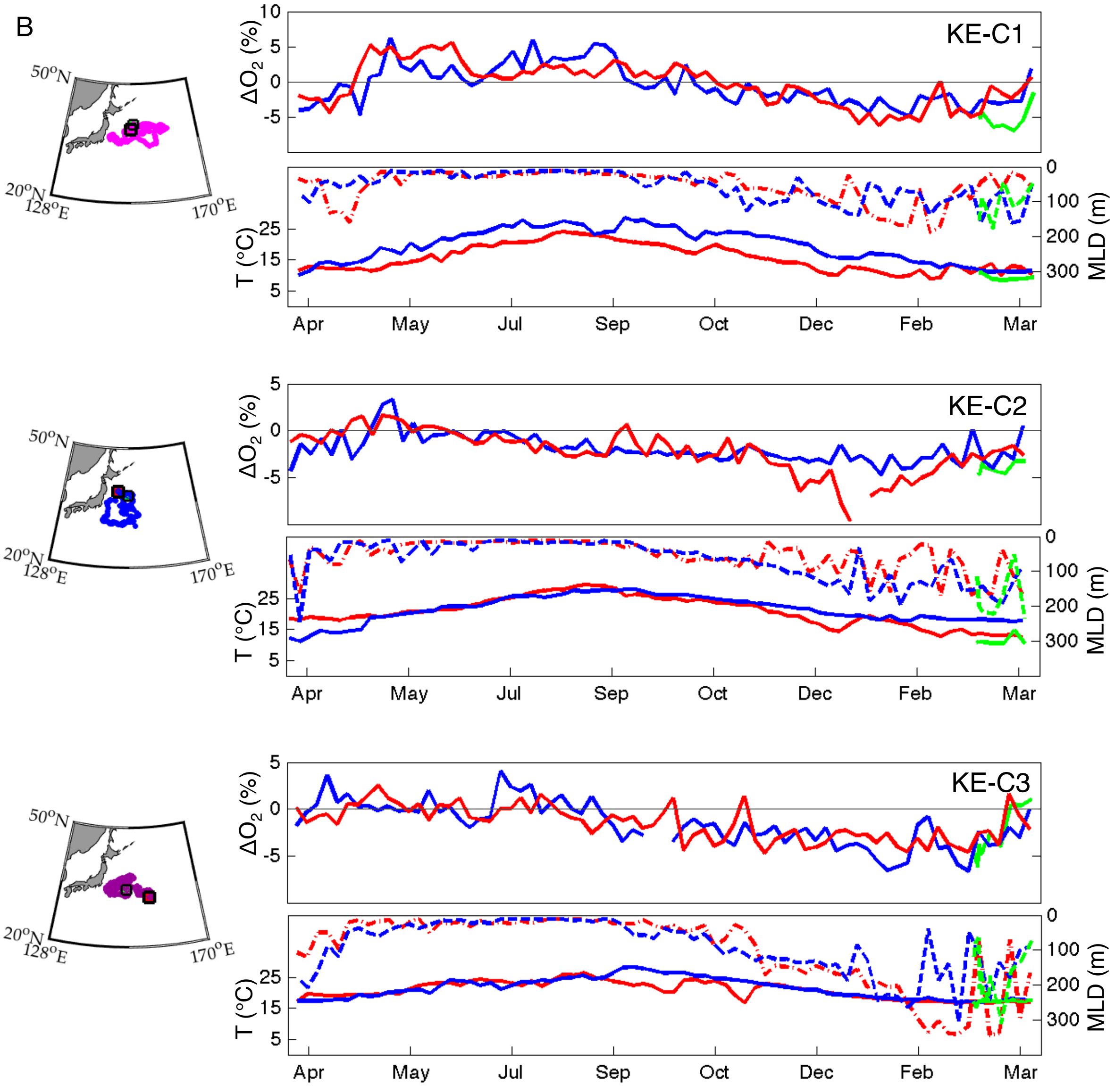

Figure 4.4 (continued).

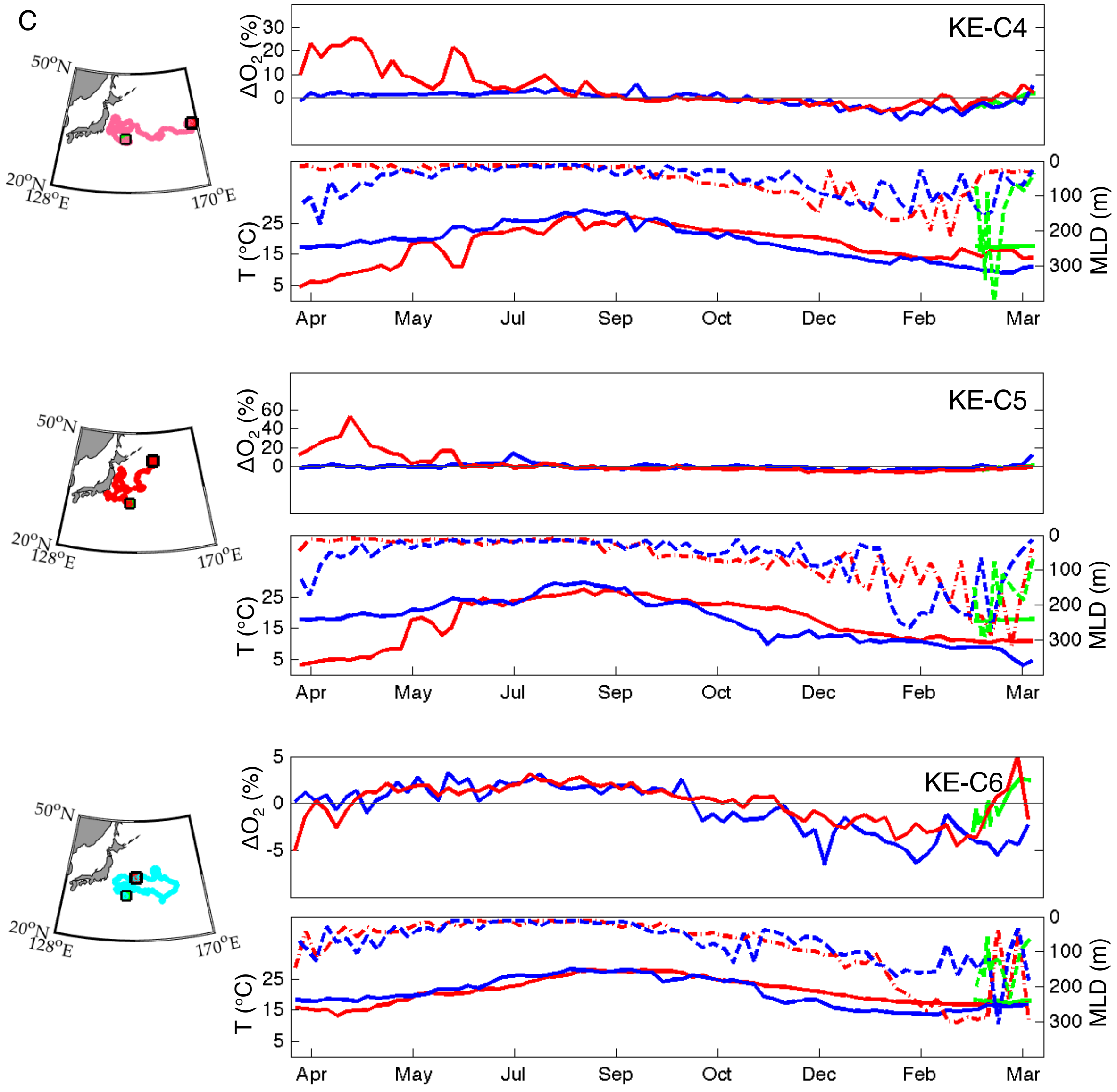

Figure 4.4 (continued).

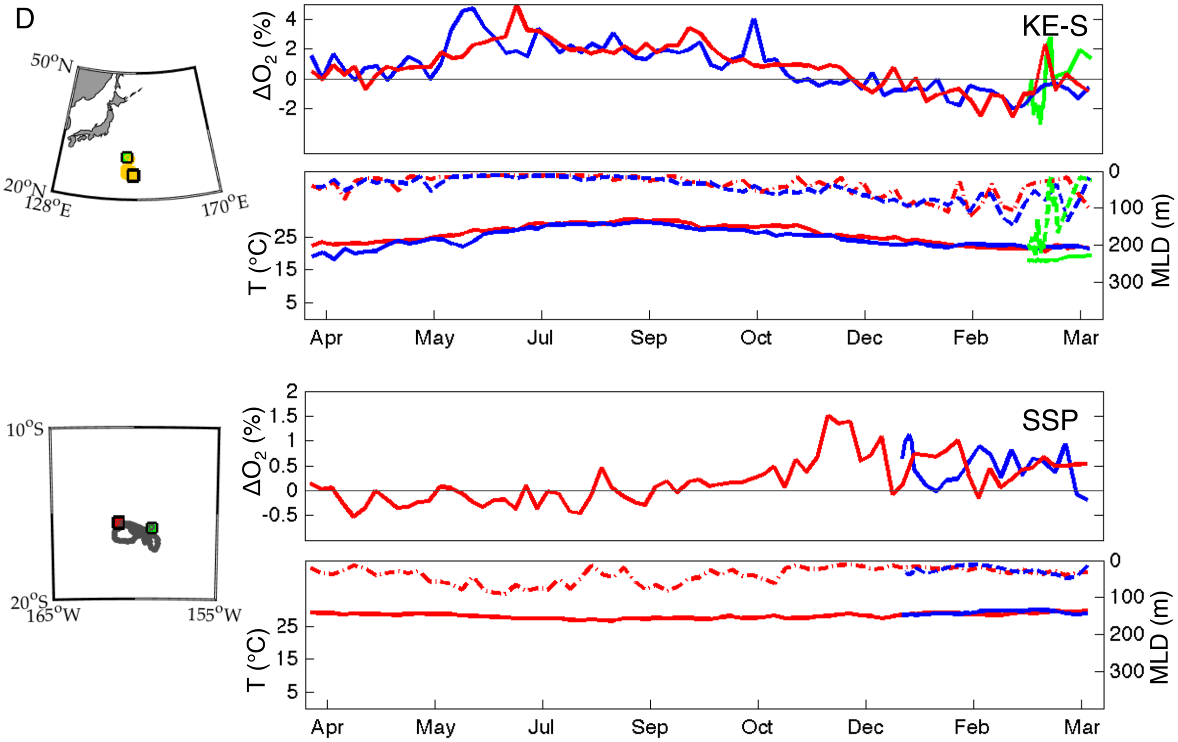

Figure 4.4 (continued).

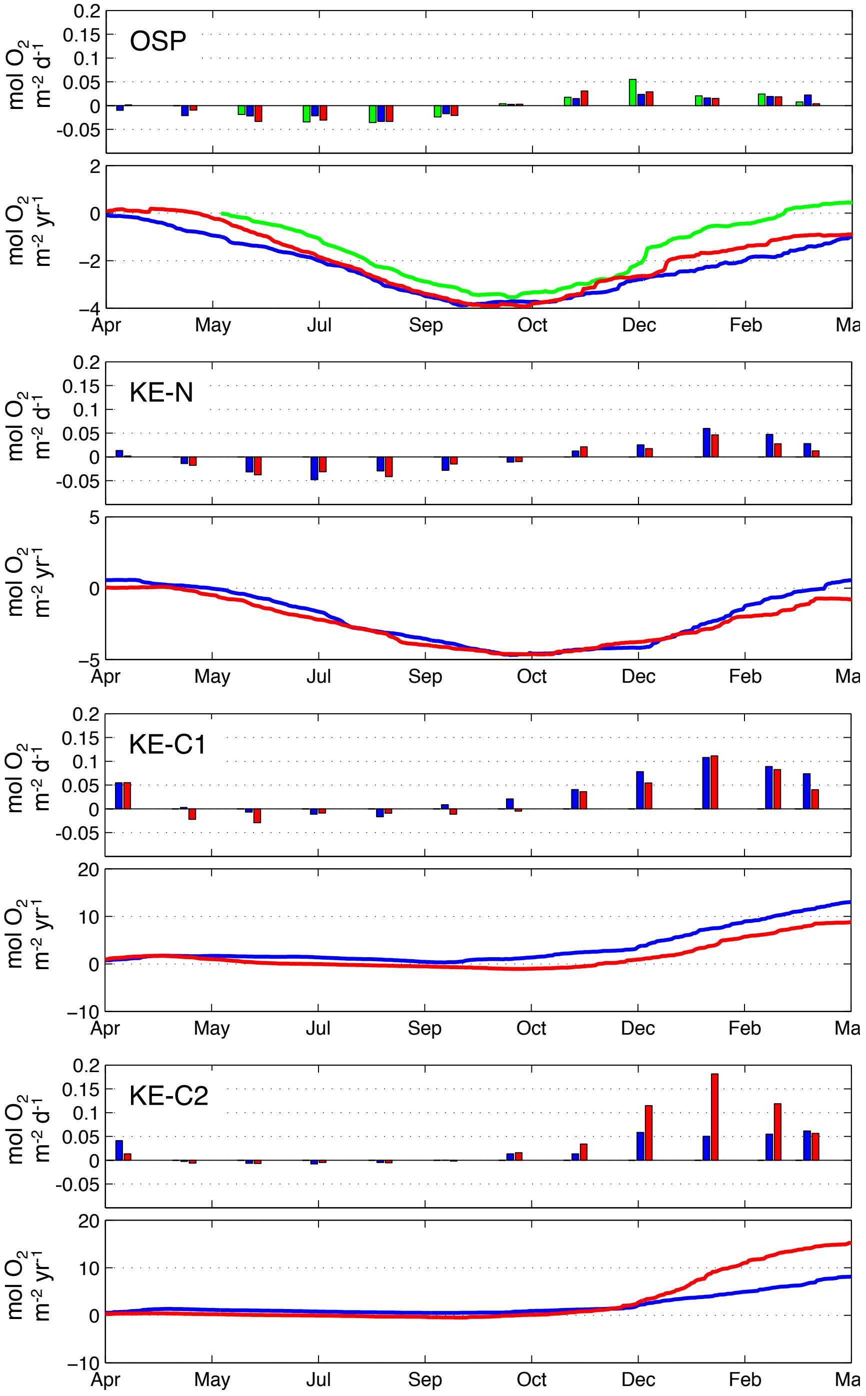

Figure 4.5. Monthly and cumulative air-sea oxygen fluxes. Daily oxygen fluxes were calculated for each float according to section 4.2.3 and equations (4.1) – (4.8). Monthly average fluxes (mol O_2 m^{-2} d^{-1}) are bars in the upper plots for each float with colors corresponding to year (2012, green; 2013, blue; 2014, red). Lines with the same color scheme are cumulative oxygen fluxes

(Apr.-Mar., mol m^{-2} yr^{-1}) in the lower plots. An increase in the lines indicates a net flux of oxygen to the water. To accommodate the range of fluxes, the Y-axes for cumulative plots have different scales.

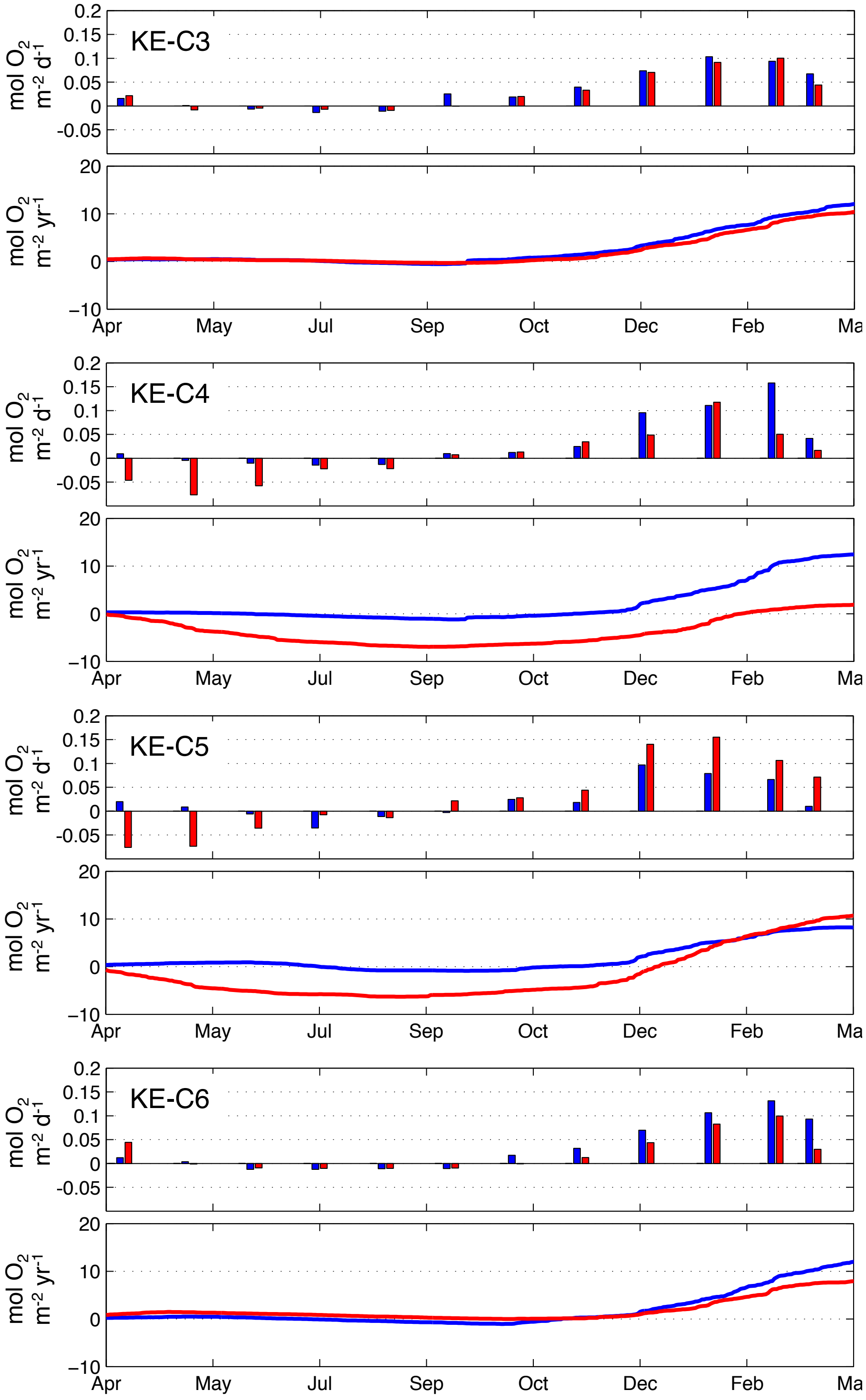

Figure 4.5 (continued).

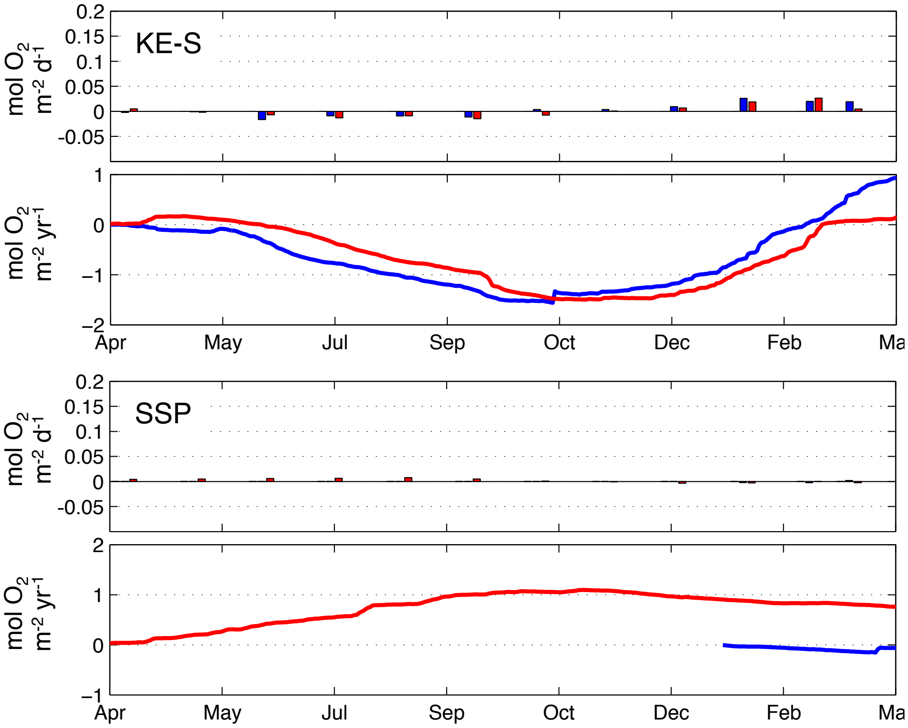

Figure 4.5 (continued).

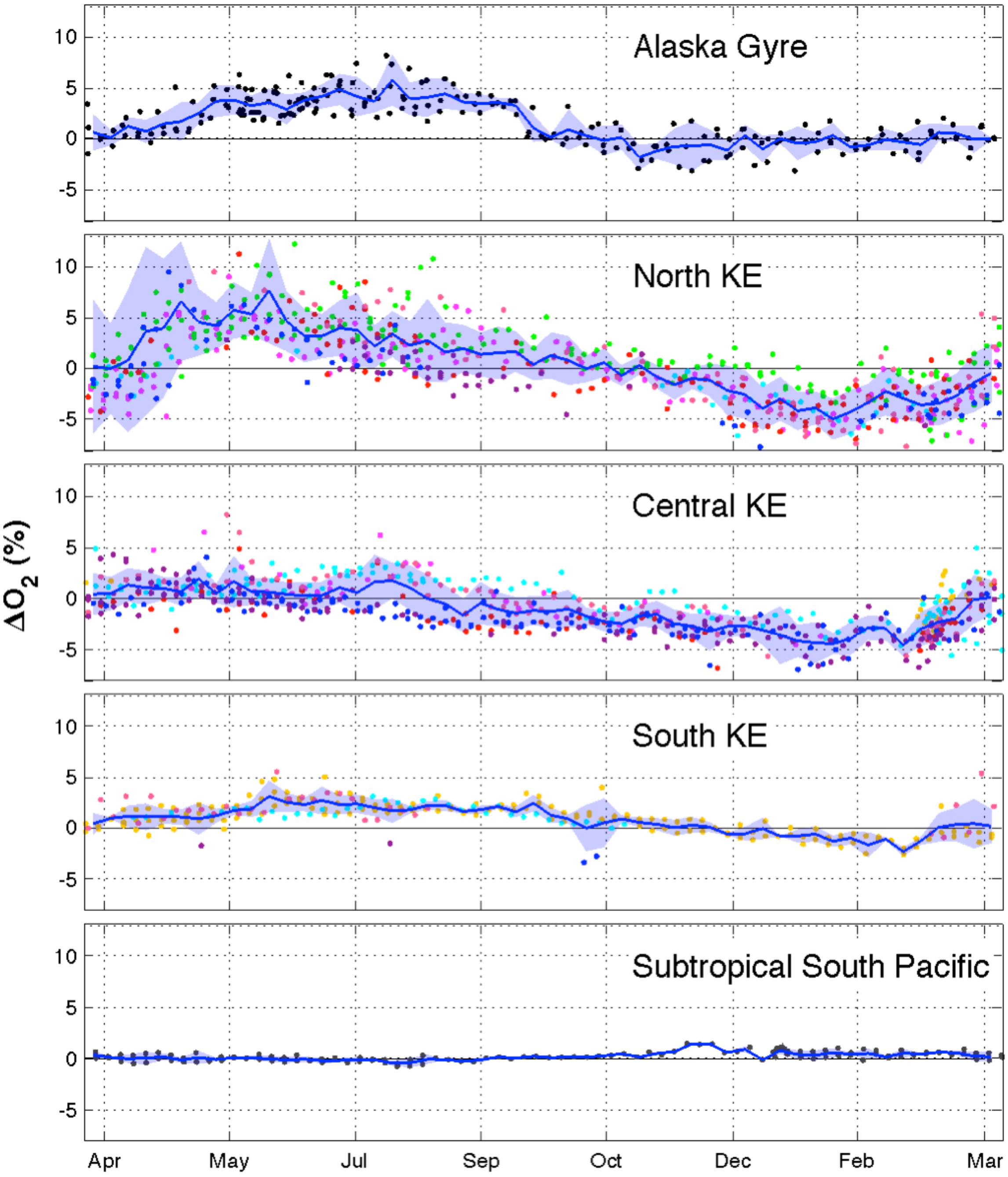

Figure 4.6. Percent supersaturation for each region. Surface supersaturation from all floats and years are plotted against year-day. Colored points represent a surface oxygen measurement, with the color indicating the float. Measurements are divided into separate regions by a combination of T-S relationships and geographic location (section 4.2.4, Figure 4.3). Blue lines and shaded

blue regions represent weekly means ± 1 standard deviation. The Alaska Gyre and S. Subtropical Gyre only contain data from floats OSP and SSP, respectively.

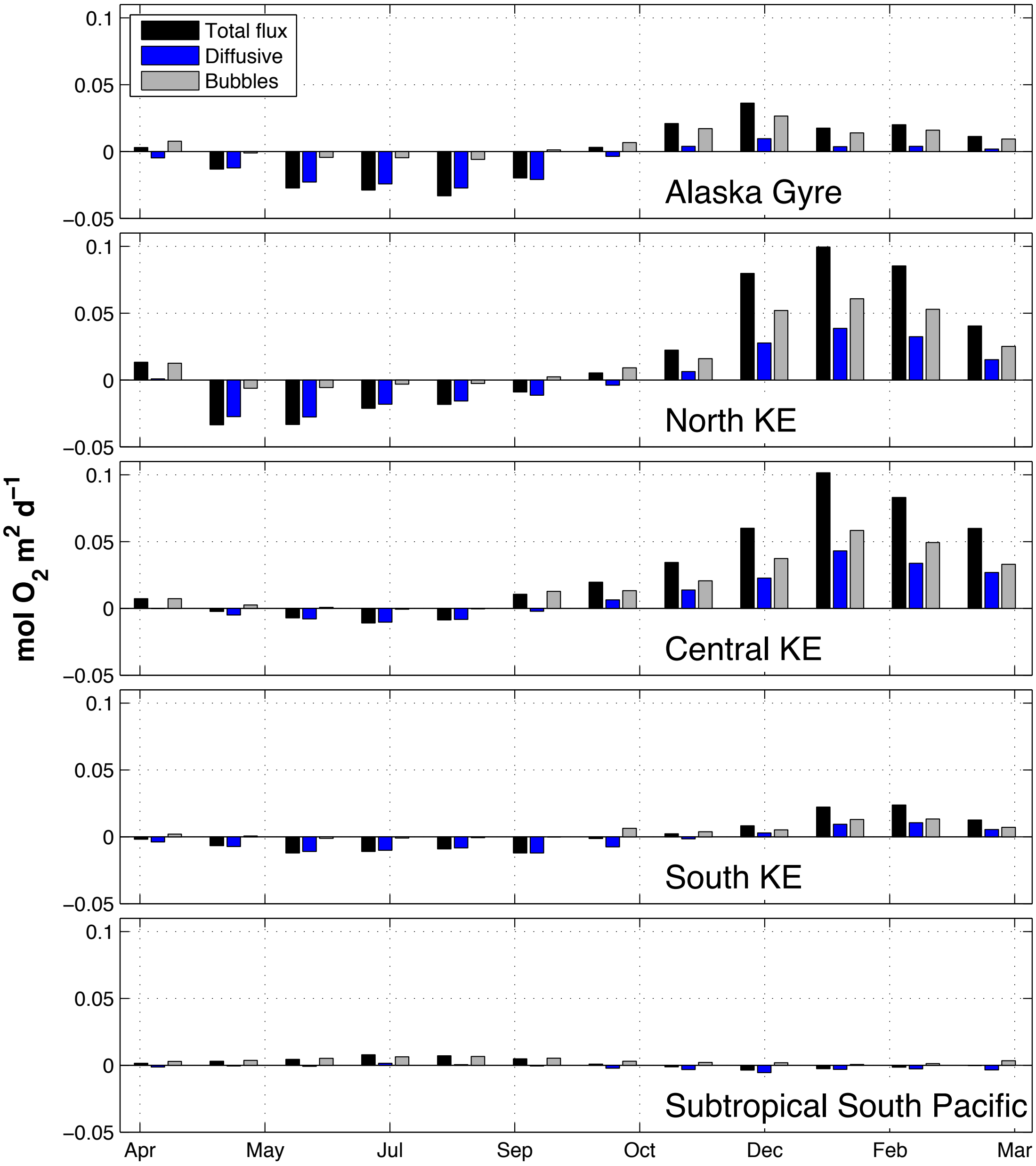

Figure 4.7. Monthly air-sea oxygen fluxes by region. Mean monthly total ($F_{A\text{-}W}$), diffusive (F_S), and combined bubble flux ($F_C + F_P$) plotted for each region in this study. Fluxes are calculated according to section 4.2.3 using the Liang et al. (2013) air-sea gas flux parameterization. The diffusive component of the air-sea flux is most important during the summer, when higher supersaturation and lower wind speed allows gas to diffuse without injecting bubbles into the

ocean. In the winter, high wind speeds drive bubbles into the ocean, making up over half of the total flux.

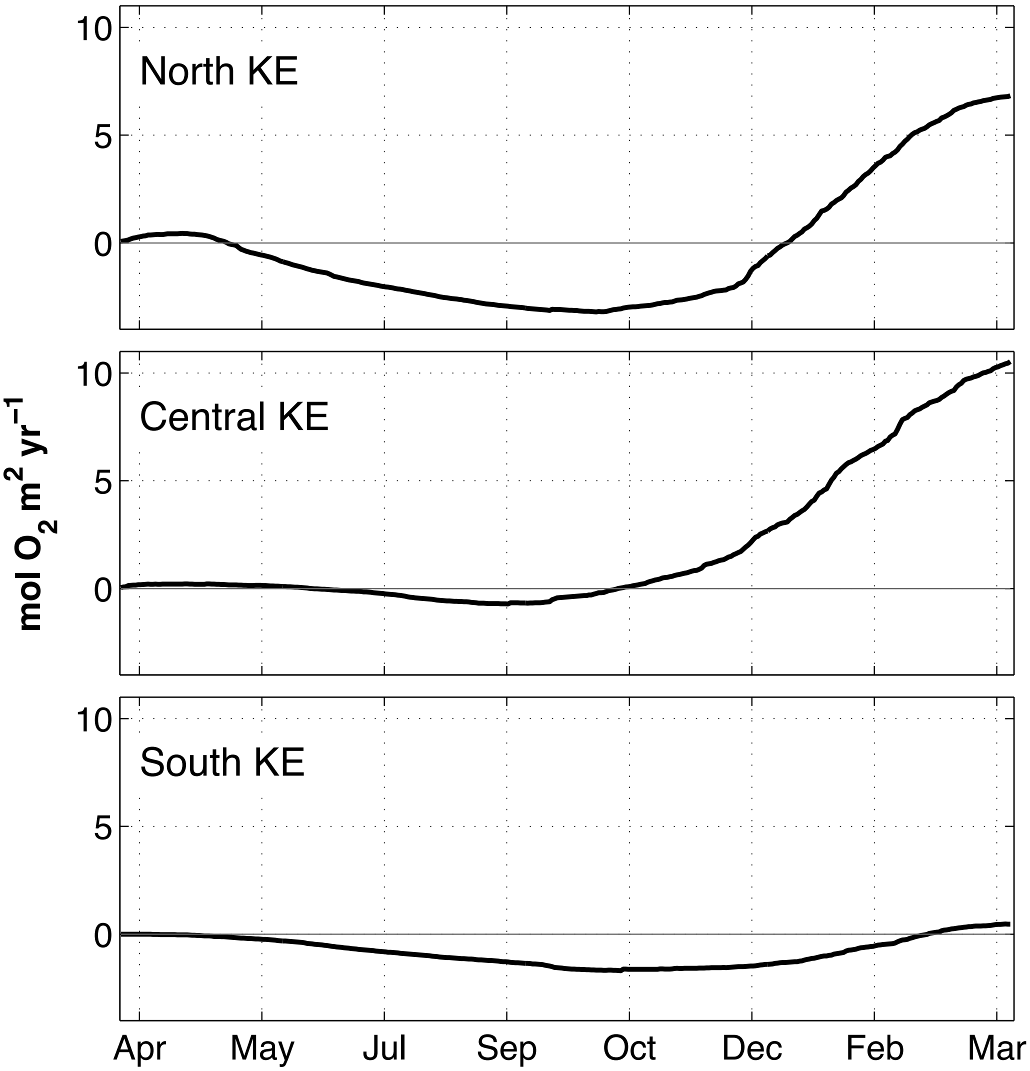

Figure 4.8. Mean cumulative oxygen fluxes for Kuroshio Extension regions. An increase in the lines indicates a flux of oxygen to the water, a decrease represents a flux to the atmosphere. Cumulative fluxes are calculated by averaging and adding daily fluxes calculated from float-measured supersaturation for each region. Total annual flux is represented by the right-hand point on each plot. Mean net O_2 flux is 6.8 mol m^{-2} yr^{-1} for the North KE, 10.5 mol m^{-2} yr^{-1} for the Central KE, and 0.5 mol m^{-2} yr^{-1} for the South KE. Cumulative flux plots for the Alaska Gyre (-0.3 mol m^{-2} yr^{-1}) and south subtropical gyre (0.6 mol m^{-2} yr^{-1}) can be found in Figure 4.5 for floats OSP (AG) and SSP (south subtropical Pacific gyre).

BIBLIOGRAPHY

Altabet, M. A. 2007. Constraints on oceanic N balance/imbalance from sedimentary 15N records. Biogeosciences Discuss. **4**: 75–86.

Ayers, J. M., and M. S. Lozier. 2010. Physical controls on the seasonal migration of the North Pacific transition zone chlorophyll front. J. Geophys. Res. Ocean. **115**: 1–11.

Ayers, J. M., and M. S. Lozier. 2012. Unraveling dynamical controls on the North Pacific carbon sink. J. Geophys. Res. **117**: C01017.

Bentamy, A., D. Croize-Fillon, and C. Perigaud. 2008. Characterization of ASCAT measurements based on buoy and QuikSCAT wind vector observations. Ocean Sci. **4**: 265–274.

Bingham, F. M., and R. Lukas. 1996. Seasonal cycles of temperature, salinity and dissolved oxygen observed in the Hawaii Ocean Time-series. Deep Sea Res. Part II Top. Stud. Oceanogr. **43**: 199–213.

Bittig, H. C., and A. Körtzinger. 2015. Tackling oxygen optode drift: Near-surface and in-air oxygen optode measurements on a float provide an accurate in-situ reference. J. Atmos. Ocean. Technol. **in press.**

Bograd, S. J., D. G. Foley, F. B. Schwing, C. Wilson, R. M. Laurs, J. J. Polovina, E. a. Howell, and R. E. Brainard. 2004. On the seasonal and interannual migrations of the transition zone chlorophyll front. Geophys. Res. Lett. **31**: 1–5.

Bopp, L., L. Resplandy, J. C. Orr, S. C. Doney, J. P. Dunne, M. Gehlen, P. Halloran, C. Heinze, T. Ilyina, R. Séférian, J. Tjiputra, and M. Vichi. 2013. Multiple stressors of ocean ecosystems in the 21st century: projections with CMIP5 models. Biogeosciences **10**: 6225–6245.

De Boyer Montégut, C., G. Madec, A. S. Fischer, A. Lazar, and D. Iudicone. 2004. Mixed layer depth over the global ocean: An examination of profile data and a profile-based climatology. J. Geophys. Res. **109**: C12003.

Boyer, T., M. E. Conkright, and S. Levitus. 1999. Seasonal variability of dissolved oxygen, percent oxygen saturation, and apparent oxygen utilization in the Atlantic and Pacific Oceans. Deep. Res. Part I Oceanogr. Res. Pap. **46**: 1593–1613.

Bushinsky, S. M., and S. Emerson. 2013. A method for In-situ Calibration of Aanderaa Oxygen Sensors on Surface Moorings. Mar. Chem. **155**: 22–28.

Bushinsky, S. M., and S. R. Emerson. 2015. Marine Biological Production from Remote In Situ Oxygen Measurements. Global Biogeochem. Cycles **(submitted)**.

Bushinsky, S. M., S. R. Emerson, S. C. Riser, and D. Swift. 2015. Accurate oxygen measurements on Argo floats using in-situ air calibrations. Manuscript

Charette, M. A., S. B. Moran, and J. K. B. Bishop. 1999. 234Th as a tracer of particulate organic carbon export in the subarctic northeast Pacific Ocean. Deep Sea Res. Part II Top. Stud. Oceanogr. **46**: 2833–2861.

Chierici, M., A. Fransson, and Y. Nojiri. 2006. Biogeochemical processes as drivers of surface fCO2 in contrasting provinces in the subarctic North Pacific Ocean. Global Biogeochem. Cycles **20**: 1–16.

Cronin, M. F., N. a. Bond, J. Thomas Farrar, H. Ichikawa, S. R. Jayne, Y. Kawai, M. Konda, B. Qiu, L. Rainville, and H. Tomita. 2013. Formation and erosion of the seasonal thermocline in the Kuroshio Extension Recirculation Gyre. Deep Sea Res. Part II Top. Stud. Oceanogr. **85**: 62–74.

Cronin, M. F., N. Pelland, S. Emerson, and W. R. Crawford. 2015. Estimating diffusivity from the mixed layer heat and salt balances in the North Pacific. J. Geophys. Res. Ocean. **Submitted**.

D'Asaro, E. A., and C. McNeil. 2013. Calibration and Stability of Oxygen Sensors on Autonomous Floats. J. Atmos. Ocean. Technol. **30**: 1896–1906.

Demas, J. N., B. A. DeGraff, and P. B. Coleman. 1999. Oxygen Sensors Based on Luminescence Quenching. Anal. Chem. News Featur. 793–800.

Deutsch, C., J. L. Sarmiento, D. M. Sigman, N. Gruber, and J. P. Dunne. 2007. Spatial coupling of nitrogen inputs and losses in the ocean. Nature **445**: 163–7.

Diaz, R. J., and R. Rosenberg. 2008. Spreading dead zones and consequences for marine ecosystems. Science **321**: 926–929.

Emerson, S. 2014. Annual Net Community Production and the Biological Carbon Flux in the Ocean. Global Biogeochem. Cycles **28**: 1–12.

Emerson, S., P. Quay, D. M. Karl, C. Winn, and L. M. Tupas. 1997. Experimental determination of the organic carbon flux from open-ocean surface waters. Nature **389**: 951–954.

Emerson, S. R., and S. M. Bushinsky. 2014. Oxygen concentrations and biological fluxes in the open ocean. Oceanography **27**: 168–171.

Emerson, S. R., and S. M. Bushinsky. 2015. Importance of bubbles in air-sea gas flux parameterizations evaluated using in-situ O2, Ar, and N2 measurements. Manuscript

Emerson, S., and C. Stump. 2010. Net biological oxygen production in the ocean—II: Remote in situ measurements of O2 and N2 in subarctic pacific surface waters. Deep Sea Res. Part I Oceanogr. Res. Pap. **57**: 1255–1265.

Emerson, S., C. Stump, and D. Nicholson. 2008. Net biological oxygen production in the ocean: Remote in situ measurements of O2 and N2 in surface waters. Global Biogeochem. Cycles **22**: GB3023.

Fiedler, B., P. Fietzek, N. Vieira, P. Silva, H. C. Bittig, and A. Körtzinger. 2013. In Situ CO2 and O2 Measurements on a Profiling Float. J. Atmos. Ocean. Technol. **30**: 112–126.

Garcia, H. E., T. P. Boyer, S. Levitus, R. a. Locarnini, and J. I. Antonov. 2005. Climatological annual cycle of upper ocean oxygen content anomaly. Geophys. Res. Lett. **32**: 1–4.

Garcia, H. E., R. a. Locarnini, T. P. Boyer, J. I. Antonov, O. K. Baranova, M. M. Zweng, and D. R. Johnson. 2010. World Ocean Atlas 2009 Volume 3: Dissolved Oxygen, Apparent Oxygen Utilization, and Oxygen Saturation. Noaa Atlas Nesdic **70**: 344pp.

Glueckauf, E. 1951. The Composition of Atmospheric Air, p. 3–10. *In* Compendium of Meteorology. American Meteorological Society.

Gruber, N., S. C. Doney, S. R. Emerson, D. Gilbert, T. Kobayashi, A. Körtzinger, G. C. Johnson, K. S. Johnson, S. C. Riser, and O. Ulloa. 2009. Adding oxygen to Argo : Developing a global in-situ observatory for ocean deoxygenation and biogeochemistry. Ocean Obs '09

Hansell, D. A., and C. A. Carlson. 2001. Marine dissolved organic matter and the carbon cycle. Oceanography **14**: 41–49.

Harrison, P. J., F. a. Whitney, A. Tsuda, H. Saito, and K. Tadokoro. 2004. Nutrient and plankton dynamics in the NE and NW Gyres of the subarctic Pacific Ocean. J. Oceanogr. **60**: 93–117.

Hayward, T. L. 1997. Pacific Ocean climate change: atmospheric forcing, ocean circulation and ecosystem response. Trends Ecol. Evol. **12**: 150–154.

Hedges, J. I., J. a. Baldock, Y. Gélinas, C. Lee, M. L. Peterson, and S. G. Wakeham. 2002. The biochemical and elemental compositions of marine plankton: A NMR perspective. Mar. Chem. **78**: 47–63.

Helly, J. J., and L. a. Levin. 2004. Global distribution of naturally occurring marine hypoxia on continental margins. Deep. Res. Part I Oceanogr. Res. Pap. **51**: 1159–1168.

Helm, K. P., N. L. Bindoff, and J. a. Church. 2011. Observed decreases in oxygen content of the global ocean. Geophys. Res. Lett. **38**: 1–6.

Hofmann, A. F., E. T. Peltzer, P. M. Walz, and P. G. Brewer. 2011. Hypoxia by degrees: Establishing definitions for a changing ocean. Deep Sea Res. Part I Oceanogr. Res. Pap. **58**: 1212–1226.

Hofmann, M., and H. Schellnhuber. 2009. Oceanic acidification affects marine carbon pump. Proceedings of the National Academy of Sciences **106**: 3017-3022.

Jayne, S. R., N. G. Hogg, S. N. Waterman, L. Rainville, K. a. Donohue, D. Randolph Watts, K. L. Tracey, J. L. McClean, M. E. Maltrud, B. Qiu, S. Chen, and P. Hacker. 2009. The Kuroshio Extension and its recirculation gyres. Deep. Res. Part I Oceanogr. Res. Pap. **56**: 2088–2099.

Johnson, K. S., W. M. Berelson, E. S. Boss, Z. Chase, H. Claustre, S. R. Emerson, N. Gruber, A. Körtzinger, M. J. Perry, and S. C. Riser. 2009. Observing biogeochemical cycles at global scales with profiling floats and gliders: Prospects for a global array. Oceanography **22**: 216–225.

Johnson, K. S., J. N. Plant, S. C. Riser, and D. Gilbert. 2015. Air oxygen calibration of oxygen optodes on a profiling float array. J. Atmos. Ocean. Technol. (in Rev.

Juranek, L. W., P. D. Quay, R. a. Feely, D. Lockwood, D. M. Karl, and M. J. Church. 2012. Biological production in the NE Pacific and its influence on air-sea CO 2 flux: Evidence from dissolved oxygen isotopes and O 2 /Ar. J. Geophys. Res. **117**: C05022.

Kalnay, E., M. Kanamitsu, R. Kistler, W. Collins, D. Deaven, L. Gandin, S. Iredell, S. Saha, G. White, Y. Zhu, a Leetmaa, R. Reynolds, M. Chelliah, W. Ebisuzaki, W. Higgins, J. Janowiak, K. Mo, C. Ropelewski, J. Wang, R. Jenne, and D. Joseph. 1996. The NCEP/NCAR 40-Year Reanalysis Project. Bull. Am. Meteorol. Soc. **77**: 437–471.

Kamykowski, D., and S.-J. Zentara. 1990. Hypoxia in the world ocena as recorded in the historical data set. Deep. Res. Part I Oceanogr. Res. Pap. **37**: 1861–1874.

Keeling, R. E., A. Körtzinger, and N. Gruber. 2010. Ocean deoxygenation in a warming world. Ann. Rev. Mar. Sci. **2**: 199–229.

Körtzinger, A., J. Schimanski, and U. Send. 2005. High Quality Oxygen Measurements from Profiling Floats: A Promising New Technique. J. Atmos. Ocean. Technol. **22**: 302–308.

Kwon, E. Y., F. Primeau, and J. L. Sarmiento. 2009. The impact of remineralization depth on the air–sea carbon balance. Nat. Geosci. **2**: 630–635.

Laws, E. A., E. D'Sa, and P. Naik. 2011. Simple equations to estimate ratios of new or export production to total production from satellite-derived estimates of sea surface temperature and primary production. Limnol. Ocean. Methods **9**: 593–601.

Ledwell, J. R., A. J. Watson, and C. S. Law. 1993. Evidence for slow mixing across the pycnocline from an open-ocean tracer-release experiment. Nature **364**: 701–703.

Liang, J.-H., C. Deutsch, J. C. McWilliams, B. Baschek, P. P. Sullivan, and D. Chiba. 2013. Parameterizing bubble-mediated air-sea gas exchange and its effect on ocean ventilation. Global Biogeochem. Cycles **27**: 894–905.

Liss, P. S., and L. Merlivat. 1986. Air-sea gas exchange rates - Introduction and synthesis, p. 113–127. *In* P. Buat-Ménard [ed.], The Role of Air-Sea Exchange in Geochemical Cycling.

Longhurst, A., S. Sathyendranath, T. Platt, and C. Caverhill. 1995. An estimate of global primary production in the ocean from satellite radiometer data. J. Plankton Res. **17**: 1245–1271.

McKinley, G. A., M. J. Follows, J. Marshall, and S.-M. Fan. 2003. Interannual variability of air-sea O2 fluxes and the determination of CO2 sinks using atmospheric O2 /N2. Geophys. Res. Lett. **30**, doi:10.1029/2002GL016044

Munro, D. R., P. D. Quay, L. W. Juranek, and R. Goericke. 2013. Biological production rates off the Southern California coast estimated from triple O2 isotopes and O2 : Ar gas ratios. Limnol. Oceanogr. **58**: 1312–1328.

Nicholson, D., S. Emerson, and C. C. Eriksen. 2008. Net community production in the deep euphotic zone of the subtropical North Pacific gyre from glider surveys. Limnol. Oceanogr. **53**: 2226–2236.

Quay, P., J. Stutsman, and T. Steinhoff. 2012. Primary production and carbon export rates across the subpolar N. Atlantic Ocean basin based on triple oxygen isotope and dissolved O2 and Ar gas measurements. Global Biogeochem. Cycles **26**: 1–13.

Resplandy, L., R. Séférian, and L. Bopp. 2015. Natural variability of CO2 and O2 fluxes: What can we learn fromcenturies-long climatemodels simulations? J. Geophys. Res. Ocean. **120**: 384–404.

Riser, S. C., and K. S. Johnson. 2008. Net production of oxygen in the subtropical ocean. Nature **451**: 323–326.

Roemmich, D., G. C. Johnson, S. Riser, R. Davis, J. Gilson, W. B. Owens, S. L. Garzoli, C. Schmid, and M. Ignaszewski. 2009. The Argo Program: Observing the Global Ocean with Profiling Floats. Oceanography **22**: 34–43.

Rohlf, F. J., and R. R. Sokal. 2003. Statistical Tables, Third Edit. W. H. Freeman and Company.

Siegel, D. A., K. O. Buesseler, S. C. Doney, S. F. Sailley, M. J. Behrenfeld, and P. W. Boyd. 2014. Global assessment of ocean carbon export by combining satellite observations and food-web models. Global Biogeochem. Cycles **28**: 181–196.

Sokal, R. R., and F. J. Rohlf. 2003. Biometry, Third Edit. W. H. Freeman and Company.

Sonnerup, R. E., S. Mecking, and J. L. Bullister. 2013. Transit time distributions and oxygen utilization rates in the Northeast Pacific Ocean from chlorofluorocarbons and sulfur hexafluoride. Deep Sea Res. Part I Oceanogr. Res. Pap. **72**: 61–71.

Stanley, R. H. R., W. J. Jenkins, and S. C. Doney. 2006. Quantifying seasonal air-sea gas exchange processes using noble gas time-series: A design experiment. J. Mar. Res. **64**: 267–295.

Stokes, M. D., and G. N. Somero. 1999. An optical oxygen sensor and reaction applications vessel for high-pressure Applications. Limnol. Oceanogr. **44**: 189–195.

Stramma, L., P. Brandt, J. Schafstall, F. Schott, and A. Ko. 2008. Oxygen minimum zone in the North Atlantic south and east of the Cape Verde Islands. **113**: 1–15.

Suga, T., Y. Aoki, H. Saito, and K. Hanawa. 2008. Ventilation of the North Pacific subtropical pycnocline and mode water formation. Prog. Oceanogr. **77**: 285–297.

Suga, T., K. Motoki, Y. Aoki, and A. M. Macdonald. 2004. The North Pacific Climatology of Winter Mixed Layer and Mode Waters. J. Phys. Oceanogr. **34**: 3–22.

Sun, O. M., S. R. Jayne, K. L. Polzin, B. A. Rahter, and L. C. St. Laurent. 2013. Scaling Turbulent Dissipation in the Transition Layer. J. Phys. Oceanogr. **43**: 2475–2489.

Takahashi, T., S. C. Sutherland, C. Sweeney, A. Poisson, N. Metzl, B. Tilbrook, N. Bates, R. Wanninkhof, R. a. Feely, C. Sabine, J. Olafsson, and Y. Nojiri. 2002. Global sea-air CO2 flux based on climatological surface ocean pCO2, and seasonal biological and temperature effects. Deep. Res. Part II Top. Stud. Oceanogr. **49**: 1601–1622.

Takahashi, T., S. C. Sutherland, R. Wanninkhof, C. Sweeney, R. a. Feely, D. W. Chipman, B. Hales, G. Friederich, F. Chavez, C. Sabine, A. Watson, D. C. E. Bakker, U. Schuster, N. Metzl, H. Yoshikawa-Inoue, M. Ishii, T. Midorikawa, Y. Nojiri, A. Körtzinger, T. Steinhoff, M. Hoppema, J. Olafsson, T. S. Arnarson, B. Tilbrook, T. Johannessen, A. Olsen, R. Bellerby, C. S. Wong, B. Delille, N. R. Bates, and H. J. W. de Baar. 2009. Climatological mean and decadal change in surface ocean pCO2, and net sea-air CO2 flux over the global oceans. Deep. Res. Part II Top. Stud. Oceanogr. **56**: 554–577.

Takeshita, Y., T. R. Martz, K. S. Johnson, J. N. Plant, D. Gilbert, S. C. Riser, C. Neill, and B. Tilbrook. 2013. A climatology-based quality control procedure for profiling float oxygen data. J. Geophys. Res. Ocean. **118**: 5640–5650.

Tengberg, A., J. Hovdenes, H. J. Andersson, O. Brocandel, R. Diaz, D. Hebert, T. Arnerich, C. Huber, A. Körtzinger, A. Khripounoff, F. Rey, C. Rönning, J. Schimanski, S. Sommer, and A. Stangelmayer. 2006. Evaluation of a lifetime-based optode to measure oxygen in aquatic systems. Limnol. Oceanogr. Methods **4**: 7–17.

Tengberg, A., J. Hovdenes, D. Barranger, O. Brocandel, R. Diaz, J. Sarkkula, C. Huber, and A. Stangelmayer. 2003. Optodes to Measure Oxygen in the Aquatic Environment. Sea Technol. **44**: 10–15.

Timothy, D. A., C. S. Wong, J. E. Barwell-Clarke, J. S. Page, L. a. White, and R. W. Macdonald. 2013. Climatology of sediment flux and composition in the subarctic Northeast Pacific Ocean with biogeochemical implications. Prog. Oceanogr. **116**: 95–129.

Toggweiler, J. R., and J. L. Sarmiento. 1985. Glacial to interglacial changes in atmospheric carbon dioxide: The critical role of ocean surface water in high latitudes, p. 163–184. *In* E.T. Sundquist and W.S. Broecker [eds.], The Carbon Cycle and Atmospheric CO2: Natural Variations Archean to Present.

Uchida, H., T. Kawano, I. Kaneko, and M. Fukasawa. 2008. In Situ Calibration of Optode-Based Oxygen Sensors. J. Atmos. Ocean. Technol. **25**: 2271–2281.

Volk, and Hoffert. 1985. The Carbon Cycle and Atmospheric CO2: Natural Variations Archean to Present, E.T. Sundquist and W.S. Broecker [eds.]. American Geophysical Union.

Volk, T., and Z. Liu. 1988. Controls of CO2 sources and sinks in the earth scale surface ocean: temperature and nutrients. Global Biogeochem. Cycles **2**: 73–89.

Wanninkhof, R. 1992. Relationship Between Wind Speed and Gas Exchange. J. Geophys. Res. **97**: 7373–7382.

Wanninkhof, R. 2014. Relationship between wind speed and gas exchange over the ocean revisited. Limnol. Oceanogr. Methods **12**: 351–362.

Wearn, R. B., and N. G. Larson. 1982. Measurements of the sensitivities and drift of Digiquartz pressure sensors. Deep Sea Res. Part A. Oceanogr. Res. Pap. **29**: 111–134.

Westberry, T., M. J. Behrenfeld, D. a. Siegel, and E. Boss. 2008. Carbon-based primary productivity modeling with vertically resolved photoacclimation. Global Biogeochem. Cycles **22**: 1–18.

Westberry, T. K., P. J. L. B. Williams, and M. J. Behrenfeld. 2012. Global net community production and the putative net heterotrophy of the oligotrophic oceans. Global Biogeochem. Cycles **26**: GB4019.

Whalen, C. B., L. D. Talley, and J. A. MacKinnon. 2012. Spatial and temporal variability of global ocean mixing inferred from Argo profiles. Geophys. Res. Lett. **39**: L18612.

Whitney, F. A., H. J. Freeland, and M. Robert. 2007. Persistently declining oxygen levels in the interior waters of the eastern subarctic Pacific. Prog. Oceanogr. **75**: 179–199.

Wong, C. S., F. A. Whitney, D. W. Crawford, K. Iseki, R. J. Matear, W. K. Johnson, J. S. Page, and D. Timothy. 1999. Seasonal and interannual variability in particle fluxes of carbon, nitrogen and silicon from time series of sediment traps at Ocean Station P, 1982-1993: relationship to changes in subarctic primary productivity. **46**: 2735–2760.

Yasunaka, S., Y. Nojiri, S. I. Nakaoka, T. Ono, H. Mukai, and N. Usui. 2013. Monthly maps of sea surface dissolved inorganic carbon in the North Pacific: Basin-wide distribution and seasonal variation. J. Geophys. Res. Ocean. **118**: 3843–3850.

Yool, A., E. E. Popova, and T. R. Anderson. 2013. MEDUSA-2.0: An intermediate complexity biogeochemical model of the marine carbon cycle for climate change and ocean acidification studies. Geosci. Model Dev. **6**: 1767–1811.

Zeebe, R. E., and D. A. Wolf-Gladrow. 2001. CO2 in Seawater: Equilibrium, Kinetics, Isotopes, Elsevier Oceanogr. Ser.

VITA

Seth M. Bushinsky

EDUCATION

DEGREES CONFERRED

Ph.D. Oceanography, October, 2015
University of Washington, Seattle, WA
Advised by Dr. Steven Emerson
Thesis title: Improved estimates of air-sea oxygen fluxes and biological carbon export through the use of self-calibrating Argo oxygen floats in the Pacific.

M.S. Oceanography, August, 2011
University of Washington, Seattle, WA
Advised by Dr. Steven Emerson

B.S. with Honors in Biological Sciences, June, 2006
Concentration in Marine Biology
Stanford University, Stanford, CA
Thesis title: A high resolution satellite-based model of Southern Ocean primary production.
Research Advisor: Dr. Kevin Arrigo
Undergraduate Advisor: Dr. Fiorenza Micheli

EMPLOYMENT

Monterey Bay Aquarium Research Institute, Moss Landing, CA, 2006-2008
Research Technician, Dr. Francisco Chavez, Biological Oceanography Group.

FELLOWSHIPS

National Science Foundation IGERT Program on Ocean Change Fellow, 2012-2015

National Science Foundation Graduate Research Fellow, 2009-2012

Achievement Rewards for College Scientists (ARCS) Graduate Fellow, 2008-2011

PEER REVIEWED PUBLICATIONS	Emerson, SR and **S Bushinsky** (2014). Oxygen concentrations and biological fluxes in the open ocean. Oceanography, 27(1): 168-171.
	Bushinsky, SM and S Emerson (2013). A method for in-situ calibration of Aanderaa oxygen sensors on surface moorings. Marine Chemistry, 155: 22-28.
	Howard, E, S Emerson, **S Bushinsky** (2010). Net biological oxygen production at the subarctic-subtropical boundary in the North Pacific. Limnology and Oceanography, 53: 2226-2236.
	Arrigo, KR, GL van Dijken, and **S Bushinsky** (2008). Primary production in the Southern Ocean, 1997–2006. Journal of Geophysical Research, 113, C08004, doi:10.1029/2007JC004551.
	Micheli F, Shelton AO, **Bushinsky SM**, Chiu AL, Haupt AJ, Heiman KW, Kappel CV, Lynch MC, Martone RG, Watanabe J. (2008) Persistence of depleted abalones in marine reserves of central California. Biological Conservation, 141:1078-1090.
	Baglole CJ, **Bushinsky SM**, Garcia TM, Kode A, Rahman I, Sime PJ, Phipps RP. (2006) Differential induction of apoptosis by cigarette smoke extract in primary human lung fibroblast strains: implications for emphysema. Am J Physiol- Lung Cell Mol Physiol, 291: L19-L29.
MANUSCRIPTS IN PREPARATION	**Bushinsky, SM**, S. Emerson, S. Riser, and D. Swift. Accurate oxygen on Argo floats using on-going in-situ air calibrations.
	Bushinsky, SM, and S. Emerson. Marine biological oxygen production from remote in-situ measurements.
	Newsom, E, **S Bushinsky**, A Fassbender, A Maloney. Navigating the cultural divides between policy making and climate science.

PRESENTATIONS

INVITED TALKS	Scientific Committee on Oceanic Research (SCOR) Workgroup 142, Honolulu, HI, March, 2013 (Talk).
	University of Hawai'i Biogeochemistry Brown Bag Seminar, Honolulu, HI, March, 2014 (Talk).
CONFERENCE/MEETING PARTICIPATION	Dissertations Symposium in Chemical Oceanography XXIV, Kaua'i, HI. October, 2014 (Talk).
	Ocean Carbon and Biogeochemistry Workshop, Woods Hole, MA. July, 2014 (Poster).
	7th Line P Workshop, Sidney, BC, March, 2014 (Talk).
	Ocean Sciences Meeting, Honolulu, HI, February, 2014 (Talk).
	Gordon Research Conference in Chemical Oceanography, Biddeford, ME, August, 2013 (Poster).
	Station Papa "Holistic" Ocean Balances Science Workshop, NOAA-PMEL, Seattle, WA, April, 2013 (Talk).
	6th Graduate Climate Conference, Pack Forest, WA, October, 2012 (Poster).
	Ocean Sciences Meeting, Salt Lake City, UT, February, 2012 (Poster).
	Station P Science Workshop, NOAA-PMEL, Seattle, WA, April, 2012 (Talk).
	Gordon Research Conference in Chemical Oceanography, Andover, NH, August, 2011 (Poster).
	Argo-oxygen Meeting, Brest, France, May, 2011 (Talk).
	4th Line P Workshop, Sidney, BC, March, 2011 (Talk).
	4th Graduate Climate Conference, Pack Forest, WA, October, 2010 (Talk).

DEPARTMENTAL TALKS

University of Washington Chemical Oceanography Seminar, Seattle, WA. May, 2014 (Talk).

University of Washington Chemical Oceanography Seminar, Seattle, WA, February, 2013 (Talk).

University of Washington Chemical Oceanography Seminar, Seattle, WA, October, 2009 (Talk).

TEACHING

Guest Lectures, Nitrogen Cycle. Ocean 520: Marine Chemistry. Fall 2014.

Guest Lecture, Ocean Acidification. Osher Lifelong Learning Institute course on Ocean Change. Spring 2014.

Teaching Assistant, Ocean Circulation. Fall 2010.

SIGNIFICANT OCEANOGRAPHIC CRUISES

R/V Thomas G. Thompson. October 2013. 3 days.
Deployment of mooring based oxygen calibration system on Che'ba mooring.

CCGS John P. Tully. June 2013. 19 days.
Calibration, deployment, and recovery of oxygen, nitrogen, and pH sensors at Ocean Station Papa.

R/V Melville. February-March 2013. 21 days.
Calibration and deployment of 10 SOS-Argo floats in the Kuroshio Extension.

CCGS John P. Tully. June 2012. 19 days.
Calibration, deployment, and recovery of oxygen, nitrogen, and pH sensors at Ocean Station Papa. Deployment of initial test SOS-Argo float.

USNS Safeguard. November 2011. 7 days.
Calibration, deployment, and recovery of oxygen, nitrogen, and pH sensors at Kuroshio Extension Observatory.

CCGS John P. Tully. June 2011. 19 days.
Calibration, deployment, and recovery of oxygen, nitrogen, and pH sensors at Ocean Station Papa.

CCGS John P. Tully. June 2010. 19 days.
Calibration, deployment, and recovery of oxygen, nitrogen, and pH sensors at Ocean Station Papa.

CCGS John P. Tully. June 2009. 19 days.
Calibration, deployment, and recovery of oxygen, nitrogen, and pH sensors at Ocean Station Papa. Deployment and recovery of Sea Gliders with oxygen sensors.

R/V Thomas G. Thompson. August 2008. 23 days.
Synthesis and analysis of underway data, sample collection.

PROFESSIONAL AND COMMUNITY SERVICE

Chair of the 4th Graduate Climate Conference. Lead the planning committee in organizing, funding, and choosing applicants for a graduate student only meeting on climate science. Accepted ~80 students from both the U.S. and abroad.

Reviewer for Marine Chemistry.

Graduate Student Representative to the Faculty Council, 2011-2012.

Volunteer diver for Marine Advanced Technology Education ROV competition, 2012, 2013

Mentor, Student Oceanography Club, Monterey Bay Aquarium. Taught middle school students about the ocean and lead field experiences. 2006-2008.